WRC RESEARCH REPORT NO. 30

THE MECHANICS OF A DROP AFTER STRIKING A STAGNANT WATER LAYER

by

Raymond Chun-Tsung Wang

Research Associate

and

Harry G. Wenzel, Jr.

Assistant Professor of Civil Engineering

University of Illinois

REPORT
Project No. B-018-ILL

The work upon which this publication is based was supported by funds provided by the U.S. Department of the Interior as authorized under the Water Resources Research Act of 1964, P.L. 88-379
Agreement No. 14-01-0001-1499

UNIVERSITY OF ILLINOIS
WATER RESOURCES CENTER
3220 Civil Engineering Building
Urbana, Illinois 61801

January 1970

ABSTRACT

THE MECHANICS OF A DROP AFTER STRIKING
A STAGNANT WATER LAYER

This report represents a first step in the theoretical analysis of sheet flow with rainfall impinging on the free surface. This is a common occurrance in urban areas and many design procedures do not recognize the added resistance due to the rainfall. The analytical approach consists of the numerical solution of the Navier-Stokes equations, including surface tension as a boundary condition, using a Synthetic-Cell-Fluid scheme which rigorously conserves mass and momentum. The results include a maximum impact pressure model and a quantitative discussion of pressure distribution, boundary shear, the effect of surface tension, the free surface configuration, and the various forms of energy and its transformation during the impact process. Experiments were performed consisting of drop impact pressure measurements using various drop sizes, impact velocities and water layer depths. These data were used to successfully verify the theoretical work.

Wang, Raymond C. T., and Wenzel, H. G., Jr.
THE MECHANICS OF A DROP AFTER STRIKING A STANGANT WATER LAYER
University of Illinois Water Resources Center Report No. 30
KEYWORDS--*impact (rainfall)/ *numerical analysis/ *raindrops/ shear stress/ *sheet flow/ soil erosion/ resistance

TABLE OF CONTENTS

	Page
LIST OF TABLES	v
LIST OF FIGURES	vi
LIST OF SYMBOLS	viii
1. INTRODUCTION	1
1.1 General Problem Area	1
1.2 Objectives	2
2. REVIEW OF PERTINENT DROP STUDIES	4
3. REVIEW OF PERTINENT NUMERICAL SCHEMES	7
4. THEORETICAL APPROACH	9
4.1 Mathematical Approach	9
4.1.1 Boundary Conditions	11
4.1.2 Initial Conditions	17
4.2 Numerical Scheme	20
4.2.1 Pressure Field	25
4.2.2 Fluid Movement	31
4.2.3 Cell Classification	32
4.2.4 Velocity Field	33
4.2.5 Time Increment	36
5. EXPERIMENTAL PROGRAM	37
5.1 Relation Between Drop Size And Capillary Tube Characteristics	37
5.2 Pressure Transducer	40
6. RESULTS	45
6.1 Experimental Results	45
6.1.1 Impact Pressure Pulse	46
6.1.2 Peak Impact Pressure Versus Water Depth Relation	46
6.2 Analytical Results	54
6.2.1 Impact Pressure Pulse	54
6.2.2 Maximum Impact Pressure Versus Water Depth Relation	55
6.2.3 Velocity Field And Shearing Stress	55
6.2.4 Free Surface Behavior	62

Page

7. DISCUSSION 68

7.1 Comparison Between Analytical And Experimental Impact Pressure 68
7.2 Comparison Between Analytical And Experimental Maximum Impact Pressure 68
7.3 Impact Pressure Model 70
7.4 Vertical Pressure Distribution 80
7.5 Velocity Field And Shearing Stress 81
7.6 Drop-Liquid Impact Behavior 83
7.7 Splashing Test 85
7.8 Energy Transformation 86
7.9 Surface Tension Effect 90
7.10 Effect Of Numerical Scheme On Accuracy Of Solution . . 91
7.11 Error Analysis On Experimental Data 93

8. CONCLUSIONS 102

LIST OF REFERENCES 104

APPENDIX

A THE COMPRESSIBILITY EFFECT 114
B DROP FORMATION DATA 115
C EXPERIMENTAL PRESSURE DATA 116
D ANALYTICAL PRESSURE DATA 124

LIST OF TABLES

Table		Page
1.	Relation Between Tube Size and Drop Size	39
2.	Test Conditions.	45
3.	Fall Height versus Drop Impact Velocity	56

LIST OF FIGURES

FIGURE		PAGE
1	PRINCIPAL RADII OF CURVATURE	15
2	DRAG COEFFICIENT VERSUS REYNOLDS NUMBER	21
3	FALL VELOCITY VERSUS FALL DISTANCE	22
4	COMPUTATION CYCLE	23
5	CELL CONFIGURATION	24
6	APPARATUS ARRANGEMENT	41
7	TYPICAL PRESSURE PULSES	42
8	K VERSUS d_o / d	43
9	d VERSUS d_o	43
10	TRANSDUCER CROSS SECTION AND SURFACE RESPONSE CURVE	44
11	ANALYTICAL VERSUS EXPERIMENTAL PRESSURE PULSE	47
12	ANALYTICAL VERSUS EXPERIMENTAL PRESSURE PULSE	48
13	MAXIMUM IMPACT PRESSURE VERSUS WATER DEPTH FOR d = 2.7 mm	50
14	MAXIMUM IMPACT PRESSURE VERSUS WATER DEPTH FOR d = 3.12 mm	51
15	MAXIMUM IMPACT PRESSURE VERSUS WATER DEPTH FOR d = 3.12 mm	52
16	MAXIMUM IMPACT PRESSURE VERSUS WATER DEPTH FOR d = 3.7 mm	53
17	VELOCITY VECTOR FIELD	57
18	VELOCITY VECTOR FIELD	58
19	SHEARING STRESS FIELD	59
20	SHEARING STRESS FIELD	60
21	SHEARING STRESS FIELD	61
22	FLUID PATTERN	62
23	FLUID MOVEMENT	64
24	FLUID MOVEMENT	65

FIGURE		PAGE
25	FLUID MOVEMENT	66
26	DEPTH VARIATION	67
27	t_p VERSUS h	69
28	DIMENSIONLESS MAXIMUM IMPACT PRESSURE VERSUS WATER DEPTH FOR d = 2.7 mm	74
29	DIMENSIONLESS MAXIMUM IMPACT PRESSURE VERSUS WATER DEPTH FOR d = 3.12 mm	75
30	DIMENSIONLESS MAXIMUM IMPACT PRESSURE VERSUS WATER DEPTH FOR d = 3.12 mm	76
31	DIMENSIONLESS IMPACT PRESSURE VERSUS WATER DEPTH FOR d = 3.7 mm	77
32	φ_c VERSUS h/d	78
33	φ/φ_c VERSUS $2 \overset{*}{r} / h$	79
34	PRESSURE VERSUS DEPTH	79
35	VERTICAL PRESSURE DISTRIBUTION	96
36	VERTICAL PRESSURE DISTRIBUTION	97
37	PRESSURE VARIATION	98
38	MERCURY DROP SPLASHING TEST	98
39	ENERGY TRANSFORMATION	99
40	SURFACE TENSION EFFECT	100
41	COMPUTATIONAL CELL SIZE EFFECT	101
42	COMPUTATIONAL FIELD SIZE EFFECT	101

LIST OF SYMBOLS

A	Drop cross section area
A_c	Effective compression area
c	Compressible wave celerity $= \sqrt{dP/d\rho}$
C_D	Drag coefficient
d	Equivalent drop diameter
d_i	Inside diameter of a tube
d_o	Outside diameter of a tube
D	Fluid dilation $= \frac{1}{r}\frac{\partial r V_r}{\partial r} + \frac{\partial V_z}{\partial z}$
E_i	Initial total energy
E_k	Kinetic energy
E_p	Potential energy
E_s	Surface energy
F	Froude number $= V_o^2/gL$
F_B	Buoyant force
F_D	Drag force
F_W	Gravity force
g	Gravitational acceleration
h	Depth of water layer
H	Drop falling height
K	A constant in drop-tubing relation
L	A length parameter
L_1	Drop tip dimension
L_2	Drop top dimension
L_h	Static water head in forming drops

m	Unit tangent to a surface
n	Unit normal on a surface
N_R	Reynolds number = $V_o L/\nu$
N_{RA}	Reynolds number = $V_o d \rho_a/\mu_a$
P	Point pressure
P_c	Compressible pressure
P_{max}	Maximum impact pressure on transducer
P_p	Impact pressure = $P - \rho g(h-\overset{*}{z})$
$\overset{*}{r}$	Radial component in cylindrical polar coordinate *
r_c	Radial image component
r_o	Radial component of the center of a circle
R	Radial boundary of the fluid domain
$\overset{*}{R}_1$	First principal radius of curvature
$\overset{*}{R}_2$	Second principal radius of curvature
R_*	The radius of a circle
$\overset{*}{t}$	Time variable
t_p	Time to reach peak impact pressure
V	Velocity = $\sqrt{V_r^2 + V_z^2}$
V_D	Drop falling velocity
V_o	Drop impact velocity
$\overset{*}{V}_r$	Velocity component in radial direction
$\overset{*}{V}_z$	Velocity component in axial direction
W	Weber number = $\rho L V_o^2/\Gamma$
Y	Drop falling distance
$\overset{*}{z}$	Axial component in cylindrical polar coordinate
z_c	Axial image component

z_o	Axial component of the center of a circle
ρ	Density of the fluid
ρ_a	Air density
ρ_s	Synthetic cell fluid
μ	Absolute viscosity of the fluid
μ_a	Absolute viscosity of the air
ν	Kinematic viscosity of the fluid
Γ	Surface tension force per unit length
φ	Dimensionless pressure = $P/\rho V_o^2$
φ_c	Dimensionless point pressure at the bottom of the water directly under drop impact point
Δt_d	Drop impact interval
ω	Vorticity = $\frac{\partial V_r}{\partial z} - \frac{\partial V_z}{\partial r}$
Ψ	Fluid volume
Ψ_D	Drop volume
$\sigma_{i,j}$	Stress tensor
$\sigma'_{i,j}$	Deviatoric stress tensor

---

* All variables without asterisk above their center refer to the corresponding dimensionless parameters.

1. INTRODUCTION

1.1 General Problem Area

In recent years the rainfall-runoff process in urban areas has received increased and much needed attention. Furthermore, the process of soil erosion has been of interest to agricultural engineers and others as well for some time. Therefore, a better understanding of the effect of the raindrop impact process is needed. It could lead to developments which would reduce soil erosion and to improved drainage design practices.

The relative raindrop impact effect decreases as the flow depth increases, and is generally neglected in studying open-channel flow problems. However, in analyzing overland flow problems where the depth of flow is small, this effect of drop impact on the flow may be significant. The general approach to this problem has been to solve the one-dimensional spatially varied flow equations, treating rainfall as lateral flow (89)* and including raindrop impact effect in the form of a boundary shear resistance coefficient or overpressure. Early experimental studies by Izzard (80, 81, 82) confirmed the existance of a drop impact effect. Woo and Brater (140) described the impact effect as a function of rainfall intensity, channel slope, and surface roughness. In an analysis of data obtained by Los Angeles District of the Corps of Engineers (97), Yu and McNown (147) showed that the raindrop impact effect decreases as flow rate increases. Glass and Smerdon (50)

*Numbers in parentheses refers to the list of references.

measured the velocity profiles with rainfall and concluded that they are logarithmic. Wenzel, Yoon, and Wang (137) measured the flow depth with rainfall and recognized that it is substantially deeper than that without rainfall at the same flow rate. Chen (23), Chen and Chow (24), and Grace and Eagleson (53) suggested an arbitrary over-pressure to take account of the drop impact effect in their mathematical analyses.

Another approach to study the drop impact effect is a detailed investigation of the flow near the drop impact point. When a drop strikes the sheet flow, a high pressure is momentarily exerted on the water surface at the impact point. This high pressure, as well as the drop itself, is then distributed into the water layer. The pressure and velocity fields due to this process generate a local disturbance which by definition is the effect of drop impact. Consequently, an understanding of the mechanics of drops striking a thin sheet flow will lead toward a complete analytical description of the impact phenomenon and the impact effect as well.

1.2 Objectives

The purpose of this study is to investigate the mechanics of a single water drop after striking a stagnant water layer in hope that it will serve as a first step toward a complete evaluating of the overall raindrop impact effect on sheet flow. More specifically, the objectives of the proposed studying are:

A. To develop a numerical method which will permit the numerical solution of the Navier-Stokes equations for the particular problem of interest.

B. To employ this method to analytically describe the interrelation between drop parameters, water layer depth, and the time dependent velocity, pressure, and shear stress fields in the vicinity of the impact point.

C. To experimentally investigate as fully as possible the relationships stated in the second objective and to thereby verify the analytical approach stated in the first objective.

To reach these objectives, the study is divided into three parts. In the first part, a Synthetic-Cell-Fluid method (hereafter designated as SCF method) is introduced. This scheme is capable of solving the Navier-Stokes equations with free surface boundary conditions for incompressible fluids. In the second part, an experimental program is described which includes a measurement of the drop impact pressure averaged over the surface area of a transducer. These data are used to verify the analytical results obtained by SCF method. In the last part, the SCF method is employed to obtain additional analytical information about the drop-liquid impact phenomenon.

2. REVIEW OF PERTINENT DROP STUDIES

The study of a single drop after it strikes the surface of a liquid layer dates back to the time of Reynolds (119), when he suggested that the sea may be calmed by the action of rain. He also showed the formation of vortex rings from an impinging drop at low impact speed. Recently, Chapman and Critchlow (20) observed the formation of optimum vortex rings when the falling drop is spherical and is changing from an oblate to a prolate spheriod upon contact with the liquid surface. (For a drop with horizontal axis a and vertical axis b, it is defined as an oblate spheroid if $a > b$, and as a prolate spheriod if $a < b$.)

With the advent of high speed photographic techniques, many excellent drop-liquid impact photographs have been published by Worthington (141-146), Edgerton et. al. (34, 35), Charters (22), and Mutchler (111). Worthington also showed the similarity of crater formation between drop-liquid impact and the initial phase of solid-solid impact at high speed.

In designing modern high-speed aerodynamic structures, the impact behavior between drop and liquid, drop and solid, and solid and solid have attracted the attention of many researchers (27, 28, 121). Charters (22) observed the similarity between the crater formed on the Moon's surface and that due to drop-liquid impact. Bowden (14, 15, 16) discussed the deformation of solids by high-speed drop impact and related it to the rain damage in aircraft and missiles. Maximum impact pressure due to compressibility effects was reported to be proportional to the well-known water hammer pressure (15, 16, 39). While maximum

B. To employ this method to analytically describe the interrelation between drop parameters, water layer depth, and the time dependent velocity, pressure, and shear stress fields in the vicinity of the impact point.

C. To experimentally investigate as fully as possible the relationships stated in the second objective and to thereby verify the analytical approach stated in the first objective.

To reach these objectives, the study is divided into three parts. In the first part, a Synthetic-Cell-Fluid method (hereafter designated as SCF method) is introduced. This scheme is capable of solving the Navier-Stokes equations with free surface boundary conditions for incompressible fluids. In the second part, an experimental program is described which includes a measurement of the drop impact pressure averaged over the surface area of a transducer. These data are used to verify the analytical results obtained by SCF method. In the last part, the SCF method is employed to obtain additional analytical information about the drop-liquid impact phenomenon.

2. REVIEW OF PERTINENT DROP STUDIES

The study of a single drop after it strikes the surface of a liquid layer dates back to the time of Reynolds (119), when he suggested that the sea may be calmed by the action of rain. He also showed the formation of vortex rings from an impinging drop at low impact speed. Recently, Chapman and Critchlow (20) observed the formation of optimum vortex rings when the falling drop is spherical and is changing from an oblate to a prolate spheriod upon contact with the liquid surface. (For a drop with horizontal axis a and vertical axis b, it is defined as an oblate spheroid if $a > b$, and as a prolate spheriod if $a < b$.)

With the advent of high speed photographic techniques, many excellent drop-liquid impact photographs have been published by Worthington (141-146), Edgerton et. al. (34, 35), Charters (22), and Mutchler (111). Worthington also showed the similarity of crater formation between drop-liquid impact and the initial phase of solid-solid impact at high speed.

In designing modern high-speed aerodynamic structures, the impact behavior between drop and liquid, drop and solid, and solid and solid have attracted the attention of many researchers (27, 28, 121). Charters (22) observed the similarity between the crater formed on the Moon's surface and that due to drop-liquid impact. Bowden (14, 15, 16) discussed the deformation of solids by high-speed drop impact and related it to the rain damage in aircraft and missiles. Maximum impact pressure due to compressibility effects was reported to be proportional to the well-known water hammer pressure (15, 16, 39). While maximum

3. REVIEW OF PERTINENT NUMERICAL SCHEMES

Since the advent of high speed digital computers, considerable work has been done by researchers which clearly demonstrates that numerical solutions can be obtained for problems to which exact solutions are not available. For the past few decades, a group of researchers at the Los Alamos Scientific Laboratory of the University of California have developed numerous numerical techniques for solving the Navier-Stokes equations (a complete bibliography can be obtained from Group T-3 at the laboratory). Those closely related to the scheme to be used in the proposed study will be summarized.

The Particle-In-Cell (PIC) method (4, 60, 63) is a combined Eulerian-Lagrangian computing scheme for solving multi-material problems. By inserting weighted particles, i.e. particles with mass, into computing cells to trace the fluid movement and to indicate cell mass, this method solves the Navier-Stokes equations in terms of the stream function and vorticity. Rigorously conserving mass, momentum, and energy in the computation, the PIC method is most applicable to hydrodynamic problems with fluid speed comparable to the speed of sound.

The Fluid-In-Cell method (19, 120) is a modified PIC method, in which the mass which flows from cell to cell is assumed to be directly proportional to the density of the cell from which the fluid is flowing (this will henceforth be designated as doner cell concept). This method, resulting in good stability properties for the far subsonic flow regions, is developed to solve single material problems involving large fluid distortions.

The Marker-And-Cell (MAC) method (65, 135) is an Eulerian method introduced to solve multi-material flow problems. Similar to the flow visualization methods, such as following flow movements by injecting hydrogen bubbles or tracers, the MAC method involves the insertion of particles without mass in the cells as markers to trace the fluid movement, and treats pressure and velocity as independent variables. The mass and volume of the fluid domain are preserved which permits the MAC method to be applied to flow problems with a free surface, as well as with confined flow. When the free surface varies slowly and smoothly, surface particles can be joined by sections of cubics through application of a spline fit interpolation method (118, 125, 133). Daly and Pracht (31) were able to include surface tension effects in studying density-current surges. The including of free surface stress conditions in solving incompressible flow calculations was also demonstrated by Hirt and Shannon (75).

By treating massless particles instead of weighted particles, the MAC method adapted the merits of the PIC method in solving incompressible flow problems. In the proposed numerical scheme a synthetic mass is inserted in each cell. The movement of this mass is then determined using the doner cell concept. This permits the solution of incompressible flow problems with free surface boundary conditions in terms of velocity and pressure.

4. THEORETICAL APPROACH

4.1 Mathematical Approach

In order to develop a one-phase fluid model, it is assumed that no interfacial tension exists when a drop strikes the water surface, and that no air entrainment is produced by drop splashing. The fluid density (Appendix A), air and fluid temperatures are further assumed to remain unchanged in the domain of interest and the entire phenomenon is assumed to be axisymmetric. Under these assumptions the equation of continuity and equations of motion which govern the phenomenon after a drop strikes the water surface, are

$$\frac{1}{\overset{*}{r}}\frac{\partial \overset{*}{r}\overset{*}{V}_r}{\partial \overset{*}{r}} + \frac{\partial \overset{*}{V}_z}{\partial \overset{*}{z}} = 0 \tag{1}$$

$$\frac{\partial \overset{*}{V}_r}{\partial \overset{*}{t}} + \frac{1}{\overset{*}{r}}\frac{\partial \overset{*}{r}\overset{*}{V}_r^{\,2}}{\partial \overset{*}{r}} + \frac{\partial \overset{*}{V}_r \overset{*}{V}_z}{\partial \overset{*}{r}} = -\frac{1}{\rho}\frac{\partial P}{\partial \overset{*}{r}} + \nu\frac{\partial}{\partial \overset{*}{z}}\left(\frac{\partial \overset{*}{V}_r}{\partial \overset{*}{z}} - \frac{\partial \overset{*}{V}_z}{\partial \overset{*}{r}}\right) \tag{2}$$

$$\frac{\partial \overset{*}{V}_z}{\partial \overset{*}{t}} + \frac{1}{\overset{*}{r}}\frac{\partial \overset{*}{r}\overset{*}{V}_r \overset{*}{V}_z}{\partial \overset{*}{r}} + \frac{\partial \overset{*}{V}_z^{\,2}}{\partial \overset{*}{z}} = -g - \frac{1}{\rho}\frac{\partial P}{\partial \overset{*}{z}} - \frac{\nu}{\overset{*}{r}}\frac{\partial P}{\partial \overset{*}{r}}\left[\overset{*}{r}\left(\frac{\partial \overset{*}{V}_r}{\partial \overset{*}{z}} - \frac{\partial \overset{*}{V}_z}{\partial \overset{*}{r}}\right)\right] \tag{3}$$

where $\overset{*}{V}_r$ and $\overset{*}{V}_z$ are the radial and axial velocity components respectively in cylindrical polar coordinates $(\overset{*}{r}, \overset{*}{z})$, P is the pressure taken as the gage pressure in this study, ρ is the density of the fluid, g is the gravitational acceleration, $\overset{*}{t}$ is the time variable, and ν is the kinematic viscosity of the fluid.

After the following dimensionless variables and parameters

$$r = \overset{*}{r}/L \ , \qquad z = \overset{*}{z}/L \ , \qquad t = \overset{*}{t}V_o/L$$

$$V_r = \overset{*}{V}_r/V_o \ , \qquad V_z = \overset{*}{V}_z/V_o \ , \qquad \varphi = P/\rho V_o^2 \tag{4}$$

$$N_R = V_o L/\nu \ , \qquad F = V_o^2/gL \ , \qquad W = \rho L V_o^2/\Gamma$$

are introduced into Eqs. 1, 2, and 3, where L is an arbitrary length parameter taken as the cell size dimension in the numerical computation, and Γ is the surface tension force per unit length between air and water, the governing equations become

$$\frac{1}{r}\frac{\partial rV_r}{\partial r} + \frac{\partial V_z}{\partial z} = 0 \tag{5}$$

$$\frac{\partial V_r}{\partial t} + \frac{1}{r}\frac{\partial rV_r^2}{\partial r} + \frac{\partial V_r V_z}{\partial z} = -\frac{\partial \varphi}{\partial r} + \frac{1}{N_R}\frac{\partial}{\partial z}\left(\frac{\partial V_r}{\partial z} - \frac{\partial V_z}{\partial r}\right) \tag{6}$$

$$\frac{\partial V_z}{\partial t} + \frac{1}{r}\frac{\partial rV_r V_z}{\partial r} + \frac{\partial V_z^2}{\partial z} = -\frac{1}{F} - \frac{\partial \varphi}{\partial z} - \frac{1}{N_R}\frac{1}{r}\frac{\partial}{\partial r}\left[r\left(\frac{\partial V_r}{\partial z} - \frac{\partial V_z}{\partial r}\right)\right] \tag{7}$$

With given initial and boundary conditions, Eqs. 5, 6, and 7 describe the pressure and velocity fields. However, no closed form analytical solution is presently available, and a two-step numerical scheme is used together with the proper boundary conditions to solve this initial value

if the fluid in contact with the boundary has zero velocity, and

$$V_r = 0$$

$$V_z \neq 0$$

$$\frac{\partial V_z}{\partial r} = 0 \qquad (11\text{-b})$$

$$\frac{\partial \varphi}{\partial r} = 0$$

if the fluid is assumed to slip freely along the wall. At the free surface the rapid change of the free surface shape is one of the most interesting parts of the drop splashing problem. However, a quantitative expression for the transient free surface tension force due to this rapid change is not available (95). Boussinesq (13) assumed that a dynamic surface tension exists at interfaces in motion. Its magnitude is given by the sum of the static surface tension and the dynamic increment. The latter is assumed to be proportional to the rate of dilation at that point. The constant of proportionality is called the coefficient of surface viscosity. However, in their experimental investigation of the drag and shape of air bubbles, Haberman and Morton (56) could not find experimental evidence that dynamic surface tension force exists. In order to take the surface tension force into account, the free surface is assumed to be in a local equilibrium stage, and transient free surface tension force is assumed to be equal to that of the static case in the same free surface configuration.

The free surface is not easily determined accurately, but its shape can be approximated in the numerical scheme. At the free surface, the only net force exerted on it is the surface tension force.

In differential form this condition is expressed as (75, 91)

$$\Gamma\left(\frac{1}{\overset{*}{R}_1} + \frac{1}{\overset{*}{R}_2}\right) n_i = - \sigma_{i,j} n_j = P n_i - \sigma'_{i,j} n_j \qquad (i,j = 1,2) \tag{12}$$

where $\sigma_{i,j}$ and $\sigma'_{i,j}$ are the tensor and deviatoric tensor stresses respectively, n is the unit outward normal and $\overset{*}{R}_1$ and $\overset{*}{R}_2$ are the principal radii of curvature of the surface, assumed positive when the corresponding centers of curvature lie on the fluid side.

In Fig. 1, $\overset{*}{R}_1$ denotes the local radius of curvature of a surface curve formed on $\overset{*}{r}$ - $\overset{*}{z}$ plane. While $\overset{*}{R}_2$, in axisymmetric case, is the radius of curvature of a curve formed by the intersection of the plane with a cone which is tangent to the surface at the surface and has symmetry about the $\overset{*}{z}$ axis. For a free surface, $\overset{*}{z} = \eta(\overset{*}{r},\overset{*}{t})$ as shown, the unit outward normal vector n and tangent vector m are

$$\begin{aligned} n_r &= - \frac{\partial \eta}{\partial \overset{*}{r}}\left[1+\left(\frac{\partial \eta}{\partial \overset{*}{r}}\right)^2\right]^{-\frac{1}{2}} = -m_z \\ n_z &= \left[1+\left(\frac{\partial \eta}{\partial \overset{*}{r}}\right)^2\right]^{-\frac{1}{2}} = m_r \end{aligned} \tag{13}$$

where subscripts r and z refer to unit vector and $\overset{*}{r}$ and $\overset{*}{z}$ directions respectively.

After substituting the stress tensor components, $\sigma_{i,j}$ (124),

$$\begin{aligned} \sigma_{rr} &= - P + 2\mu \frac{\partial \overset{*}{V}_r}{\partial \overset{*}{r}} \\ \sigma_{zz} &= - P + 2\mu \frac{\partial \overset{*}{V}_z}{\partial \overset{*}{z}} \\ \sigma_{rz} &= \mu\left(\frac{\partial \overset{*}{V}_r}{\partial \overset{*}{z}} + \frac{\partial \overset{*}{V}_z}{\partial \overset{*}{r}}\right) \end{aligned} \tag{14}$$

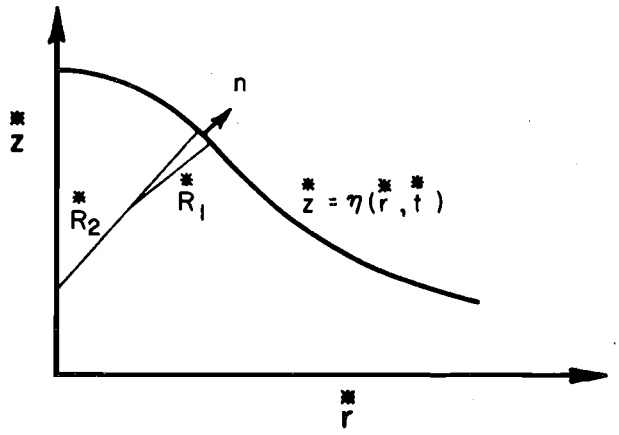

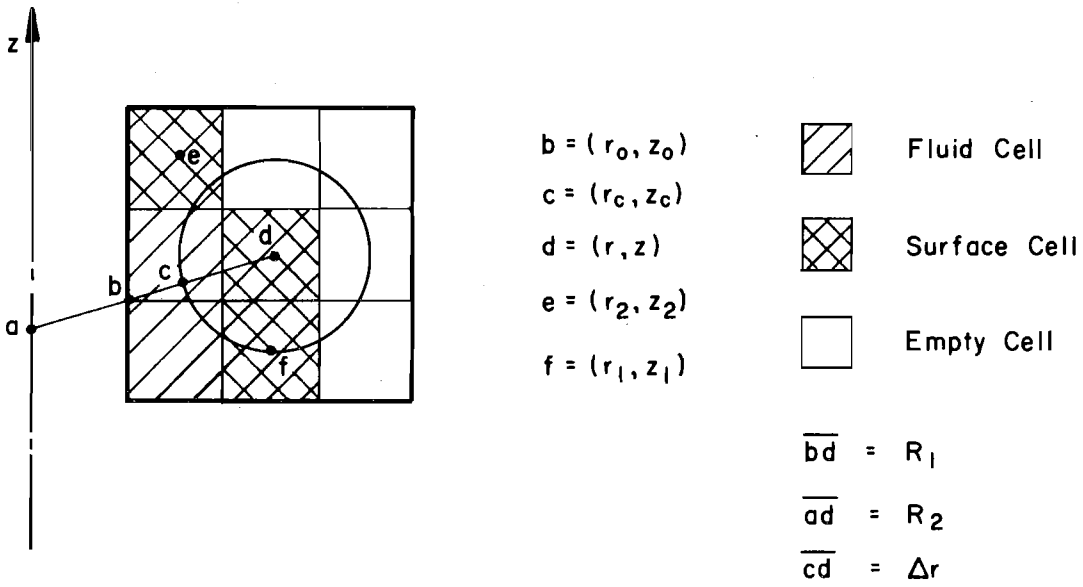

FIGURE I PRINCIPAL RADII OF CURVATURE

where μ is the absolute viscosity of the fluid, into the free surface boundary condition Eq. 12, the result is

$$\Gamma\left(\frac{1}{\overset{*}{R}_1}+\frac{1}{\overset{*}{R}_2}\right) n_r = Pn_r - 2\mu \frac{\partial \overset{*}{V}_r}{\partial \overset{*}{r}} n_r - \mu\left(\frac{\partial \overset{*}{V}_r}{\partial \overset{*}{z}} + \frac{\partial \overset{*}{V}_z}{\partial \overset{*}{r}}\right) n_z \tag{15}$$

$$\Gamma\left(\frac{1}{\overset{*}{R}_1}+\frac{1}{\overset{*}{R}_2}\right) n_z = Pn_z - 2\mu \frac{\partial \overset{*}{V}_z}{\partial \overset{*}{z}} n_z - \mu\left(\frac{\partial \overset{*}{V}_r}{\partial \overset{*}{z}} + \frac{\partial \overset{*}{V}_z}{\partial \overset{*}{r}}\right) n_r \tag{16}$$

If Eq. 15 is multiplied by n_r and then added to Eq. 16 multiplied by n_z the result is

$$P - 2\mu\left[n_r^2 \frac{\partial \overset{*}{V}_r}{\partial \overset{*}{r}} + n_r n_z \left(\frac{\partial \overset{*}{V}_r}{\partial \overset{*}{z}} + \frac{\partial \overset{*}{V}_z}{\partial \overset{*}{r}}\right) + n_z^2 \frac{\partial \overset{*}{V}_z}{\partial \overset{*}{z}}\right] = \Gamma\left(\frac{1}{\overset{*}{R}_1}+\frac{1}{\overset{*}{R}_2}\right) \tag{17}$$

Now Eq. 16 multiplied by n_z and subtracted from Eq. 15 multiplied by n_r yields

$$P(n_r^2 - n_z^2) = \Gamma\left(\frac{1}{\overset{*}{R}_1}+\frac{1}{\overset{*}{R}_2}\right)(n_r^2 - n_z^2) + 2\mu\left(n_r^2 \frac{\partial \overset{*}{V}_r}{\partial \overset{*}{r}} - n_z^2 \frac{\partial \overset{*}{V}_z}{\partial \overset{*}{z}}\right) \tag{18}$$

Furthermore, Eq. 15 can be multiplied by m_r and added to Eq. 16 multiplied by m_z to give

$$\mu\left[2n_r m_r \frac{\partial \overset{*}{V}_r}{\partial \overset{*}{r}} + (n_r m_z + n_z m_r)\left(\frac{\partial \overset{*}{V}_r}{\partial \overset{*}{z}} + \frac{\partial \overset{*}{V}_z}{\partial \overset{*}{r}}\right) + 2n_z m_z \frac{\partial \overset{*}{V}_z}{\partial \overset{*}{z}}\right] = 0 \tag{19}$$

Finally Eqs. 17, 18, and 19 can be written in dimensionless form and combined with Eq. 13 to yield

$$\varphi = \frac{1}{W}\left(\frac{1}{R_1} + \frac{1}{R_2}\right) + \frac{2}{N_R}\left[n_r^2 \frac{\partial V_r}{\partial r} + n_r n_z \left(\frac{\partial V_r}{\partial z} + \frac{\partial V_z}{\partial r}\right) + n_z^2 \frac{\partial V_z}{\partial z}\right] \qquad (20)$$

$$\varphi = \frac{1}{W}\left(\frac{1}{R_1} + \frac{1}{R_2}\right) + \frac{2}{N_R}\left(n_r^2 \frac{\partial V_r}{\partial r} - n_z^2 \frac{\partial V_z}{\partial z}\right)/\left(n_r^2 - n_z^2\right) \text{ if } n_r^2 \neq n_z^2 \qquad (21)$$

$$0 = \frac{1}{N_R}\left[2n_r n_z \left(\frac{\partial V_r}{\partial r} - \frac{\partial V_z}{\partial z}\right) + \left(n_z^2 - n_r^2\right)\left(\frac{\partial V_r}{\partial z} + \frac{\partial V_z}{\partial r}\right)\right] \qquad (22)$$

where $R_1 = \overset{*}{R}_1/L$ and $R_2 = \overset{*}{R}_2/L$, which are the free surface boundary conditions.

4.1.2 Initial Conditions

The initial conditions needed in the two-step computation outlined earlier are drop shape and drop velocity at the moment of impact. Drops formed by capillary tubes leave the tip of the tube with different initial shapes (35, 59, 71). They start to deform and oscillate as they fall. Even under ideal conditions such as drops falling in stagnant air, no analytical description of the drop's behavior has been obtained; not to mention the rather complex behavior of raindrops while falling in the air. However, it is believed (93, 103) that a single drop, after falling a sufficient distance in stagnant air, will reach a stable shape and terminal

velocity provided it is not so large as to disintegrate into smaller drops. After a drop reaches this stable stage, McDonald (103, 104) suggested that the drop shape is a function of surface tension force, internal hydrostatic pressure, external aerodynamic pressure, internal circulation, and electrostatic charge. The last two factors are in general small enough to be neglected, whereas the first three can give a rough estimation of the stable drop shape. In the present study, although drops reaching and not reaching their stable shape are to be investigated, the stable drop shapes obtained experimentally by McDonald (103) and Mutchler (111) are used as the drop shape upon impact.

Neglecting minor forces, the balance between drag force, F_D, buoyant force, F_B, and gravity force, F_W, for a freely falling drop gives

$$F_W - F_B - F_D = \rho \forall_D \frac{dV_D}{dt} = 0.5\, \rho \forall_D \frac{dV_D^2}{dy}$$

or

$$\frac{\pi d^3}{6}(\rho-\rho_a)g - 0.5\rho_a V_D^2 \frac{\pi d^2}{4} C_D = \frac{\pi \rho d^3}{12} \cdot \frac{dV_D^2}{dy} \qquad (23)$$

where $\forall_D = \frac{\pi d^3}{6}$ is the volume of the drop, ρ_a is the air density, d is the equivalent drop diameter (the diameter of an equivalent sphere having the same volume as that of the drop), y is the direction of fall, V_D is the fall velocity, and C_D is the drag coefficient based on a projected area of an equivalent sphere. The drag coefficient, C_D, can therefore be evaluated from Eq. 23

$$C_D = \left[\left(1 - \frac{\rho_a}{\rho}\right)g - 0.5\,\frac{dV_D^2}{dy}\right] \Big/ \left[\frac{3\rho_a V_D^2}{4\rho d}\right] \tag{24}$$

Based on data obtained from the fall height versus fall velocity relations measured by Gunn and Kinzer (54) for stable drops and by Laws (93) for stable and unstable drops, drag coefficients were calculated and plotted against $N_{RA} = \rho_a V_D d/\mu_a$ in Fig. 2. The resulting drag coefficient relationship deviatesincreasingly from that of a solid sphere for $N_{RA} > 1000$, indicating that the drop is flattening and therefore the drag force is increasing with N_{RA}. Fitting a least square curve to the data in Fig. 2 gives

$$\begin{aligned}
N_{RA} &\leq 0.6 && C_D = 24/N_{RA} \\
0.6 < N_{RA} &\leq 10. && \log_{10} C_D = 1.398 - 0.903 \log_{10} N_{RA} \\
&&& \quad + 0.117(\log_{10} N_{RA})^2 \\
10. < N_{RA} &< 100. && \log_{10} C_D = 1.195 - 0.590 \log_{10} N_{RA} \\
100. \leq N_{RA} &\leq 1000. && \log_{10} C_D = 2.119 - 1.525 \log_{10} N_{RA} \\
&&& \quad + 0.240(\log_{10} N_{RA})^2 \\
1000. < N_{RA} &< 3600. && \log_{10} C_D = 1.097 + 0.377 \log_{10} N_{RA} \\
&&& \quad - 0.349(\log_{10} N_{RA})^2 - 0.076(\log_{10} N_{RA})^3 \\
&&& \quad + 0.033(\log_{10} N_{RA})^4
\end{aligned} \tag{25}$$

The general agreement between data obtained by Laws and Gunn and Kinzer indicated in Fig. 2 enables the establishment of a relationship between fall velocity and fall height for drops of 0.1 mm to 6.1 mm in diameter. Equation 23 can be rearranged as

$$Y = \int dy = 0.5 \int \left[\left(1 - \frac{\rho_a}{\rho}\right)g - \frac{3\rho_a C_D}{4\rho d}\, V_D^2\right]^{-1} dV_D^2 \tag{26}$$

With the initial condition $V_D = 0$ at $Y = 0$, Eq. 26 can be integrated

numerically and the result used with Eq. 25 to determine the impact velocity of a drop falling a specific distance. Test runs for three drop sizes of equivalent drop diameter of 2.3 mm, 3.0 mm, and 3.92 mm (at 68° F) displaying the relation between fall velocity and fall height are plotted in Fig. 3. Values predicted are in general agreement with Laws' data.

4.2 Numerical Scheme

The two-step numerical scheme is shown schematically in Fig. 4. With a given fluid domain, defined as the fluid field under consideration at a specific moment, and velocity field at time t, the pressure field based on Eq. 8 can be evaluated. The fluid is then moved by utilizing a Synthetic-Cell-Fluid method, and the fluid domain at an advanced stage is defined by preserving the total fluid mass. Equations 6 and 7 then yield the new velocity field and the whole computational cycle starts again.

Since the drop-liquid impact phenomenon is assumed to be axi-symmetric, only half of the (r, z) plane needs be considered. The computational field is divided into rectangular cells as shown in Fig. 5. The cell pressure is located at the center of each individual cell. While velocities in r-direction are centered on the left and right side of the cell, and velocities in z-direction are centered on the upper and lower side of the cell to satisfy the equation of continuity at each individual cell. With this cell configuration in mind, the numerical procedure is described below.

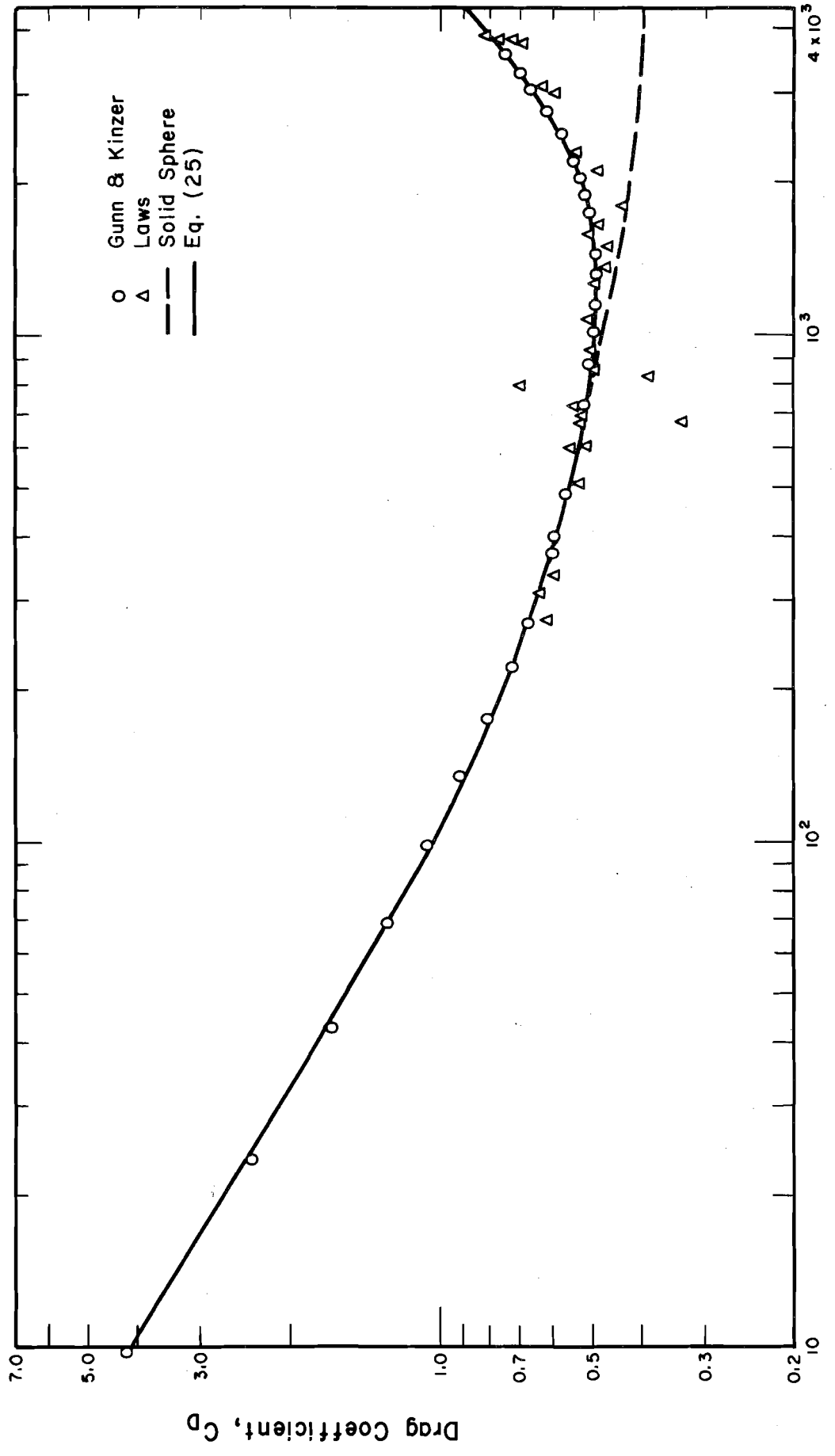

FIGURE 2 DRAG COEFFICIENT VERSUS REYNOLDS NUMBER

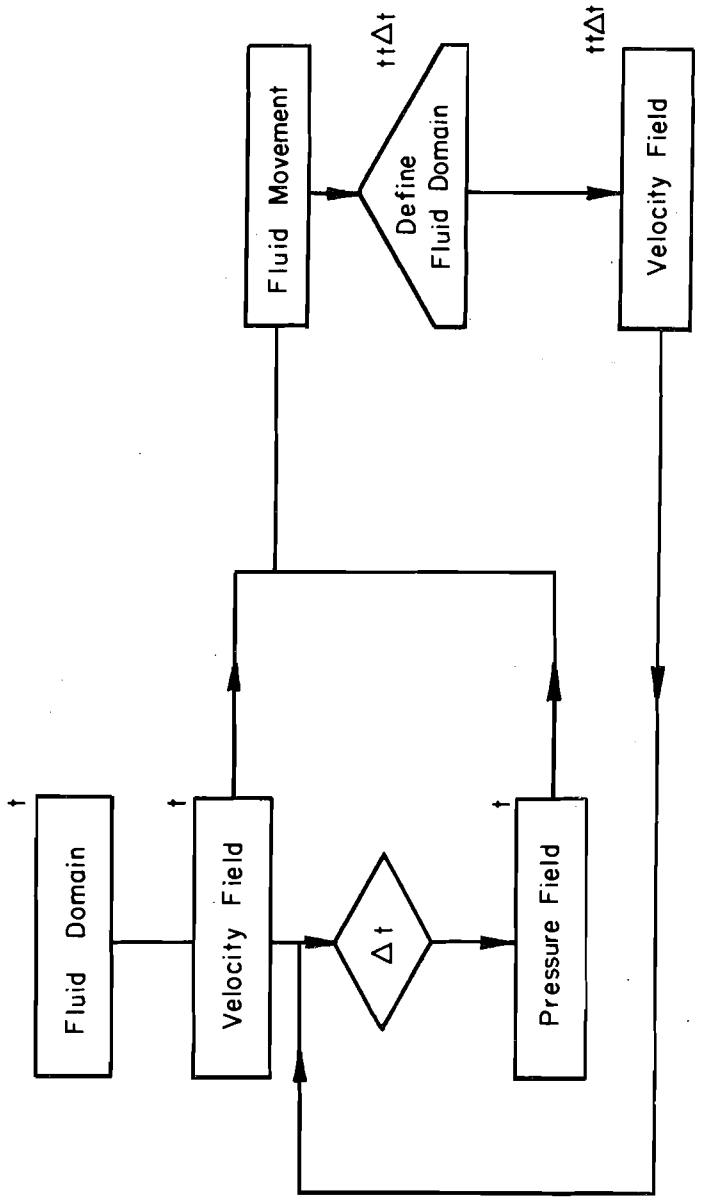

FIGURE 4 COMPUTATION CYCLE

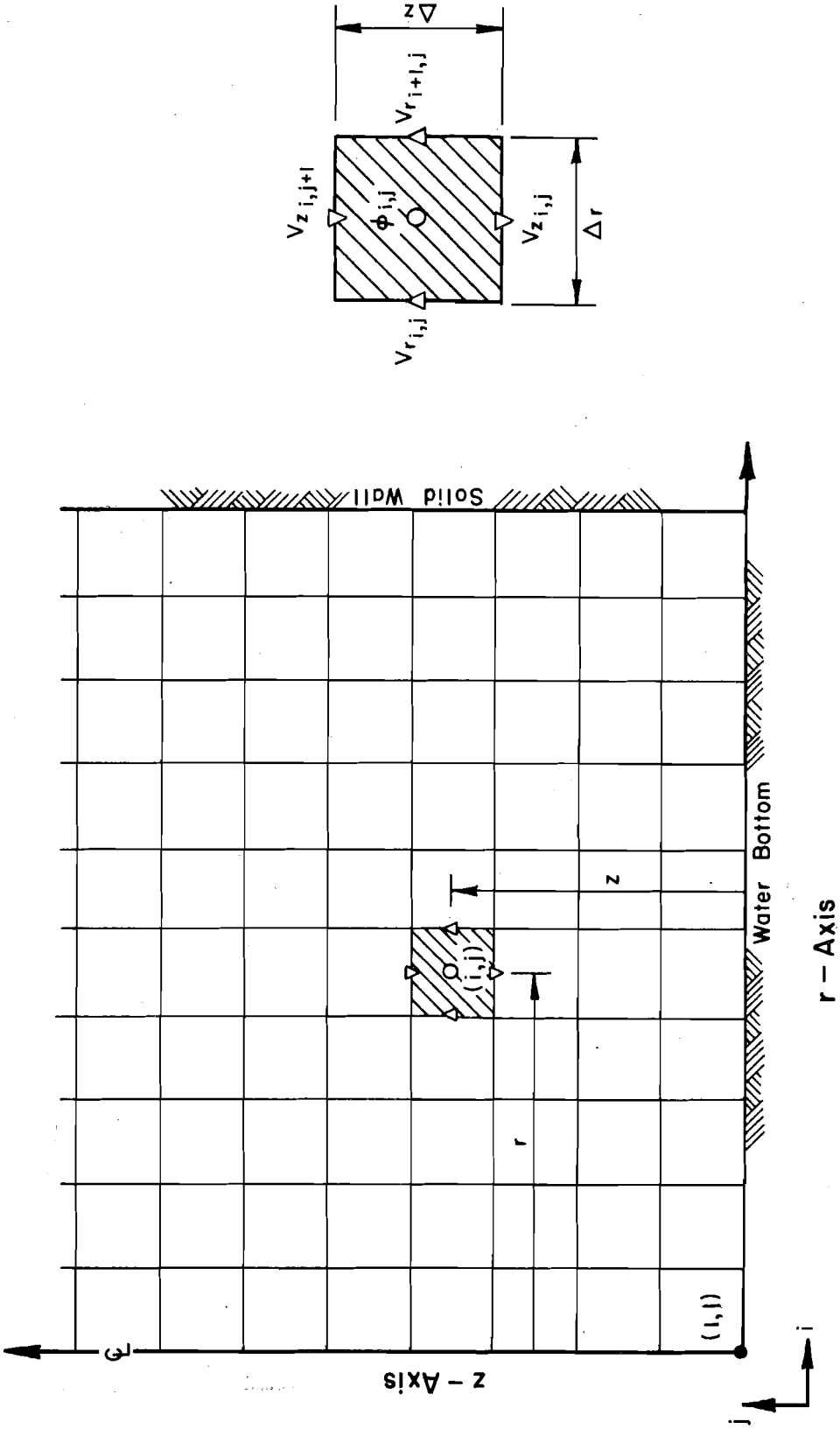

FIGURE 5 CELL CONFIGURATION

4.2.1 Pressure Field

In simple explicit difference form, Eq. 7 becomes

$$f(\varphi) = \frac{D^t - D^{t+\Delta t}}{\Delta t} - g(V) \tag{27}$$

where

$$f(\varphi) = \frac{\partial^2 \varphi}{\partial z^2} + \frac{1}{r}\frac{\partial}{\partial r}\left(r\frac{\partial \varphi}{\partial r}\right)$$

$$= \frac{1}{\Delta z^2}[\varphi_{i,j+1} + \varphi_{i,j-1} - 2\varphi_{i,j}] + \frac{1}{(i-0.5)\Delta r^2}[i(\varphi_{i+1,j} - \varphi_{i,j}) \tag{27-a}$$

$$-(i-1)(\varphi_{i,j} - \varphi_{i-1,j})]$$

$$g(V) = \frac{2}{r}\frac{\partial^2 (rV_rV_z)}{\partial r\,\partial z} + \frac{\partial^2 V_z{}^2}{\partial z^2} + \frac{1}{r}\frac{\partial^2 rV_r{}^2}{\partial r^2}$$

$$= \frac{1}{(2i-1)\Delta r\Delta z}[i(V_{r_{i+1,j}} + V_{r_{i+1,j+1}})(V_{z_{i,j+1}} + V_{z_{i+1,j+1}}) - (i-1)$$

$$(V_{r_{i,j}} + V_{r_{i,j+1}})(V_{z_{i,j+1}} + V_{z_{i-1,j+1}}) - i(V_{r_{i+1,j}} + V_{r_{i+1,j-1}})$$

$$(V_{z_{i,j}} + V_{z_{i+1,j}}) + (i-1)(V_{r_{i,j}} + V_{r_{i,j-1}})(V_{z_{i,j}} + V_{z_{i-1,j}})] +$$

$$\frac{1}{4\Delta z^2}[(V_{z_{i,j+1}} + V_{z_{i,j+2}})^2 + (V_{z_{i,j}} + V_{z_{i,j-1}})^2 - 2(V_{z_{i,j}} + V_{z_{i,j+1}})^2]$$

$$+ \frac{1}{(4i-2)\Delta r^2}[(i+0.5)(V_{r_{i+1,j}} + V_{r_{i+2,j}})^2 + (i-1.5)(V_{r_{i,j}}$$

$$+ V_{r_{i-1,j}})^2 - (2i-1)(V_{r_{i,j}} + V_{r_{i+1,j}})^2] \tag{27-b}$$

and all variables without superscript refer to time t. With a known fluid domain and velocity field at time t and assuming $D^{t+\Delta t}$ is zero, an iteration procedure satisfying the proper boundary conditions is used to evaluate $\varphi_{i,j}$ in terms of its neighboring values at four adjacent cells such that the following criteria in the entire fluid domain are satisfied:

$$\frac{|\varphi^{K+1}_{i,j} - \varphi^{K}_{i,j}|}{|\varphi^{K+1}_{i,j} + \varphi^{K}_{i,j} + V^2_{r_{i,j}} + V^2_{z_{i,j}} + 2h/F|} \leqslant \epsilon \tag{28}$$

$$\left| \frac{|\Sigma f\ (\varphi)|}{|\Sigma g\ (V)|} - 1.0 \right| \leqslant \epsilon \tag{29}$$

where superscripts k and k+1 stand for two successful φ values in iteration process, and ϵ is an arbitrary small value chosen to yield an allowable small D value, although theoretically D = 0. The carry over error is calculated as

$$D^{t+\Delta t} = D^{t} - \Delta t\ [f(\varphi)+g(V)] \tag{30}$$

which is then taken as the new D value for advance stage computations. This avoids the accumulation error after many cycles of time advancement (66, 73) and permits the use of a larger cell size.

In the present study fluid and empty cells are designated as cells filled or not filled with fluid and surface and interior cells refer to fluid cells adjoining or not adjoining empty cells. In evaluating the

pressure in the surface cells the centers of the surface cells are regarded as the discrete surface elements to approximate the surface curvature and unit normal at each surface cell. At a surface cell centering at (r, z), eight cells neighboring to it are checked to see whether they are surface or interior cells. When the total number of surface cells among these nine cells is less than three, the pressure in the surface cell interested is taken as zero. When there are three or more than three surface cells, three of them are chosen such that the four cells in direct contact with the surface cell under consideration have a high priority to be selected than the other four cells in the diagonal direction, while the surface cell considered with least priority can also be taken as one of them if necessary. The first principal radius, R_1, of a surface element centered at (r, z) is then taken as the radius of a circle, R_*, passing through the centers of these three surface cells (r_k, z_k), k = 1, 2, 3* (Fig. 1) Hence

$$R_* = [(r_1-r_o)^2 + (z_1-z_o)^2]^{\frac{1}{2}} \qquad \text{if } \Delta \neq 0 \tag{31}$$

where (r_o, z_o) is the center of the circle, and

$$r_o = \begin{vmatrix} (r_1^2 + z_1^2 - r_2^2 - z_2^2) & 2(z_1 - z_2) \\ (r_2^2 + z_2^2 - r_3^2 - z_3^2) & 2(z_2 - z_3) \end{vmatrix} / \Delta$$

$$z_o = \begin{vmatrix} 2(r_1 - r_2) & (r_1^2 + z_1^2 - r_2^2 - z_2^2) \\ 2(r_2 - r_3) & (r_2^2 + z_2^2 - r_3^2 - z_3^2) \end{vmatrix} / \Delta$$

*While this work was undertaken, a similar scheme to evaluate the principal radii was presented by Daly (32).

The directions as well as the signs of n_r and n_z are determined by the characteristics of the surface cells as follows:

When $\text{cell}_{i+1,j}$ is a fluid cell while $\text{cell}_{i-1,j}$ is an empty cell, $n_r = |n_r|$

When $\text{cell}_{i-1,j}$ is a fluid cell while $\text{cell}_{i+1,j}$ is an empty cell, $n_r = -|n_r|$

When $\text{cell}_{i,j+1}$ is a fluid cell while $\text{cell}_{i,j-1}$ is an empty cell, $n_z = |n_z|$

When $\text{cell}_{i,j-1}$ is a fluid cell while $\text{cell}_{i,j+1}$ is an empty cell, $n_z = -|n_z|$

And R_1 is infinite.

(35)

The second principal radius, R_2 is defined as the length of a line drawn perpendicular to the local surface profile from the center of the surface cell to the axisymmetric axis.

$$|R_2| = r\left[1 + \left(\frac{n_z}{n_r}\right)^2\right]^{\frac{1}{2}} \tag{36}$$

It is regarded as positive if the free surface is concave inward with respect to the symmetric axis. Therefore,

$$R_2 = |R_2| \qquad \text{if} \quad n_r \geq 0$$

$$R_2 = -|R_2| \qquad \text{if} \quad n_r < 0 \tag{37}$$

After the two principal radii R_1 and R_2 are determined, the pressure in the surface cell can be evaluated from the difference form of Eq. 21

$$\varphi_{i,j} = \frac{1}{W}\left(\frac{1}{R_1} + \frac{1}{R_2}\right) + \frac{2}{N_R(n_r^2 - n_z^2)}\left[n_r^2 \frac{V_{r_{i+1,j}} - V_{r_{i,j}}}{\Delta r} - n_z^2 \frac{V_{z_{i,j+1}} - V_{z_{i,j}}}{\Delta z}\right] \quad (38)$$

if $n_r^2 \neq n_z^2$, or from the difference form of Eq. 20

$$\varphi_{i,j} = \frac{1}{W}\left(\frac{1}{R} + \frac{1}{R_2}\right) + \frac{2}{N_R}\left[n_r^2 \frac{V_{r_{i+1,j}} - V_{r_{i,j}}}{\Delta r} + n_z^2 \frac{V_{z_{i,j+1}} - V_{z_{i,j}}}{\Delta z} + n_r n_z \left(\frac{\partial V_r}{\partial z} + \frac{\partial V_z}{\partial r}\right)_{i,j}\right] \quad (39)$$

if $n_r^2 = n_z^2$, where $\left(\frac{\partial V_r}{\partial z} + \frac{\partial V_z}{\partial r}\right)_{i,j}$ is interpolated from known values inside the fluid domain.

After the pressure in the surface cells is determined, the rest of the interior pressure field can be evaluated by using Eq. 27. If Eq. 27 were transformed into a series of linear algebraic equations, the pressure field could be solved in a closed form. However, the large number of manipulations required in solving the simultaneous algebraic equations make it impractical, and a simple iteration scheme based on the Gauss-Jorden technique is used to evaluate the pressure field in the interior cells. A set of trial $\varphi_{i,j}$ values designated as $\varphi_{i,j}^{K}$ are formed by the iteration procedure

$$\varphi_{i,j}^{K+1} = \varphi_{i,j}^{K} - \frac{f(\varphi_{i,j})}{\partial f(\varphi_{i,j})/\partial \varphi_{i,j}}$$

$$= \frac{\dfrac{\varphi_{i,j+1}^{K+1} + \varphi_{i,j-1}^{K}}{\Delta z^2} + \dfrac{i\varphi_{i+1,j}^{K} + (i-1)\,\varphi_{i-1,j}^{K+1}}{(i-0.5)\,\Delta r^2} - \dfrac{D^t}{\Delta t} + g(V)}{\dfrac{2}{\Delta r^2} + \dfrac{2}{\Delta z^2}} \quad (40)$$

where k = 1, 2, ..., and stands for the successive trial steps, and the first trial value $\varphi_{i,j}^{1}$ is assumed equal to the true $\varphi_{i,j}$ value at its previous stage, since the time increment Δt is small. This implies that

$\varphi_{i,j}$, $\varphi_{i-1,j}$, and $\varphi_{i,j+1}$ are allowed to relax while $\varphi_{i+1,j}$ and $\varphi_{i,j-1}$ are held firm as hinge points when the iteration process is centered at $\varphi_{i,j}$ value. In two successive trial steps if the criterion

$$\frac{\varphi_{i,j}^{k+1} - \varphi_{i,j+1}^{k}}{\Delta z^2} + \frac{(i-1)(\varphi_{i-1,j}^{k+1} - \varphi_{i-1,j}^{k})}{(i-0.5)\,\Delta r^2} < (\varphi_{i,j}^{k+1} - \varphi_{i,j}^{k})\left(\frac{2}{\Delta r^2} + \frac{2}{\Delta z^2}\right) \tag{41}$$

is satisfied, Eq. 40 yields a set of converging $\varphi_{i,j}^{K}$ values which converge to the true $\varphi_{i,j}$ value at time t. When the difference between two successive group of trial values is small enough to satisfy Eqs. 28 and 29, the trial $\varphi_{i,j}^{K}$ value is taken as the true $\varphi_{i,j}$ value at time t and yields the pressure at the interior cells.

4.2.2 Fluid Movement

The 'synthetic cell fluid' physically represents the fractional part of the cell which is occupied by the fluid, ρ_s. Its variation is traced as an indication of the fluid movement. The general equation of continuity in the form for the compressible fluid flow

$$\frac{\partial \rho_s}{\partial t} + \frac{1}{r}\frac{\partial \rho_s r V_r}{\partial r} + \frac{\partial \rho_s V_z}{\partial z} = 0 \tag{42}$$

is assumed to govern the movement of the synthetic cell fluid, and the fluid which flows from cell to cell is assumed to be directly proportional to the density of the cell from which the fluid is flowing (doner cell concept). Thus, Eq. 42 in finite difference form becomes

$$\rho_{s_{i,j}}^{t+\Delta t} = \rho_{s_{i,j}}^{t} - \Delta t\{\frac{1}{(i-0.5)\Delta r}[iV_{r_{i+1,j}}\rho_{sA} - (i-1)V_{r_{i,j}}\rho_{sB}] + \frac{1}{\Delta z}(V_{z_{i,j+1}}\rho_{sC} - V_{z_{i,j}}\rho_{sD})\} \tag{43}$$

where

$$\rho_{sA} = \begin{cases} \rho_{s_{i,j}} & \text{if } V_{r_{i+1,j}} \geq 0 \\ \rho_{s_{i+1,j}} & V_{r_{i+1,j}} < 0 \end{cases} \qquad \rho_{sC} = \begin{cases} \rho_{s_{i,j}} & \text{if } V_{z_{i,j+1}} \geq 0 \\ \rho_{s_{i,j+1}} & V_{z_{i,j+1}} < 0 \end{cases}$$

$$\rho_{sB} = \begin{cases} \rho_{s_{i,j}} & \text{if } V_{r_{i,j}} \leq 0 \\ \rho_{s_{i-1,j}} & V_{r_{i,j}} > 0 \end{cases} \qquad \rho_{sD} = \begin{cases} \rho_{s_{i,j}} & \text{if } V_{z_{i,j}} \leq 0 \\ \rho_{s_{i,j-1}} & V_{z_{i,j}} > 0 \end{cases} \tag{44}$$

Equation 43 then gives the subsequent synthetic cell fluid in each cell and the general fluid movement is thus determined.

4.2.3 Cell Classification

The synthetic cell fluid stands for the fractional part of a cell which is occupied by the fluid. However, in the velocity and pressure computations, a cell must be classified as either being filled with incompressible fluid or empty. Thus, cells whose synthetic cell fluid is greater than certain value $\xi(t)$ are defined as fluid cells. The value of $\xi(t)$ is determined when

$$\sum_{\rho_{s_{i,j}} > \xi(t)} \rho_{s_{i,j}} \Delta\forall_{i,j} \cong \text{Initial total fluid volume} \tag{45}$$

is satisfied, where $\Delta\forall_{i,j}$ is the volume of $\text{cell}_{i,j}$. In other words

$$\text{a cell is a fluid cell if } \rho_{s_{i,j}} > \xi(t) \tag{46}$$

$$\text{a cell is an empty cell if } \rho_{s_{i,j}} \leq \xi(t) \tag{47}$$

For computational purposes, each cell in the (r, z) plane is further designated according to its relative position as follows:

$$\begin{aligned} \text{cell}_{i,j} &= 0 \text{ if it is an empty cell} \\ &= 1 \text{ if it is an interior cell} \\ &= 2 \text{ if it is a surface cell with one side contacting empty cells} \\ &= 3 \text{ if it is a surface cell with two sides contacting empty cells} \\ &= 4 \text{ if it is a surface cell with three sides contacting empty cells} \\ &= 5 \text{ if it is a surface cell with all sides contacting empty cells} \end{aligned} \tag{48}$$

4.2.4 Velocity Field

After evaluating the pressure field at time t and classifying the fluid domain at an advance stage $t + \Delta t$, Eqs. 5, 6, and 7 written in finite difference form become

$$\frac{1}{(i-0.5)\Delta r}\left[i V_{r_{i+1,j}}^{t+\Delta t} - (i-1)\, V_{r_{i,j}}^{t+\Delta t}\right] + \frac{1}{\Delta z}\left(V_{z_{i,j+1}}^{t+\Delta t} - V_{z_{i,j}}^{t+\Delta t}\right) = 0 \tag{49}$$

$$V_{r_{i+1,j}}^{t+\Delta t} = V_{r_{i+1,j}} + \Delta t\{\frac{1}{4i\Delta r}[(i-0.5)(V_{r_{i,j}} + V_{r_{i+1,j}})^2 - (i+0.5)(V_{r_{i+1,j}} + V_{r_{i+2,j}})^2] + \frac{1}{4\Delta z}[(V_{r_{i+1,j}} + V_{r_{i+1,j-1}})(V_{z_{i,j}} + V_{z_{i+1,j}}) - (V_{r_{i+1,j}} + V_{r_{i+1,j+1}})(V_{z_{i,j+1}} + V_{z_{i+1,j+1}})] + \frac{1}{\Delta r}(\varphi_{i,j} - \varphi_{i+1,j}) + \frac{1}{N_R}[(V_{r_{i+1,j+1}} + V_{r_{i+1,j-1}} - 2V_{r_{i+1,j}})/\Delta z^2 - (V_{z_{i+1,j+1}} - V_{z_{i+1,j}} - V_{z_{i,j+1}} + V_{z_{i,j}})/(\Delta r \Delta z)]\} \quad (50)$$

$$V_{z_{i,j+1}}^{t+\Delta t} = V_{z_{i,j+1}} + \Delta t\{\frac{1}{(4i-2)\Delta r}[(i-1)(V_{r_{i,j}} + V_{r_{i,j+1}})(V_{z_{i,j+1}} + V_{z_{i-1,j+1}}) - i(V_{r_{i+1,j}} + V_{r_{i+1,j+1}})(V_{z_{i,j+1}} + V_{z_{i+1,j+1}})] + \frac{1}{4\Delta z}[(V_{z_{i,j}} + V_{z_{i,j+1}})^2 - (V_{z_{i,j+1}} + V_{z_{i,j+2}})^2] + \frac{1}{\Delta z}(\varphi_{i,j} - \varphi_{i,j+1}) - \frac{1}{F} - \frac{1}{(i-0.5)\Delta r N_R}[i((V_{r_{i+1,j+1}} - V_{r_{i+1,j}})/\Delta z - (V_{z_{i+1,j+1}} - V_{z_{i,j+1}})/\Delta r) - (i-1)((V_{r_{i,j+1}} - V_{r_{i,j}})/\Delta z - (V_{z_{i,j+1}} - V_{z_{i-1,j+1}})/\Delta r))]\} \quad (51)$$

where all variables without superscript refer to time t.

When the fluid cell considered is an interior cell, the new velocity field over there is directly calculated from Eqs. 50 and 51. When the fluid cell under consideration is a surface cell, the equation of continuity, Eq. 49, and equations of motion, Eqs. 50 and 51, together with the free surface boundary condition, Eq. 22, define the new velocity field. It is assumed that $\text{cell}_{i,j}^{t+\Delta t}$ has the same surface position as $\text{cell}_{i,j}^{t}$ had upon velocity evaluation in order to simplify the rather

complex cell configuration; for example $cell_{i,j}^{t+\Delta t} = 2$ whereas $cell_{i,j}^{t} = 3$. When the fluid cell has one side open ($cell_{i,j} = 2$), the velocities at the other three adjacent faces are calculated using Eqs. 50, 51, and 22, and the velocity at the open face is calculated using the continuity equation, Eq. 49. When the two open faces of the fluid cell are adjacent to each other ($cell_{i,j} = 3$), n_r is assumed to be equal to n_z in Eq. 22. The latter, together with Eqs. 49, 50, and 51 yields the velocity field. When the two open faces are opposite to each other, the unit normal becomes undefined and Eq. 22 is not valid. In order to overcome this difficulty the velocity at one of the open faces is assumed to have the same value as that at time t. When three faces of the fluid cell are open ($cell_{i,j} = 4$), the velocities at any two of the faces are assumed equal to the values at the previous time. The velocities at the other two faces are evaluated from Eqs. 49, 50, or 51. Whereas, a fluid cell with all faces in contact with empty cells ($cell_{i,j} = 5$) is treated as moving in a free projected profile, i.e.

$$V_z^{t+\Delta t} = V_z^t - \Delta t/F$$

$$V_r^{t+\Delta t} = V_r^t \qquad (52)$$

disregarding the three dimensional instability that might occur (146). In the special case when the computational cell is transformed from an empty cell at time t to a fluid cell at time $t+\Delta t$, the new velocity at any face in contact with a fluid cell is calculated using the equation of motion. Velocities at other faces are evaluated from the free

surface boundary conditions, Eq. 22, or are assumed to be equal to the velocities at time t. However, one of the four velocity components has to be evaluated from the equation of continuity, Eq. 49, to preserve the fluid mass.

4.2.5 Time Increment

In chosing time increment in time-dependent computations, numerical instability must be avoided. However, the non-linear characters of the equations of motion, Eqs. 6 and 7, make a rigorous stability analysis unavailable. Therefore, the time increment satisfying all the following heuristic stability criteria (61, 115, 123, 135) is employed in the present study.

$$\Delta t < \text{Minimum} \frac{\Delta r}{\left|\,|V_r| + |V_z|\,\right|} \quad , \qquad \text{when } \Delta r = \Delta z \tag{53}$$

which is also the von Neumann condition which must be satisfied upon introducing the vorticity function, $\omega = \frac{\partial V_r}{\partial z} - \frac{\partial V_z}{\partial r}$, into the equation of motion to reach a linearized stability criterion.

$$\Delta t < 0.5\, \Delta z^2 \cdot N_R \quad , \qquad \text{when } \Delta r = \Delta z \tag{54}$$

which is the Courant condition restricting the distance a wave can travel in one time increment to be less than one space interval.

$$\Delta t < \Delta r \sqrt{F/h} \quad , \qquad \text{when } \Delta r = \Delta z \tag{55}$$

which is the Courant condition for gravity waves with small wave number.

5. EXPERIMENTAL PROGRAM

In order to establish experimentally the relation between maximum impact pressure and water layer depth as a function of drop size and drop impact velocity, an experimental program was carried out to measure the pressure pulse at the boundary immediately beneath the impact point of a single drop as it strikes a stagnant thin water layer. The apparatus arrangement is schematically drawn in Fig. 6. It consisted of a drop former placed at a specific elevation above a thin water layer. By varying the elevation of the drop former, the impact velocity of the drop was varied. The water layer was contained in a smooth plexiglass tray 2 ft square with 6 in. high sides. At the center of the tray a Kistler 606A quartz pressure transducer was mounted flush with the tray bottom. The pressure signal from the transducer passed through a Model 504 Kistler charge amplifier containing a Model 548A8 plug-in filter for resonance attenuation, and was displayed on a Tektronix type 564 storage oscilloscope. The signal was sufficiently clear on the calibrated graticule of the scope to permit it to be traced on graph paper manually rather than recorded photographically. Some typical signals are shown in Fig. 7.

5.1 Relation Between Drop Size And Capillary Tube Characteristics

Water drops have been produced by many methods (6, 26, 34, 55, 107, 113). The method of capillary tube production produces the most uniform size drop and therefore was used. A simple drop former was constructed by inserting a length of capillary tube through the bottom of a water container. When water slowly flowed from the capillary tube a steady jet did

not occur but rather a series of drops were formed because of the surface tension force. If the pressure at the tube entrance is kept constant and the tube has a square sharp edge, the drop thus formed is a function of the tube tip geometry, the surface tension force between air and water, the flow rate through the tube, and the air drag force on the drop. The relationship between the weight of the drop, tube size, and surface tension can be approximately expressed as

$$\text{Drop weight} = K\pi d_o \Gamma \tag{56}$$

where d_o is the outside diameter of the tube, and K is an experimental constant varying from 0.59 to 1.00 (99). When the flow rate through the tube approaches zero, Harkins (59) showed that

$$K = f \text{ (tube tip condition, capillary constant)} \tag{57}$$

where capillary constant = $(2\Gamma/\rho)^{\frac{1}{2}}$. He obtained an experimental relationship between K and d_o/d as shown in Fig. 8. When the flow rate increases the analysis of drop production becomes a complicated one. Mutchler (108) obtained an experimental relation assuming

$$\text{Drop weight} = \text{function } (\Gamma, d_o, q, \nu, g) \tag{58}$$

where q is the flow rate through the tube. Manfré and Whorlow (100) also reported the relation between drop weight and $\mu\rho\ gq/\Gamma^2$ for a specific tube indicating that the drop weight increases to a maximum value as $\mu\rho\ gq/\Gamma^2$ increases.

The O.W.R.R. research project aimed at investigating the effect of drop impact on sheet flow employs a series of rainfall modules to produce drops. Each module contains many capillary tubes to form individual drops (137). Since there was some variation in the length and end configuration of the individual tubes, the water level in the water container, the tube length, the tube tip geometry, and the temperature of the water were combined to produce drops that might be formed by a typical tube in the rainfall modules. To establish the relation between drop and capillary tube size, various drop formers were constructed by inserting different sizes of polyethylene tubes through the bottom of a plexiglass container. Tap water with temperature varying between 65^{o} and 74^{o}F was then placed in the water container. In each test, 50 to 300 drops produced from the drop former were collected and weighed to 0.001 gm. The results obtained are shown in Appendix B. Some pertinent data are also tabulated in Table 1.

Table 1. Relation Between Tube Size and Drop Size

Tube Name	Tube OD d_o (in.)	Tube ID d_i (in.)	Equivalent drop dia. d (mm)
PE10	0.024	0.011	2.62-2.73
PE50	0.038	0.023	2.92-3.26
PE20	0.038	0.023	3.09-3.13
--	0.050	0.023	3.50-3.52
PE160	0.062	0.045	3.60-3.74
PE320	0.138	0.106	4.60-4.68

Data obtained are also displayed in Fig. 9 showing the relationship between equivalent drop diameter, d, and tube outside diameter, d_o. The data tend to fall on a line with a slope of 1 to 3 which agrees with the relation stated in Eq. 56 since the surface tension variation is small. Other researchers' data are also included for comparison.

5.2 Pressure Transducer

In testing an Atlantic LD-107 transducer, White (138) showed that the surface sensitivity varies across the surface of the transducer and that the transducer response changes with the frequency of the signal. In addition the drop impact pressure in the present study is not uniformally distributed above the sensing element of the transducer; therefore, the output signal was a function of the pressure averaged over the sensing element of the transducer.

A Kistler 606A quartz pressure transducer mounted flush with the surface of the tray bottom was used to measure the dynamic pressure due to drop impact. A cross sectional view supplied by Kistler Corporation of the upper portion of the transducer, Fig. 10, shows that the effective sensing area is not the same as the surface area of the transducer. The surface response sensitivity was assumed to have a one-to-one response from the center of the transducer to a radius of 0.132 in. and to decrease linearly from that value down to zero response at a radius of 0.156 in. The transducer had a resonant frequency greater than 130 KHz, a senitivity of 5.0 picocoulomb/psi, and a rise time of approximately 3.0 microseconds.

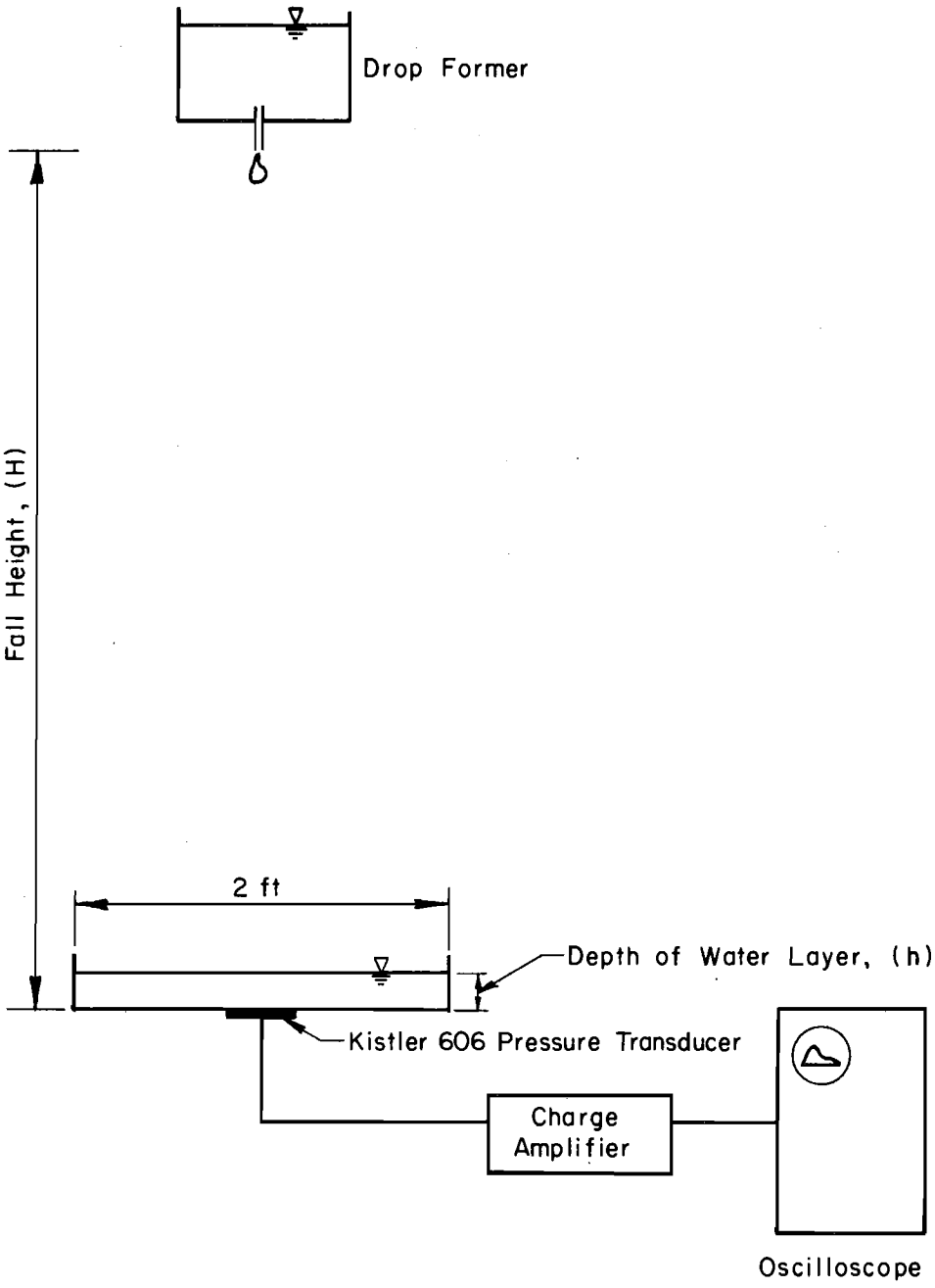

FIGURE 6 APPARATUS ARRANGEMENT

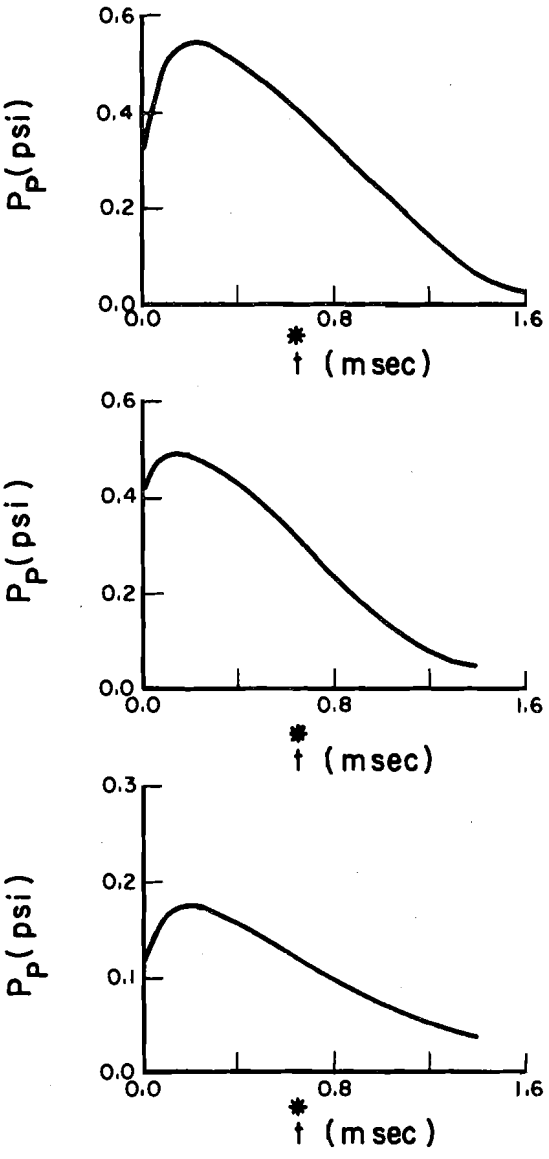

d = 3.7 mm
v_0 = 15.9 fps
h = 0.105 in.

d = 3.12 mm
v_0 = 26.8 fps
h = 0.209 in.

d = 2.7 mm
v_0 = 21.1 fps
h = 0.278 in.

FIGURE 7 TYPICAL PRESSURE PULSES

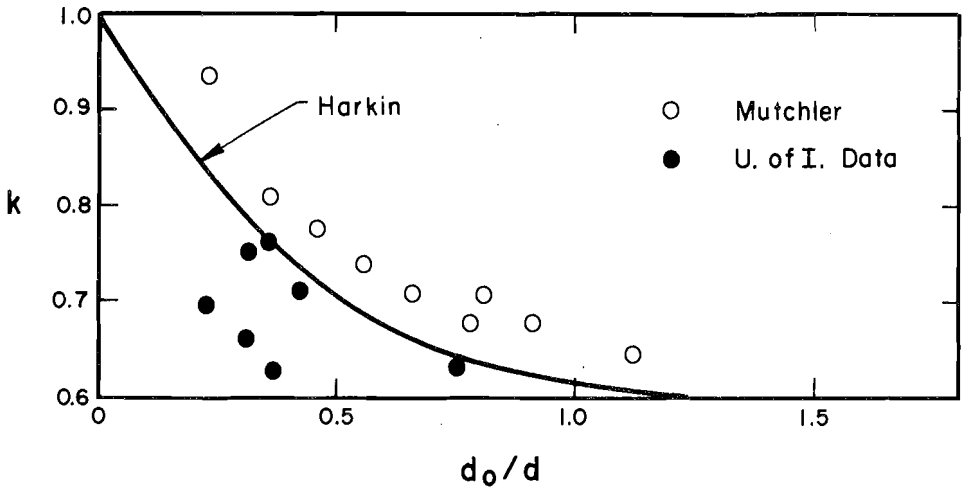

FIGURE 8 K VERSUS d_o/d

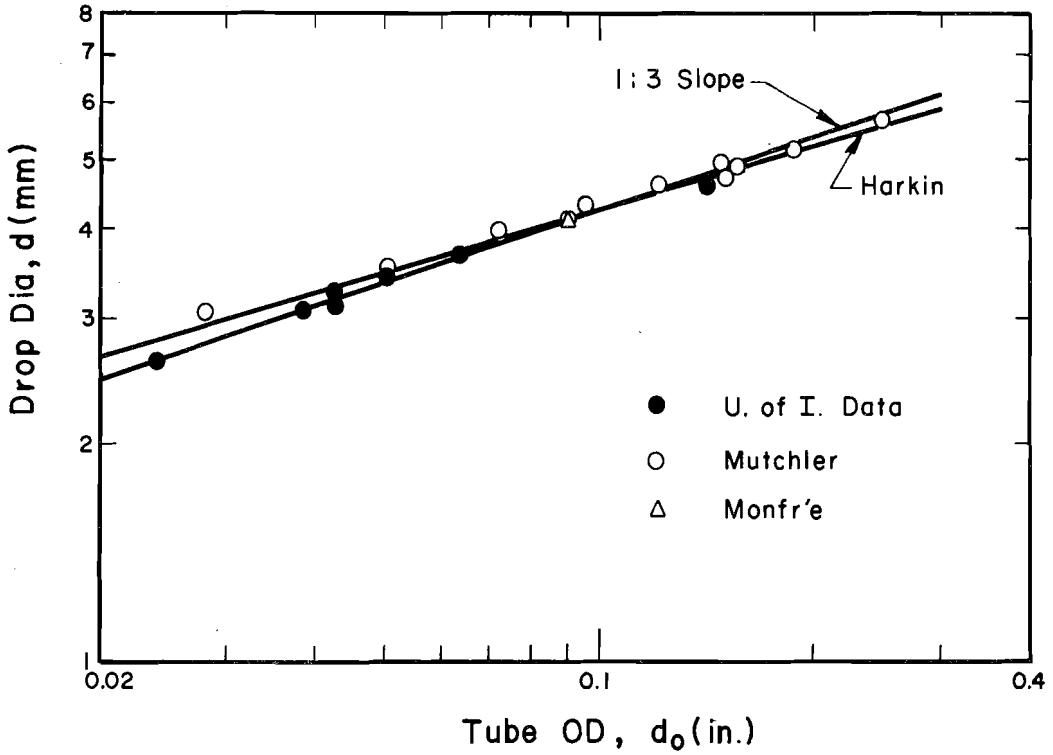

FIGURE 9 d VERSUS d_o

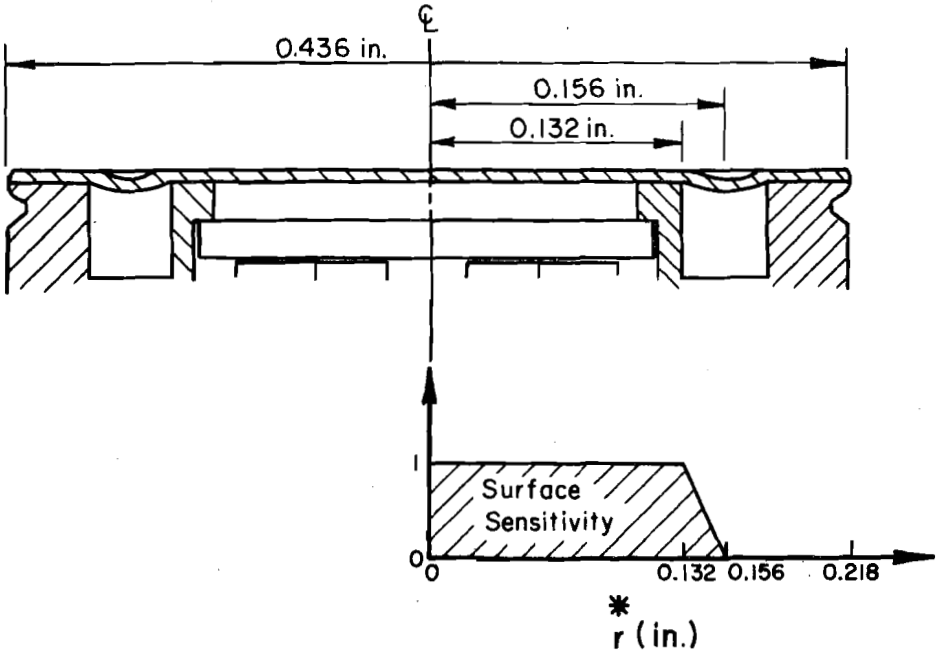

FIGURE 10 TRANSDUCER CROSS SECTION AND SURFACE RESPONSE CURVE (COURTESY TO THE THE KISTLER INSTRUMENT CORPORATION)

6. RESULTS

6.1 Experimental Results

Test conditions for this study are summarized below in Table 2.

Table 2. Test Conditions

	Range
Drop diameter, d (mm)	2.7-3.7
Height of fall, H (ft)	4.25-33.0
Water depth, h (in.)	0. to 0.82
Temperature (^{o}F)	64-75

Four different sizes of drops ranging from 2.7 to 3.7 mm, which approximate the most frequent occurring drops in natural storms of 1.0 to 6.0 in./hr intensity (94), were produced from different sizes of polyethylene tubes and were allowed to fall a specific distance in the air before striking the water layer below. Drop tests with a height of fall of approximately four, seven, twelve feet were conducted in the Hydraulic Engineering Laboratory at the University of Illinois. In addition, a drop former was set up on the third floor walkway above the structural test floor of the Civil Engineering Building at the University of Illinois to supply a 33 ft clear span, which thereafter allowed the falling drop to acquire an impact velocity close to its terminal velocity.

6.1.1 Impact Pressure Pulse

In each test, the drop was allowed to fall freely from a given height and to strike a water layer of known depth. Since there was lateral drop motion as it fell (109), the plexiglass tray was installed on a small carrier which was centered manually such that the transducer was below the most probable drop impact point. In order to assure no interference between successive drops, the drops were intercepted until the disturbance from the previous drop impact was dissipated. With triggering level of the scope well adjusted, the impact pressure pulses picked up by the transducer were displayed on the oscilloscope screen. Among these pressure pulses recorded the one which had the maximum magnitude was used as the impact pressure pulse under direct impact. Other pressure pulses were due to impact not striking upon the center of the transducer and were therefore disregarded. The impact pressure pulse due to direct impact was repeatable and was manually traced on the graph paper. Some typical pressure pulses with different impact conditions are shown in Figs. 11 and 12, while all the test data are tabulated in Appendix C.

6.1.2 Peak Impact Pressure Versus Water Depth Relation

The maximum impact pressure, P_{max}, of each pressure pulse as a function of water layer depth for different drop impact conditions is tabulated in Appendix C and is plotted in Figs. 13-16.

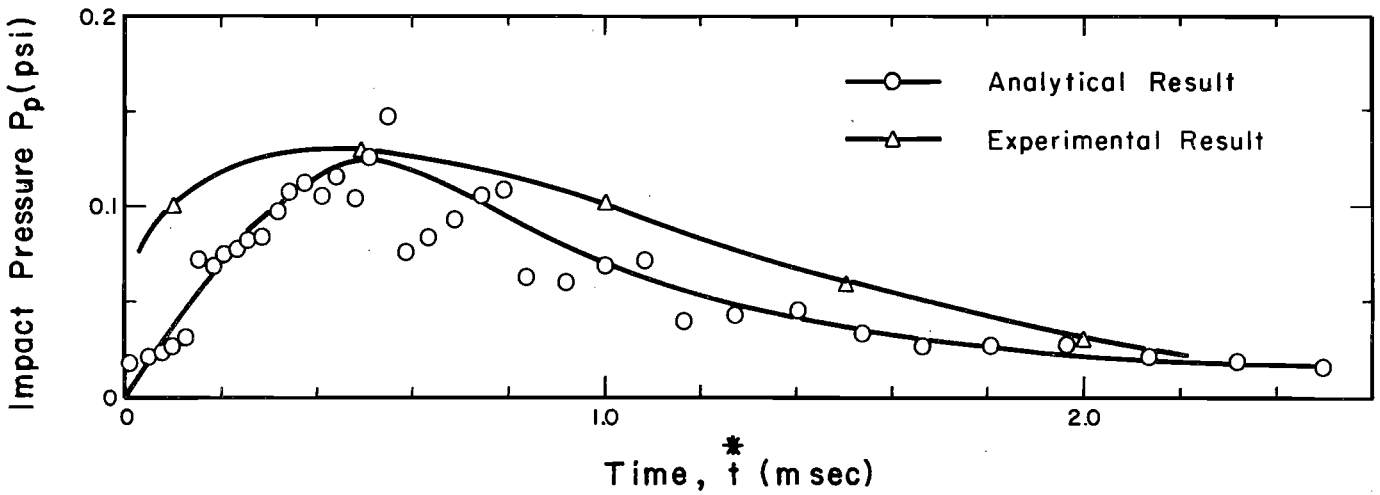

Experimental Data		Analytical Data
d (mm)	3.7	3.7
V_o(fps)	15.9	15.9
h (in.)	0.328	0.33

FIGURE 11 ANALYTICAL VERSUS EXPERIMENTAL PRESSURE PULSE

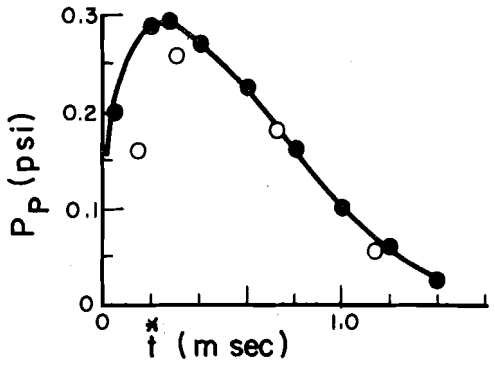

	—●—	o
d (mm)	2.7	2.7
V_0 (fps)	15.4	15.4
h (in.)	0.11	0.12

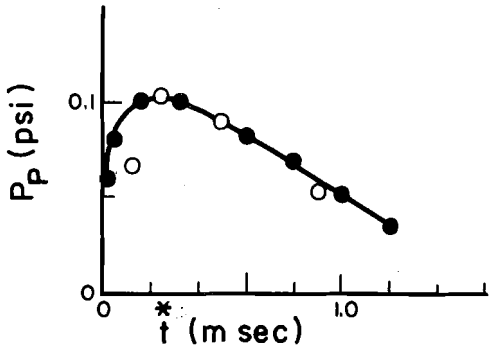

	—●—	o
d (mm)	3.12	3.12
V_0 (fps)	21.8	21.8
h (in.)	0.481	0.473

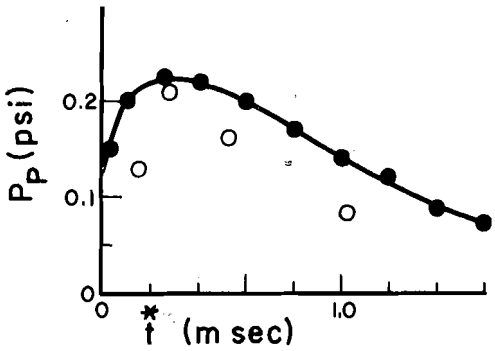

	—●—	o
d (mm)	3.7	3.7
V_0 (fps)	22.6	22.6
h (in.)	0.389	0.395

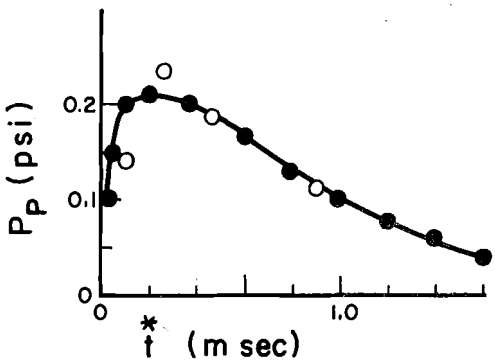

	—●—	o
d (mm)	3.12	3.12
V_0 (fps)	21.8	21.8
h (in.)	0.31	0.278

—●— Experimental Result

o Analytical Result

FIGURE 12 ANALYTICAL VERSUS EXPERIMENTAL PRESSURE PULSE

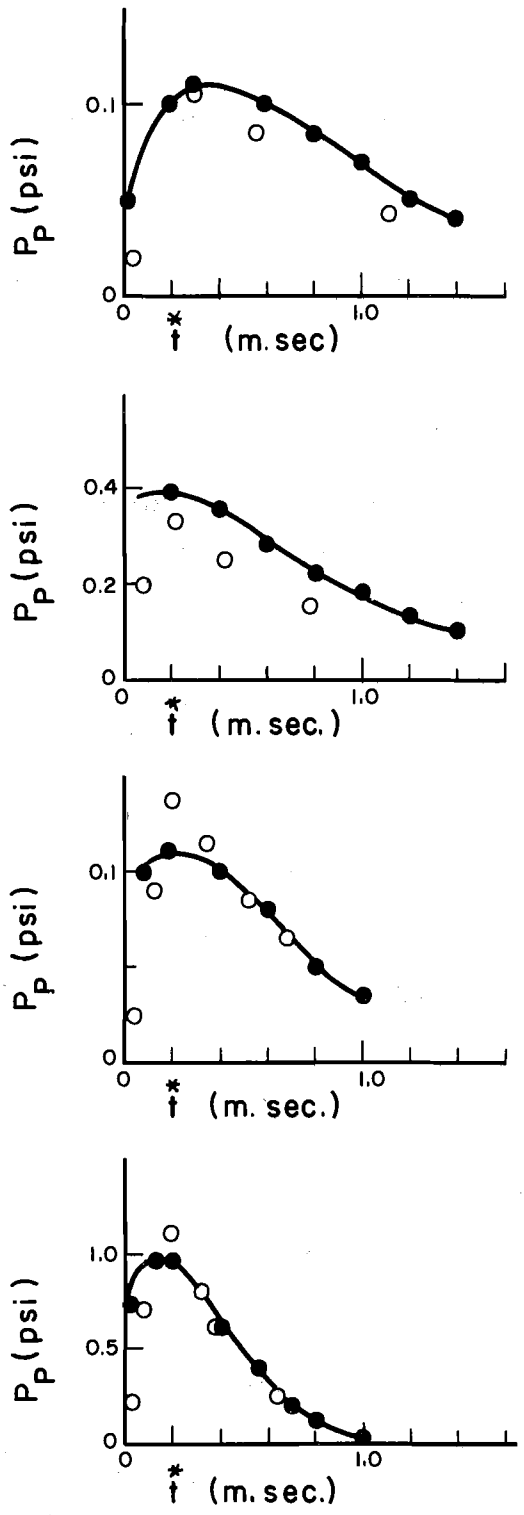

	—●—	o
d (mm)	2.7	2.7
V_o (fps)	15.4	15.4
h (in.)	0.248	0.241

	—●—	o
d (mm)	3.7	3.7
V_o (fps)	28.41	28.41
h (in.)	0.361	0.395

	—●—	o
d (mm)	2.7	2.7
V_o (fps)	25.1	25.1
h (in.)	0.451	0.405

	—●—	o
d (mm)	3.12	3.12
V_o (fps)	26.8	26.8
h (in.)	0.111	0.111

—●— Experimental Result

o Analytical Result

FIGURE 12 (CONTINUED)

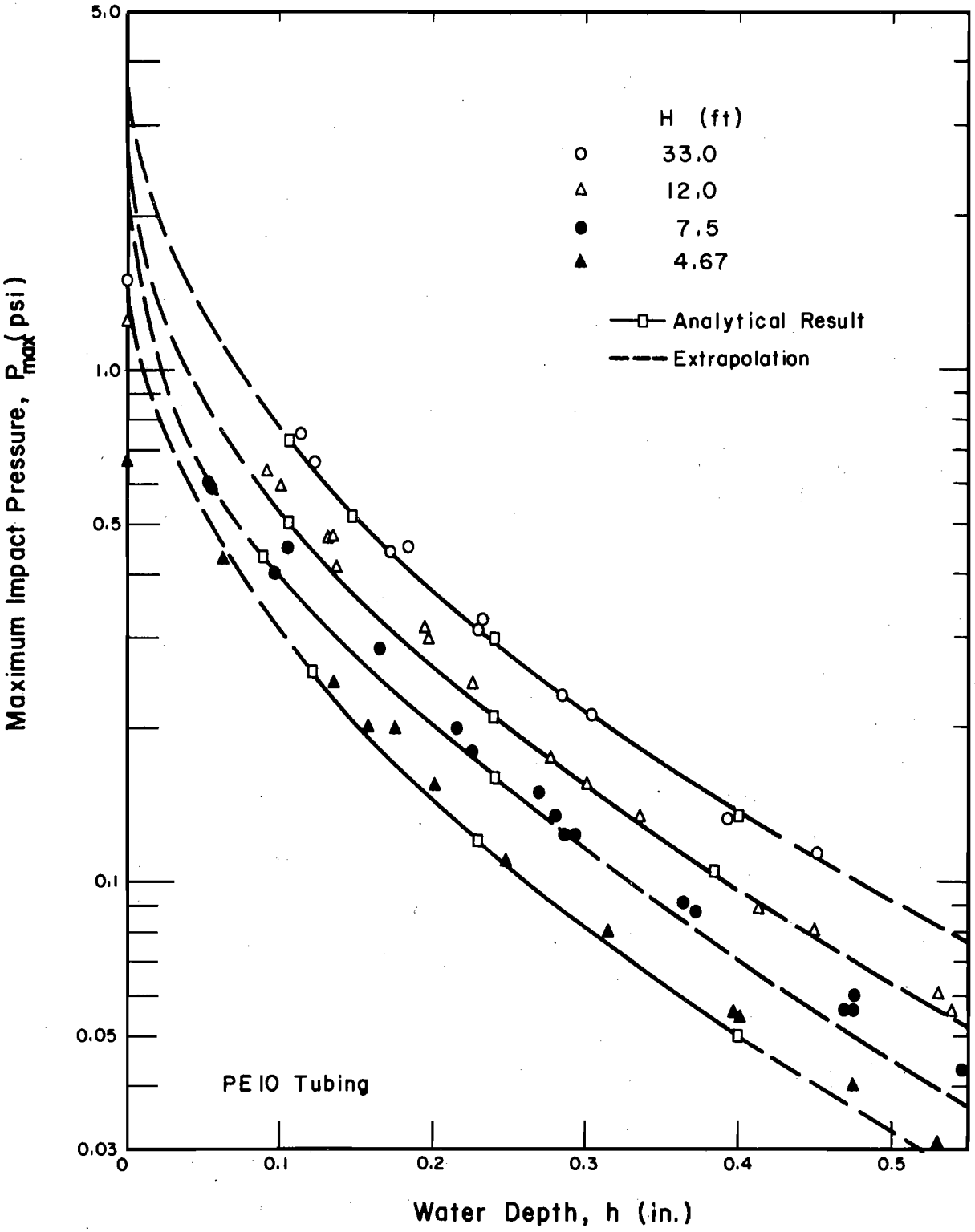

FIGURE 13 MAXIMUM IMPACT PRESSURE VERSUS WATER DEPTH FOR d = 2.7 mm

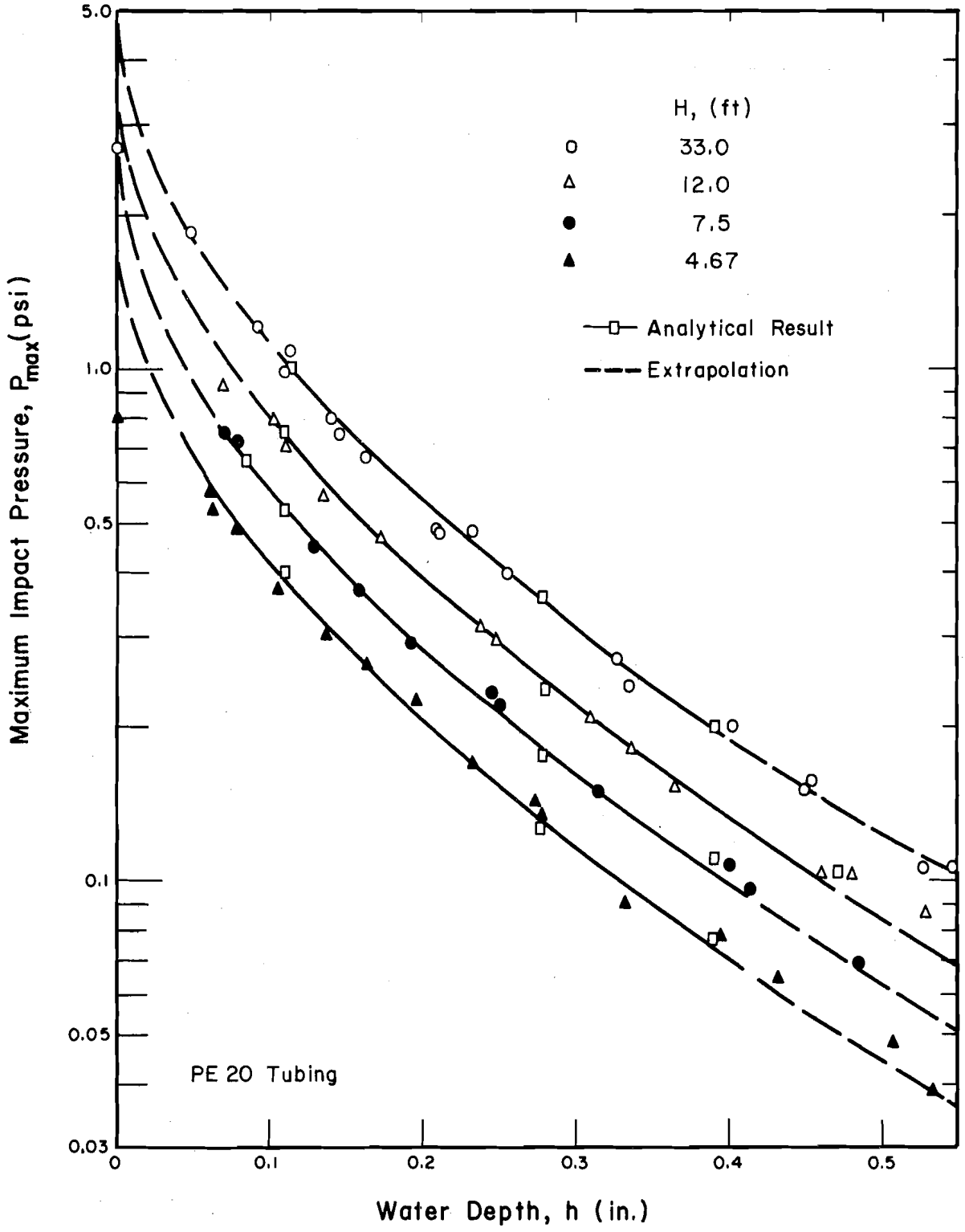

FIGURE 14 MAXIMUM IMPACT PRESSURE VERSUS WATER DEPTH FOR d = 3.12 mm

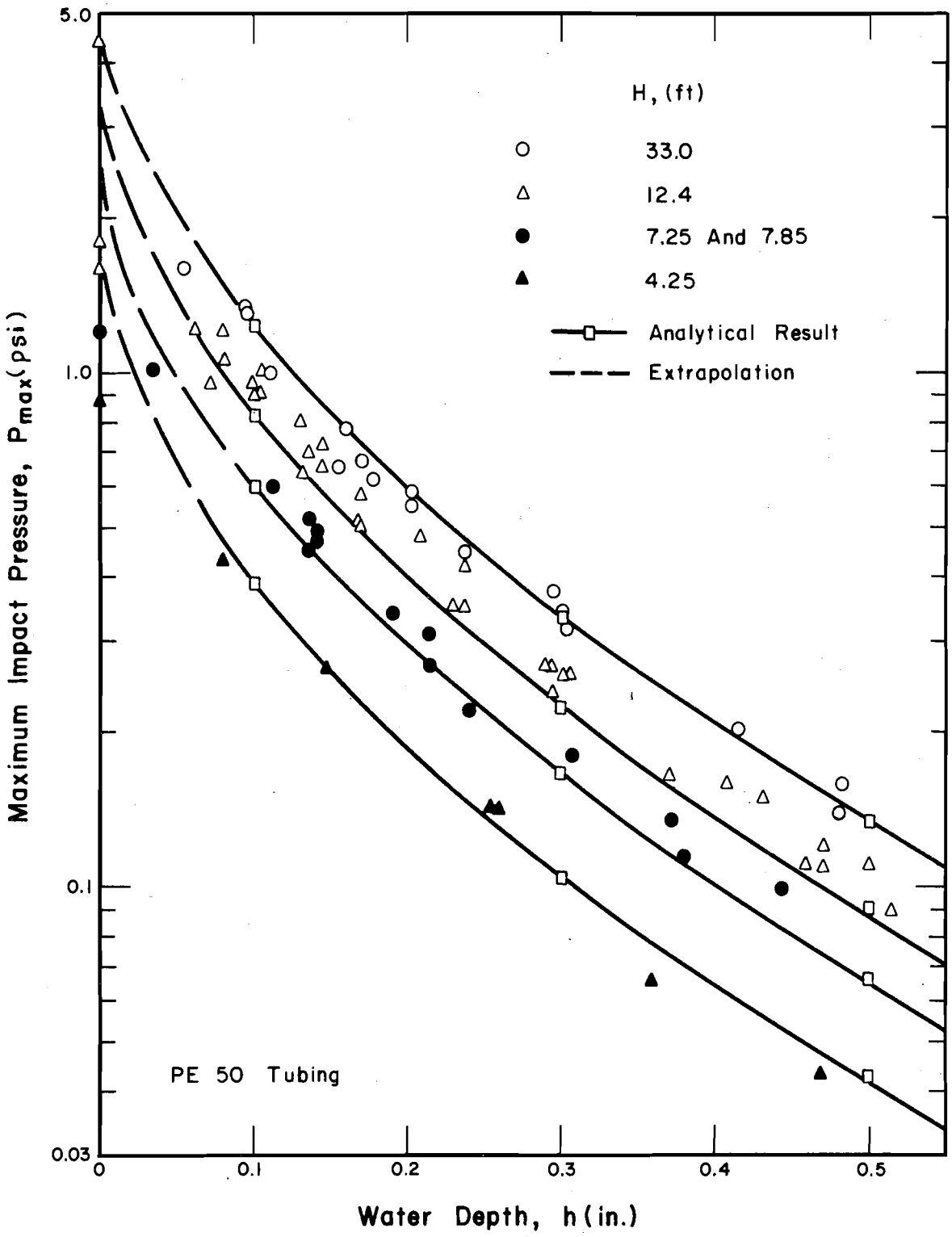

FIGURE 15 MAXIMUM IMPACT PRESSURE VERSUS WATER DEPTH FOR d = 3.12 mm

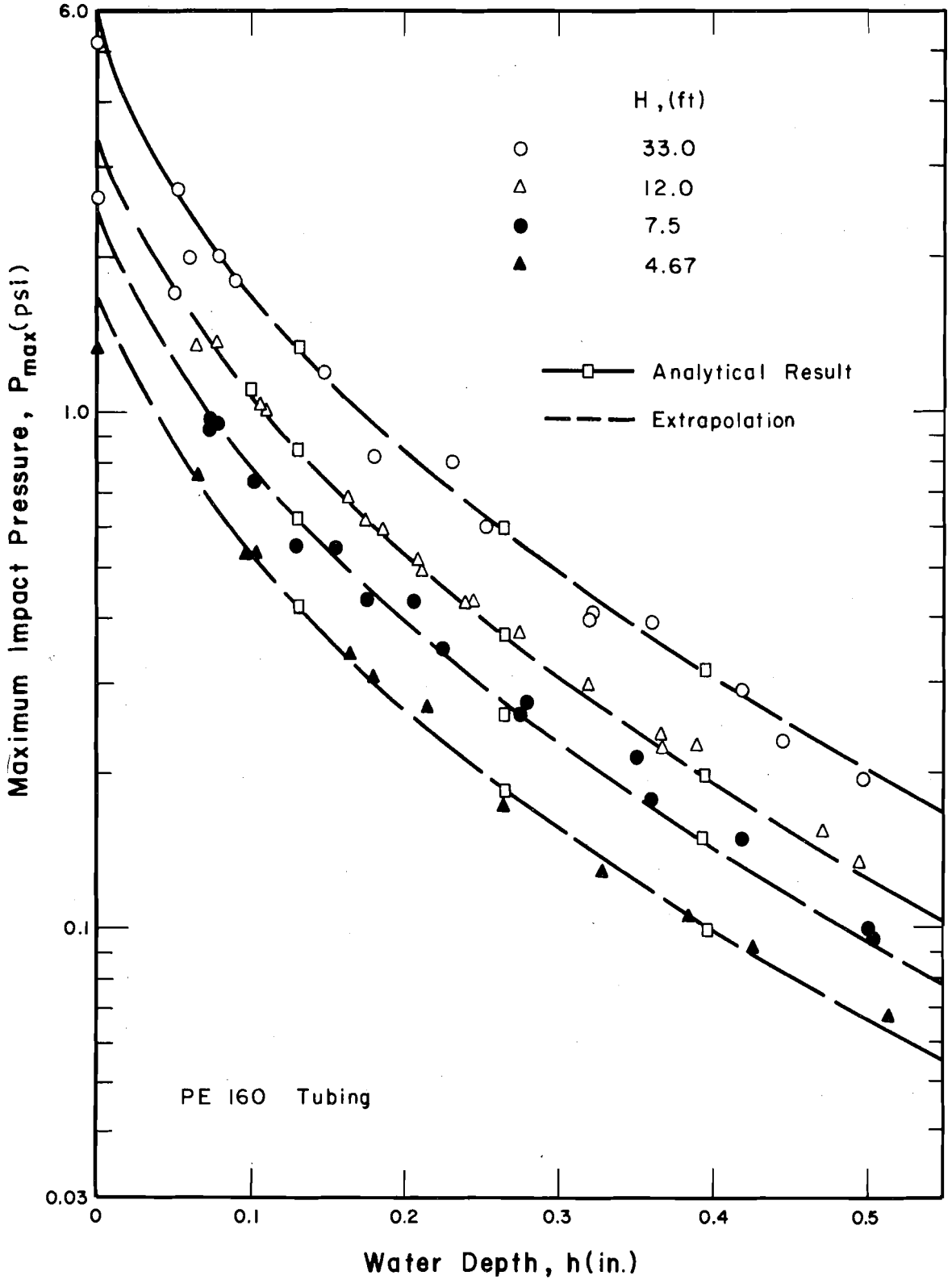

FIGURE 16 MAXIMUM IMPACT PRESSURE VERSUS WATER DEPTH FOR d = 3.7 mm

6.2 Analytical Results

Test drop size and ρ_a = 0.00234 and ρ = 1.935 lb-sec^2/ft^4 were substituted into Eq. 26 to determine the relation between drop fall height and impact velocity. The necessary information for the drop-liquid impact test is tabulated in Table 3. With the given initial conditions of drop size, drop impact velocity, and depth of water layer, the numerical scheme described earlier was used to evaluate the velocity and pressure field as a function of time.

6.2.1 Impact Pressure Pulse

Using the drop sizes and impact velocities given in Table 3, a variation of water layer of 0.1 to 0.5 in., and a spherical shape for 2.7 mm drop and slightly flattened spherical shape reported by McDonald (103) and Mutchler (111) for other drop sizes, the Navier-Stokes equations were solved to give the velocity and pressure field. Pressure values along the bottom of the water layer were then averaged over an area equivalent to the sensing element of the transducer. After subtracting from this average value the static water head, the mathematical simulated impact pressure pulse, $P_p = P - \rho gh$, was obtained. Some typical impact pressure pulses are shown in Figs. 11 and 12, and the pressure field along the bottom of the water layer as a function of time for different impact conditions is tabulated in Appendix D.

6.2.2 Maximum Impact Pressure Versus Water Depth Relation

The peak pressure of the mathematically simulated impact pressure pulse as a function of water layer depth was calculated and plotted in Figs. 13-16 to check the mathematic model proposed.

6.2.3 Velocity Field And Shearing Stress

The velocity field variation with time is shown for two cases in Figs. 17 and 18. Because each run required a long computational time, only these two cases were carried out for the length of time shown. Figure 17 draws the velocity field and free surface configuration at various times for a 2.7 mm drop striking a 0.241 in. deep water layer with a speed of 15.4 fps while Fig. 18 corresponds to a 3.7 mm drop striking a 0.33 in. water layer with a speed of 15.9 fps.

After the velocity field has been calculated, Eq. 14 was used to compute the shearing stress along the bottom of the water layer. Spatial and temporal shearing stress distributions are shown in Figs. 19, 20, and 21. Drop impact conditions are:

Figure	Drop Diameter d (mm)	Water Depth h (in.)	Drop Impact Velocity V_o (fps)
19	2.7	0.241	15.4
20	3.7	0.330	15.9
21	3.12	0.083	18.8

Table 3. Fall Height versus Drop Impact Velocity

Drop Size, d (mm)	Fall Height, H (ft)	Drop Impact Velocity, V_o (fps)
2.70	33.0	25.25
2.70	12.0	21.10
2.70	7.5	18.30
2.70	4.67	15.40
3.12	33.0	26.80
3.12	12.4	22.10
3.12	12.0	21.80
3.12	7.83	19.00
3.12	7.50	18.80
3.12	7.25	18.50
3.12	4.67	15.80
3.12	4.25	15.10
3.70	33.0	28.41
3.70	12.0	22.60
3.70	7.5	19.30
3.70	4.6	15.90

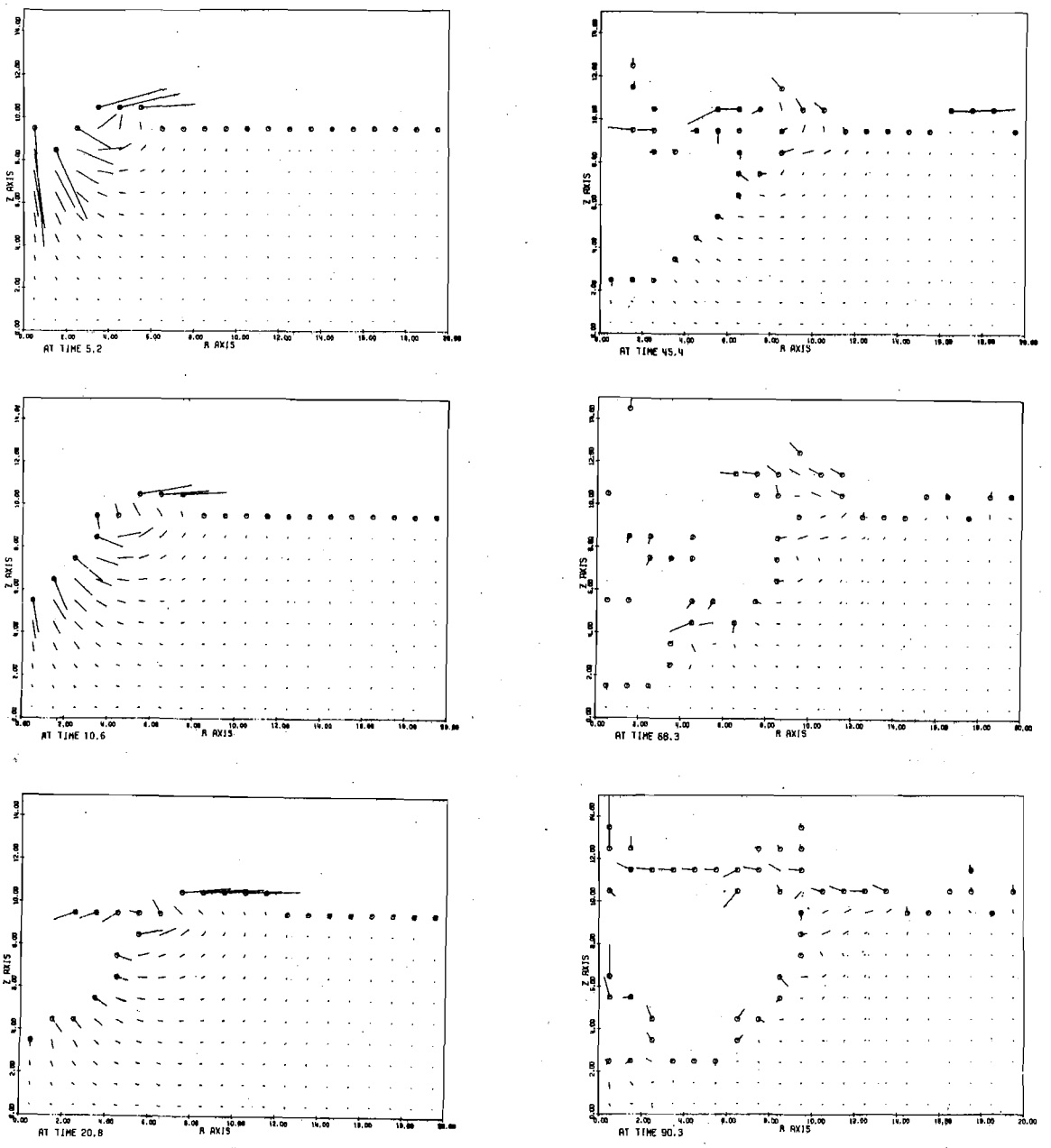

d = 2.7 mm

V_o = 15.4 fps

$\frac{*}{t}/t$ = 0.130 msec

h = 0.241 in.

R = 0.506 in.

L = 0.0241 in.

V_o — Scale

FIGURE 17 VELOCITY VECTOR FIELD

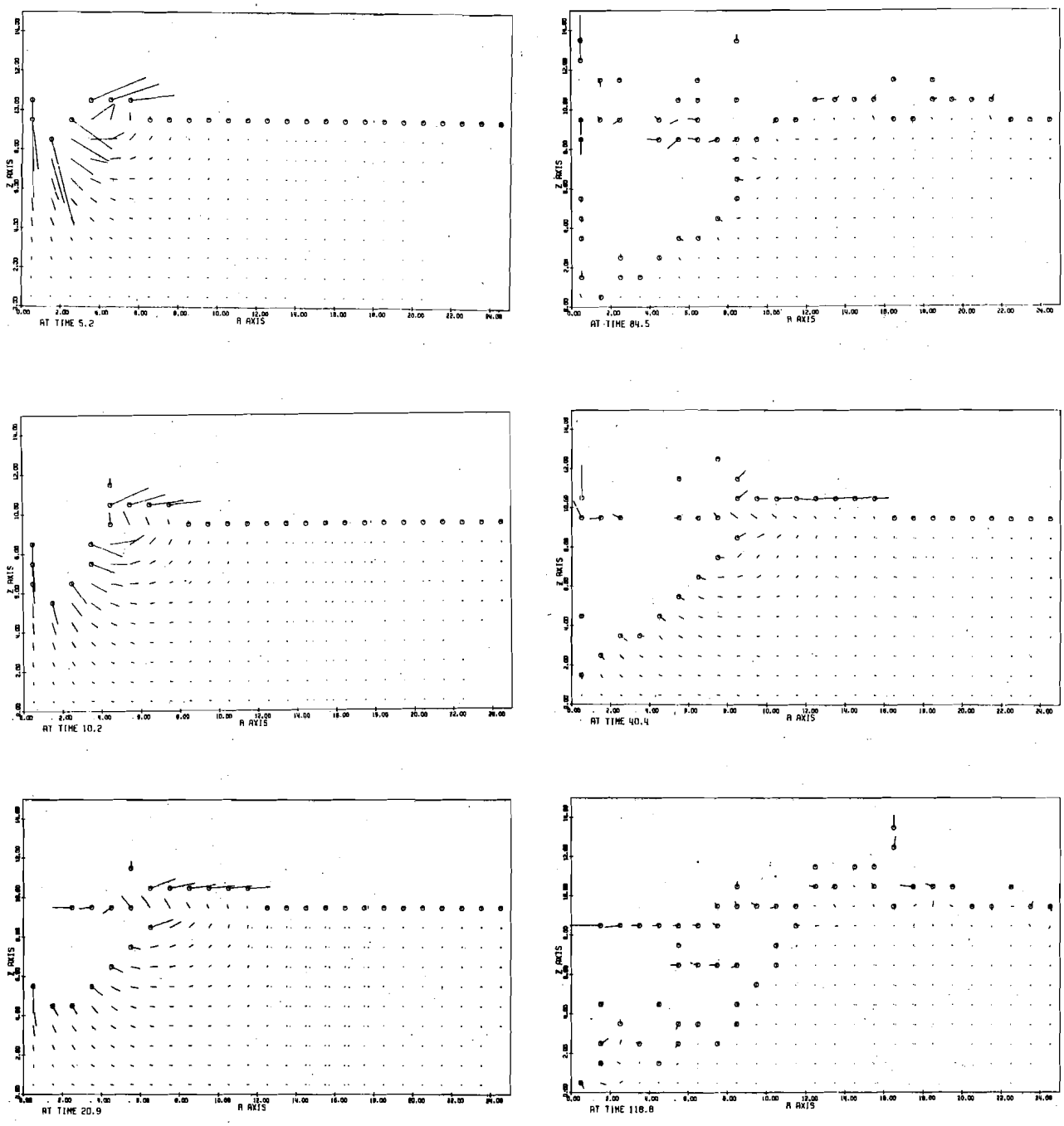

d = 3.7 mm

V_o = 15.9 fps

$\frac{*}{t}/t$ = 0.173 msec

h = 0.33 in.

R = 0.891 in.

L = 0.033in.

V_o / Scale

FIGURE 18 VELOCITY VECTOR FIELD

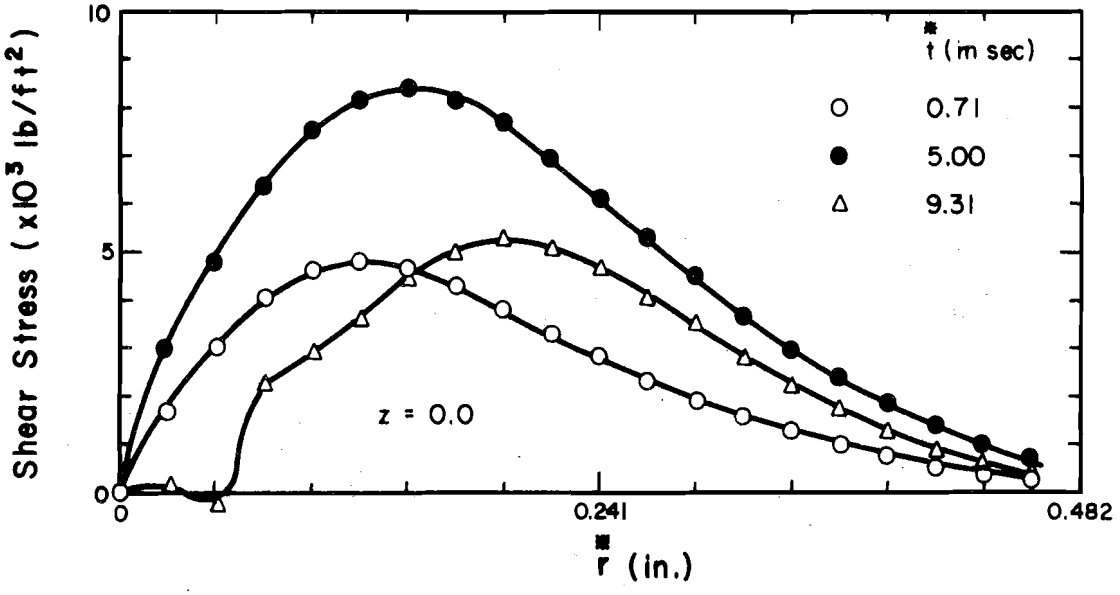

d = 2.7 mm V_o = 15.4 fps h = 0.241 in

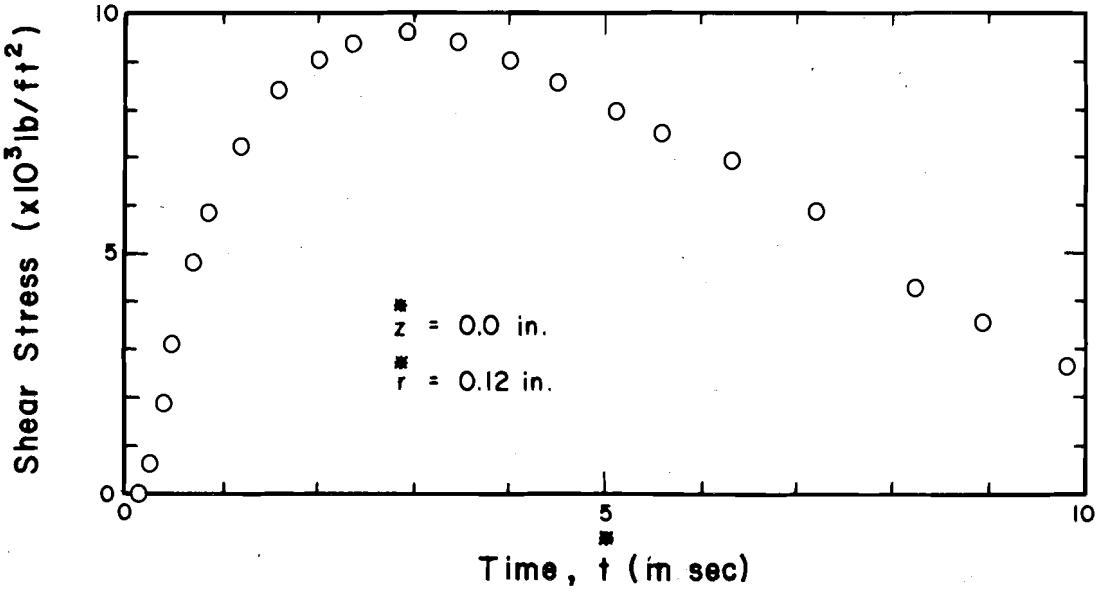

FIGURE 19 SHEARING STRESS FIELD

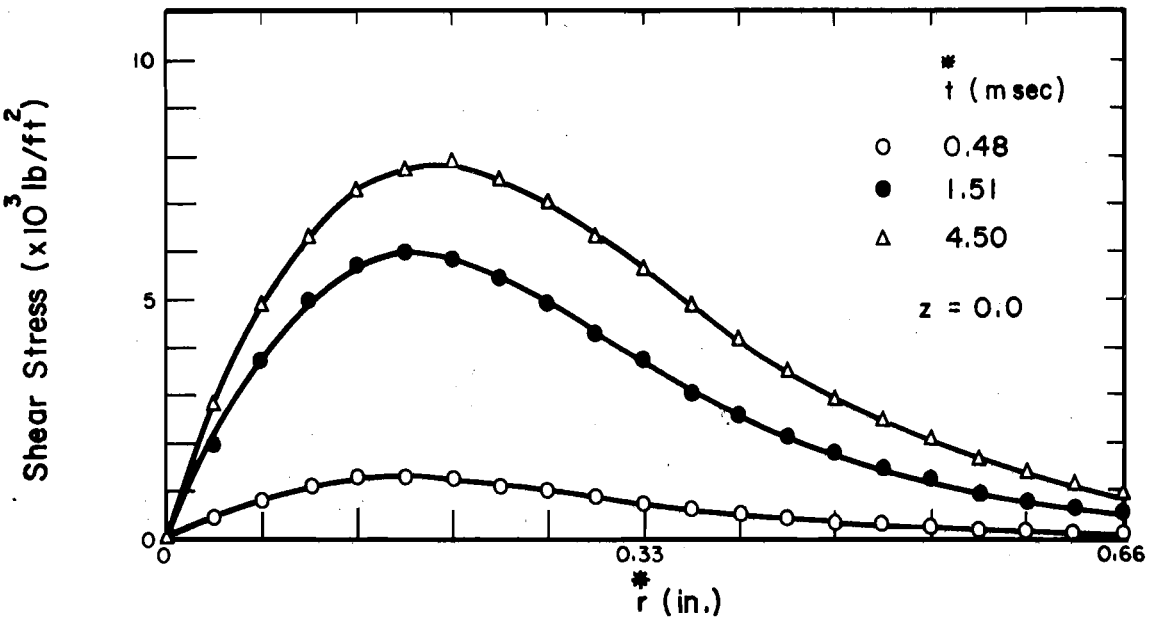

d = 3.7 mm V_0=15.9 fps h = 0.33 in.

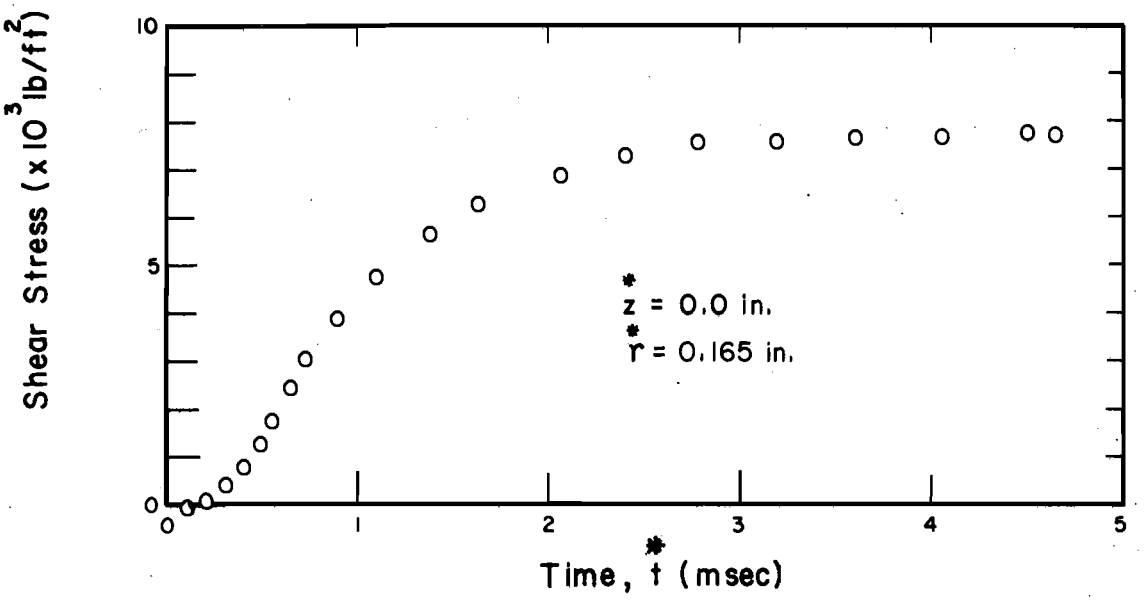

FIGURE 20 SHEARING STRESS FIELD

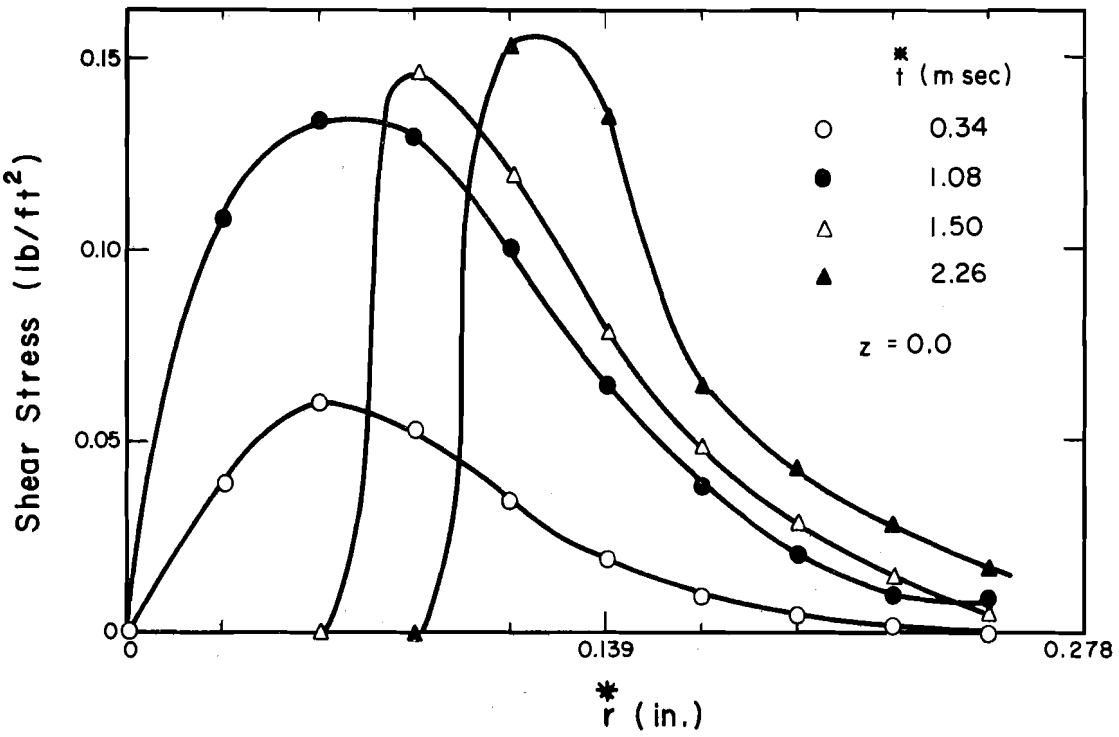

d = 3.12 mm V_o = 18.8 fps h = 0.083 in.

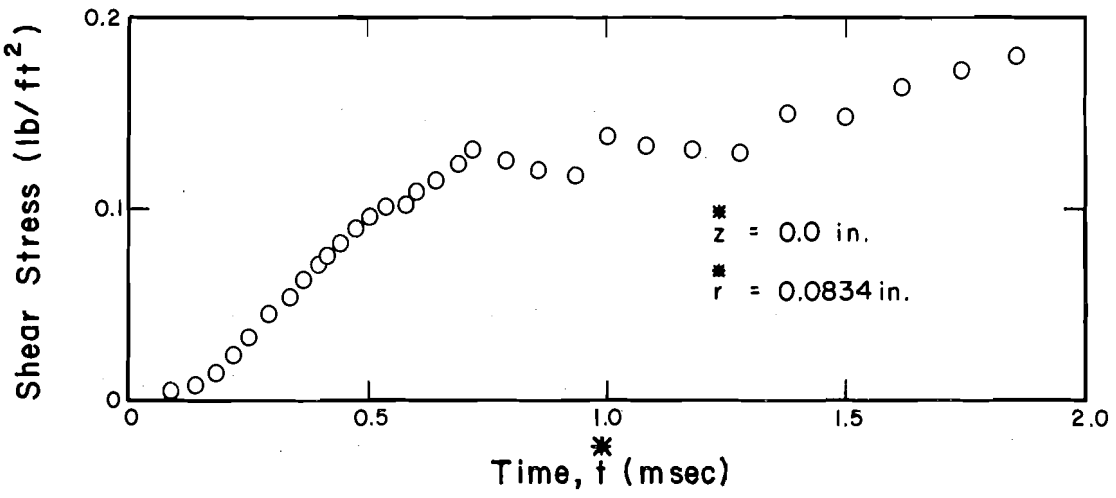

FIGURE 21 SHEARING STRESS FIELD

6.2.4 Free Surface Behavior

The disturbance generated by an impinging drop can best be visualized by observing the free surface configuration as a function of time.

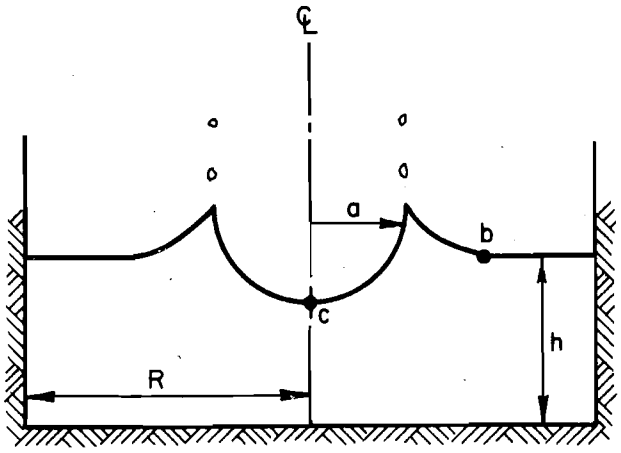

h = Water Depth
R = Radius of Computational Field
a = Crater Radius
b = Crown Tip
c = Crater Center

FIGURE 22 FLUID PATTERN

In Fig. 22, a schematic drawing of the free surface at a specific instant after drop-liquid impact is shown. The concave surface below the drop impact point is called the crater, while the portion of fluid rising above the original water surface is the crown, and the far-reaching point of the crown in the radial direction is called the crown tip. To characterize the fluid movement after drop impact, the time variation of crater radius, a, crown tip, b, and the top position of the crater center, c, are plotted in Figs. 23-25. Drop-liquid impact conditions are given below:

Figure	d (mm)	V_o (fps)	h (in.)	R (in.)
23	3.7	28.41	0.132	0.561
24	2.7	15.40	0.241	0.506
25	3.7	15.90	0.330	0.891

Depth variation as a function of time at several locations from the drop impact point is shown in Fig. 26 to indicate the water surface disturbance produced by a 3.7 mm impinging drop. The initial water layer depth was 0.33 in. while the drop impact speed was 15.9 fps for this case.

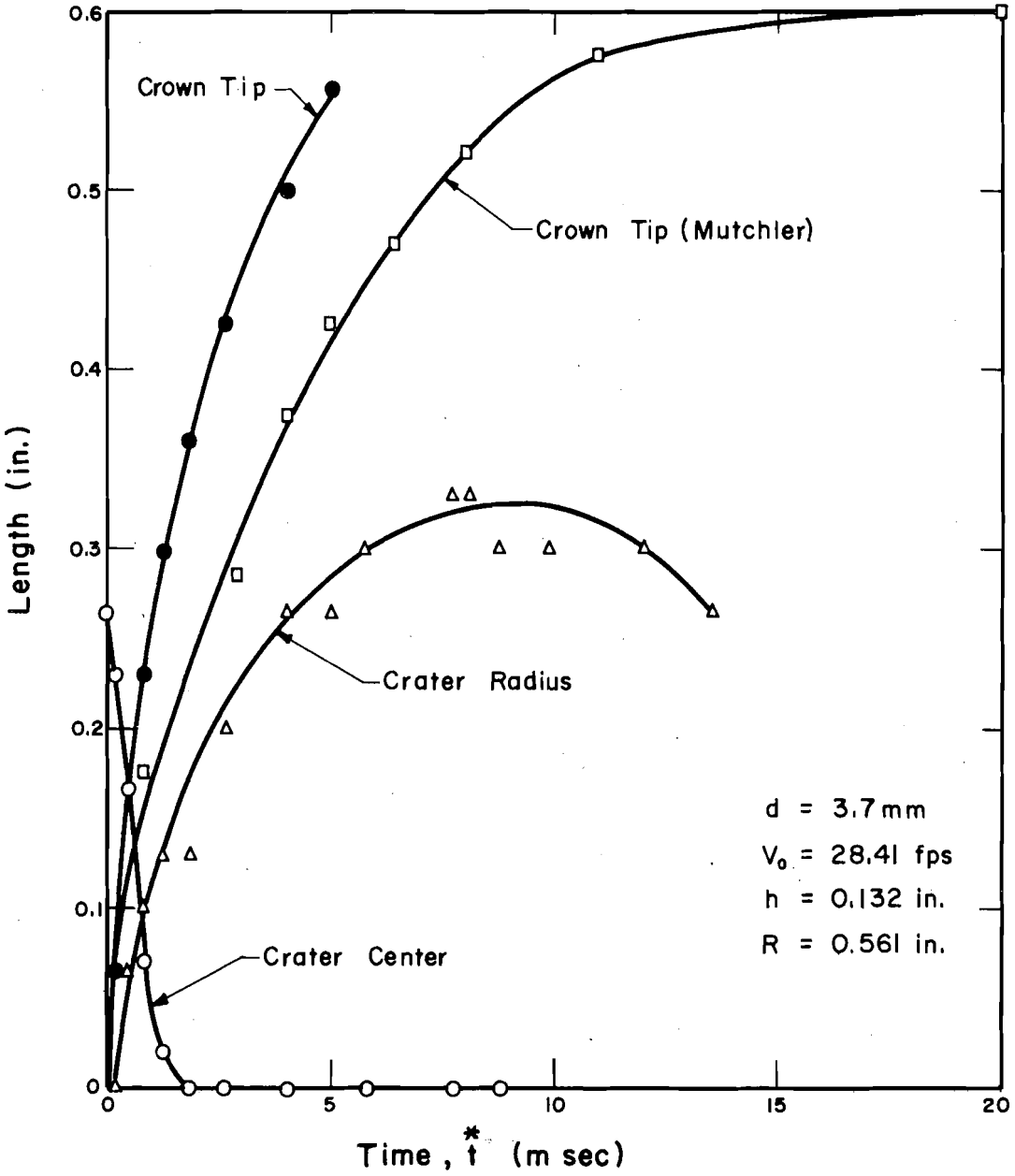

FIGURE 23 FLUID MOVEMENT

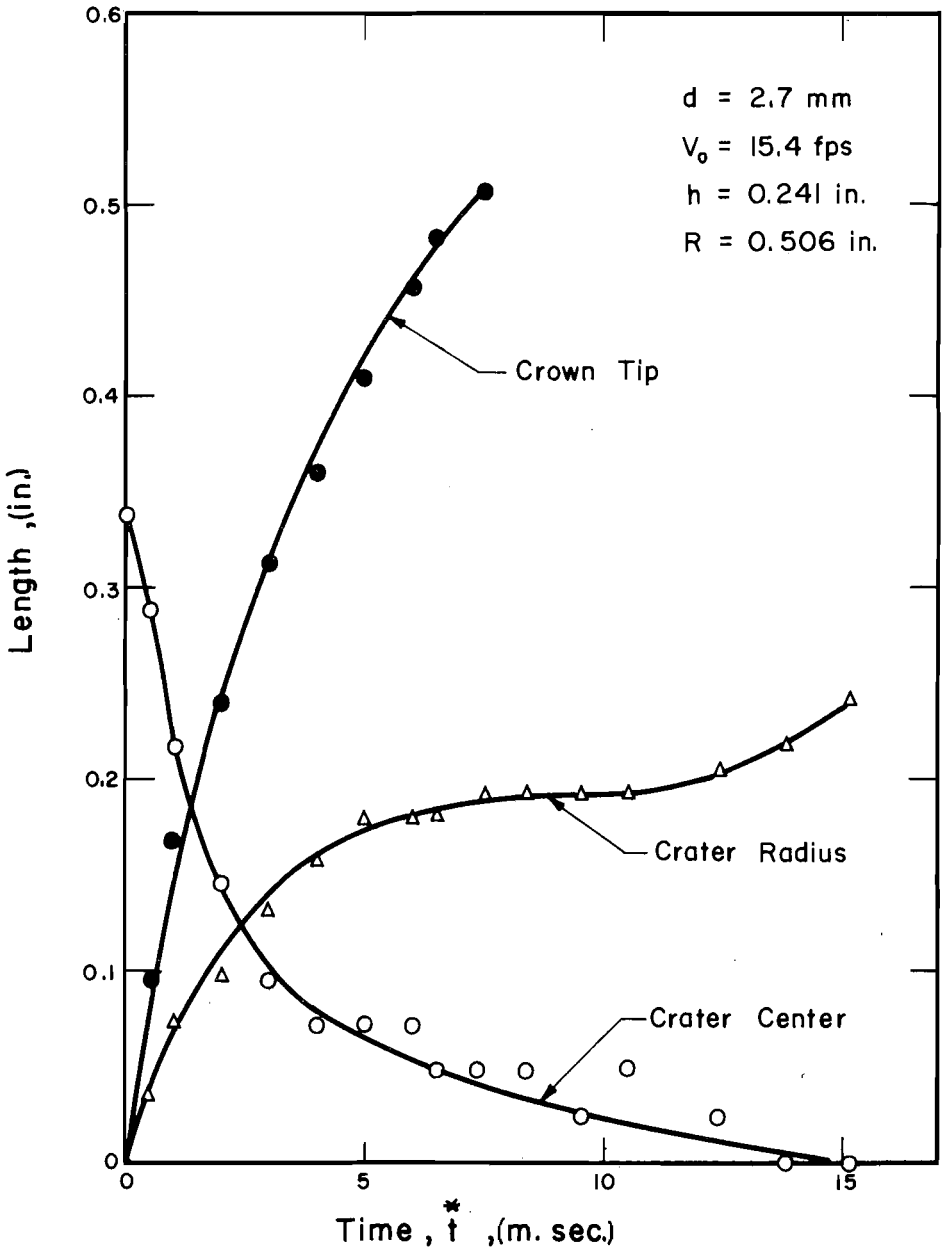

FIGURE 24 FLUID MOVEMENT

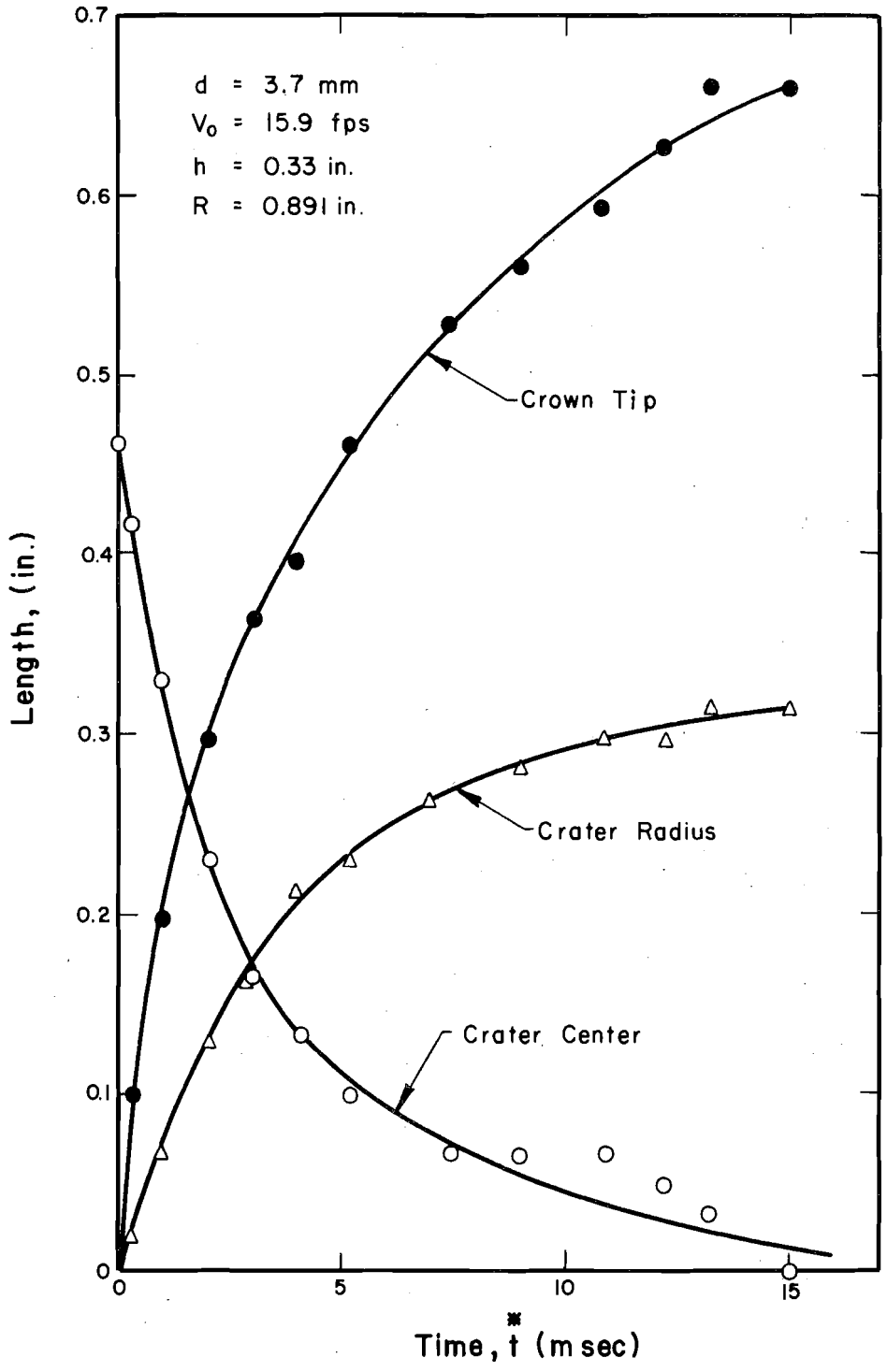

FIGURE 25 FLUID MOVEMENT

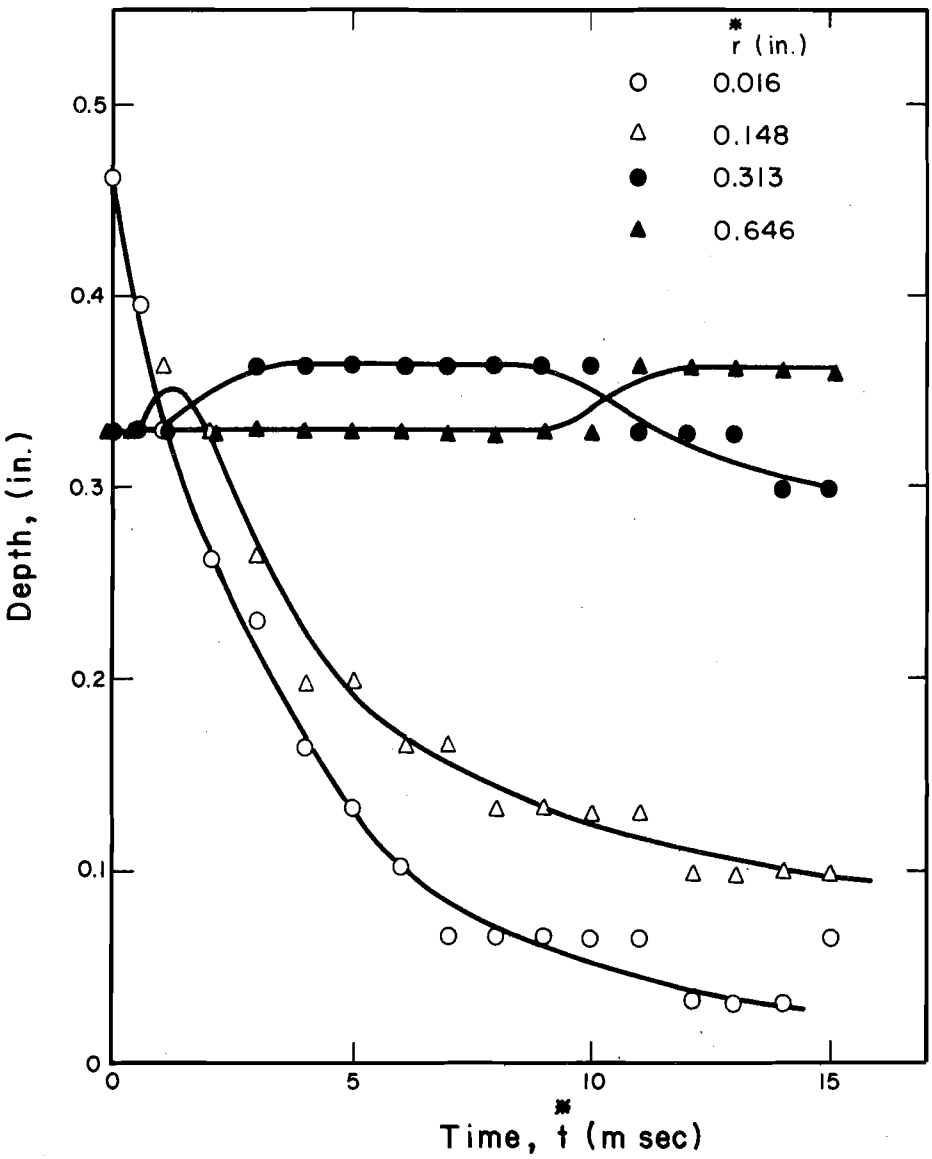

d = 3.7 mm

V_o = 15.9 fps

h = 0.33 in.

FIGURE 26 DEPTH VARIATION

7. DISCUSSION

7.1 Comparison Between Analytical And Experimental Impact Pressure

In Figs. 11 and 12 some typical analytical as well as experimental impact pressure pulses are shown. Qualitative agreement between the two are observed. It should be pointed out that immediately (on the order of microseconds) after the drop touches the water surface, the small contact angle results in a strong surface tension force pulling the water from the drop impact point faster than the numerical scheme can predict with the large cell size used. As a result, the analytical impact pressure pulse tends to rise more slowly than the experimental one. Shown in Fig. 11 is a complete analytical pressure pulse in which the numerical scheme generates an oscillating pressure pulse again because of the large cell size. Therefore, only several representative pressure values are recorded in Fig. 12 and in Appendix D as well.

The time to reach maximum impact pressure, t_p, for each pressure pulse varies randomly from 0.1 to 0.5 msec, and no correlation was attempted. The experimental relationship between t_p and water layer depth, h, is shown in Fig. 27. Its magnitude is in qualitative agreement with the analytical result as shown in Fig. 12. In addition, it should be pointed out that at t_p the velocity field has changed very little from its initial value.

7.2 Comparison Between Analytical And Experimental Maximum Impact Pressure

In Figs. 13-16, maximum experimental impact pressures and those computed using the mathematical model are plotted against the water layer

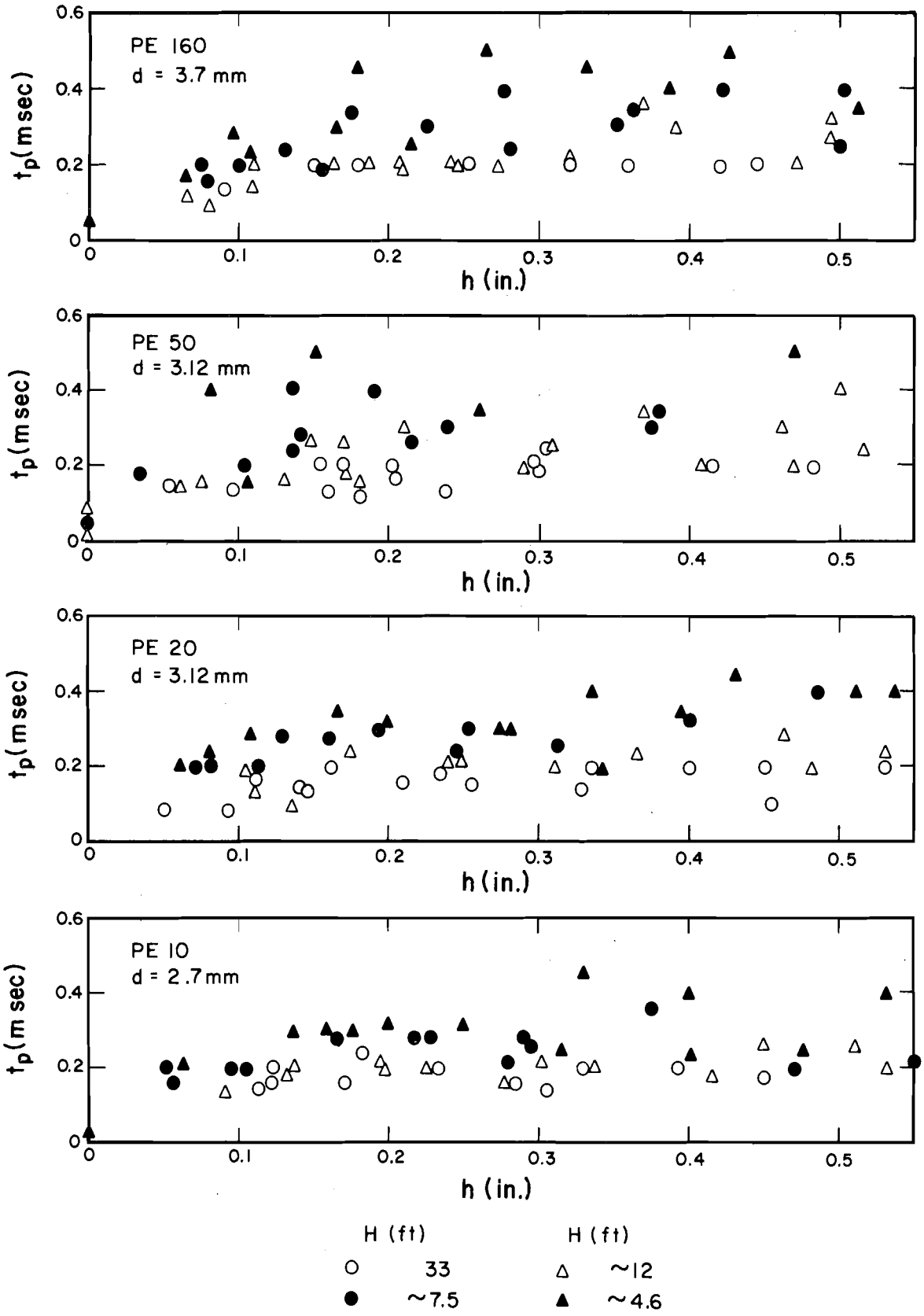

FIGURE 27 t_p VERSUS h

depth for various drop sizes and impact conditions. These results indicate that the maximum impact pressure decreases as the water layer depth increases, and the pressure approaches the hydrostatic value as the depth approaches 1 in.. For example, a 2.7 mm drop with a drop impact speed 18.3 fps has a maximum impact pressure nearly equal to the hydrostatic pressure when the water depth is approximately 0.7 in.. The magnitude of the maximum impact pressure for each specific drop does not vary significantly although the height of fall of the drop varied from 4 ft to 33 ft, essentially because the corresponding drop impact velocity is of the same order of magnitude. The excellent correlation between analytical results and experimental data suggests that the mathematic model used in the present study is capable of solving the drop-liquid impact problem proposed. In Figs. 13-16, analytical results are extrapolated to the stagnant pressure ($0.5\rho V_o^2$) at zero water depth. The experimentally recorded impact pressure however in general did not reach this theoretical point pressure value since the transducer produces a signal which is related to the average pressure over its sensing area rather than the point pressure.

In Figs. 28-31, the dimensionless maximum impact pressure, $2P_{max}/\rho V_o^2$, is plotted against the water layer depth. The correlation suggests that the non-linear part in the equations of motion, Eqs. 6 and 7, does not affect the maximum impact pressure which occurs in the early stages of the impact process if the drop impact velocity is of the same order of magnitude as its terminal velocity.

7.3 Impact Pressure Model

The fact that the non-linear terms in the equations of motion do not affect the maximum impact pressure suggests the existence of a similar

relation between the drop impact pressure and the water layer depth. A dimensional analysis reveals that, after drops striking a water layer at an interval Δt_d, the point pressure P at any point $(\overset{*}{r}, \overset{*}{z})$ in the fluid domain may be affected by the following parameters:

$$\frac{P}{\rho V^2} = \text{function}\left(\frac{\rho V d}{\mu}, \frac{V^2}{gh}, \frac{h}{d}, \frac{\overset{*}{r}}{d}, \frac{\overset{*}{z}}{d}, \frac{V}{V_o}, \frac{V^2}{\Gamma/\rho d}, \frac{\Delta t_d}{\overset{*}{t}}, \frac{\overset{*}{t}}{d/V}, \frac{R}{d}\right) \tag{59}$$

Familiar dimensionless parameters, such as Reynolds number, Froude number, Weber number, and different combinations of length and time variables appear in Eq. 59, although other combinations can be used. For a single drop striking a water layer, Eq. 59 can be rewritten as

$$\frac{P}{\rho V_o^2} = \varphi = \text{function}\left(\frac{\rho V d}{\mu}, \frac{V^2}{gh}, \frac{V^2}{\Gamma/\rho d}, \frac{\overset{*}{t}}{d/V_o}, \frac{\overset{*}{r}}{d}, \frac{\overset{*}{z}}{d}, \frac{h}{d}, \frac{R}{d}\right) \tag{60}$$

At the bottom of the water layer directly below the drop impact point, the magnitude of the dimensionless point peak impact pressure, φ_c, is independent of the coordinate system. It depends simply on h/d and R/d, since velocity is zero at this point. Therefore

$$\varphi_c = \text{function } (h/d, R/d) \tag{61}$$

In the present study, the side wall effect is assumed to be negligible so that φ_c depends only on the water layer-drop size ratio.

$$\varphi_c = \text{function } (h/d) \tag{62}$$

After plotting the point peak impact pressure under the drop impact point obtained analytically against h/d as shown in Fig. 32, a line was fitted to the data.

$$\varphi_c = 0.2\ (h/d)^{-1.825} \tag{63}$$

for $h/d \geqslant 1.0$.

A similar dimensional analysis suggests that the pressure distribution along the water layer bottom when the point peak impact pressure occurs may have a simple relation

$$\varphi/\varphi_c = \text{function}\ (2\overset{*}{r}/h) \tag{64}$$

The analytical results of the pressure distribution upon transformation into these two parameters are plotted in Fig. 33. A least square curve fitting suggests the relation between them to be

$$\varphi/\varphi_c = \text{Exp}\left[- \sum_{i=0}^{4} C_i\ (2\overset{*}{r}/h)^i \right] \tag{65}$$

in which $C_o = -0.00942$

$C_1 = 0.01365$

$C_2 = 0.34312$

$C_3 = -0.04565$

$C_4 = 0.00082$

where φ/φ_c exponentially decreases as $2\overset{*}{r}/h$ increases.

The peak impact pressure distribution for a specific drop impact condition along the water layer bottom can thereafter be predicted from the analytical relation between φ_c and h/d, and between φ/φ_c and $2\overset{*}{r}/h$ as given by Eqs. 63 and 65. For example, a 2.9 mm drop after falling five feet in the air, from Eq. 26, acquires a speed of 16 fps. With this speed, it strikes a water layer with various depth and exerts a maximum pressure whose distribution along the water layer bottom is given by Eq. 65. Upon averaging this pressure over a 1-inch diameter surface area and substituting the point peak impact pressure from Eq. 63, the relation between the water layer depth and the drop impact pressure on a 1-inch diameter area is shown in Fig. 34 to simulate the experimental test conducted by Palmer (114). The large discrepancy between the two may be caused by two factors:

A. The static load calibration used by Palmer: If the frequency of the drop impact pressure pulse, which is about 1250 cycles/sec for a water layer depth of approximately 0.15 in., is higher than that of the strain gage used by Palmer, the static load calibration could result in low pressure value being recorded.

B. The non-uniform response across the surface of the strain gage: The half inch quartz pressure transducer used in this study has a non-uniform response across its surface. It would not be reasonable to expect a uniform surface response from the center to the edge of a 1-inch diameter foil-type spiral strain gage used by Palmer.

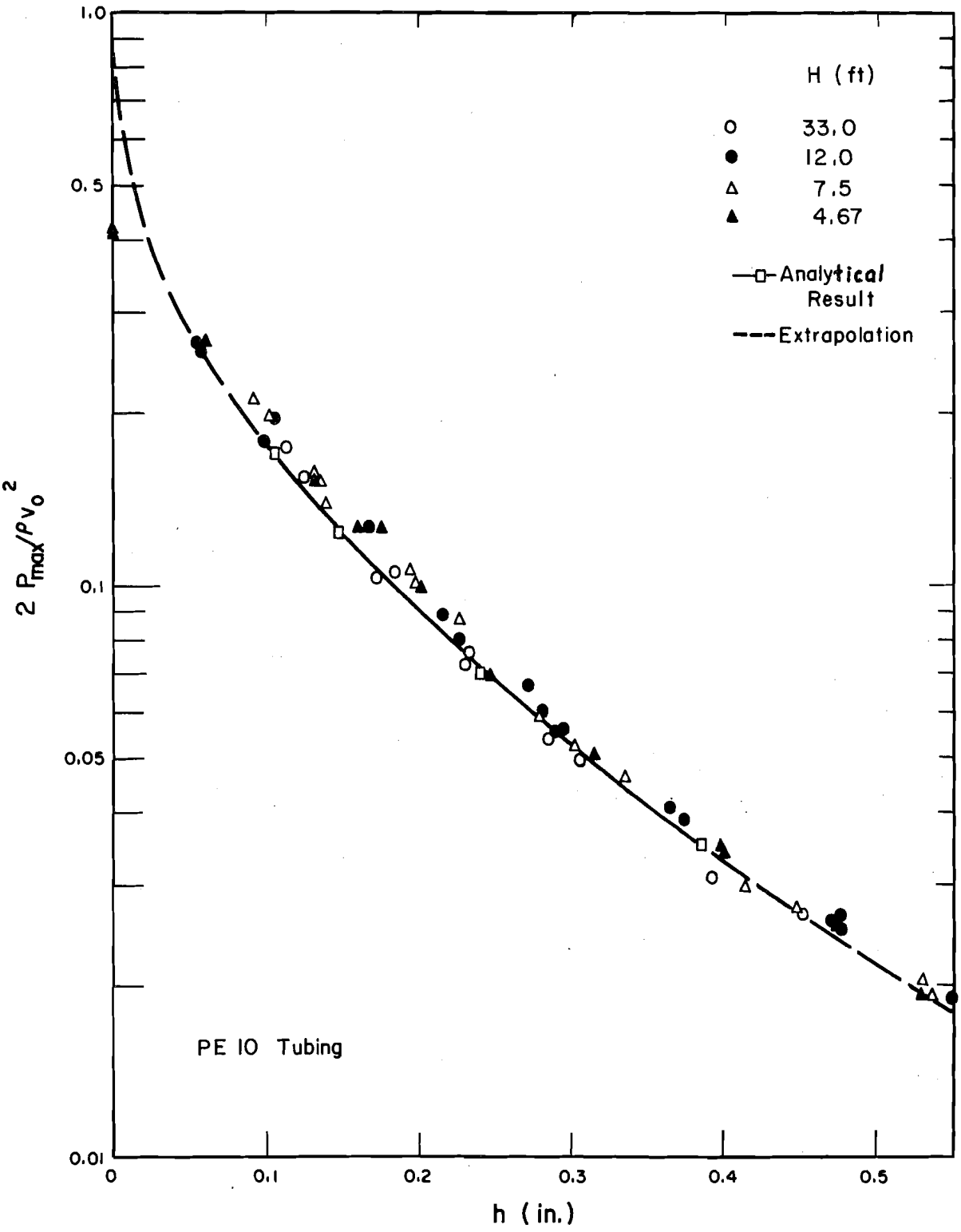

FIGURE 28 DIMENSIONLESS MAXIMUM IMPACT PRESSURE VERSUS WATER DEPTH FOR d = 2.7 mm

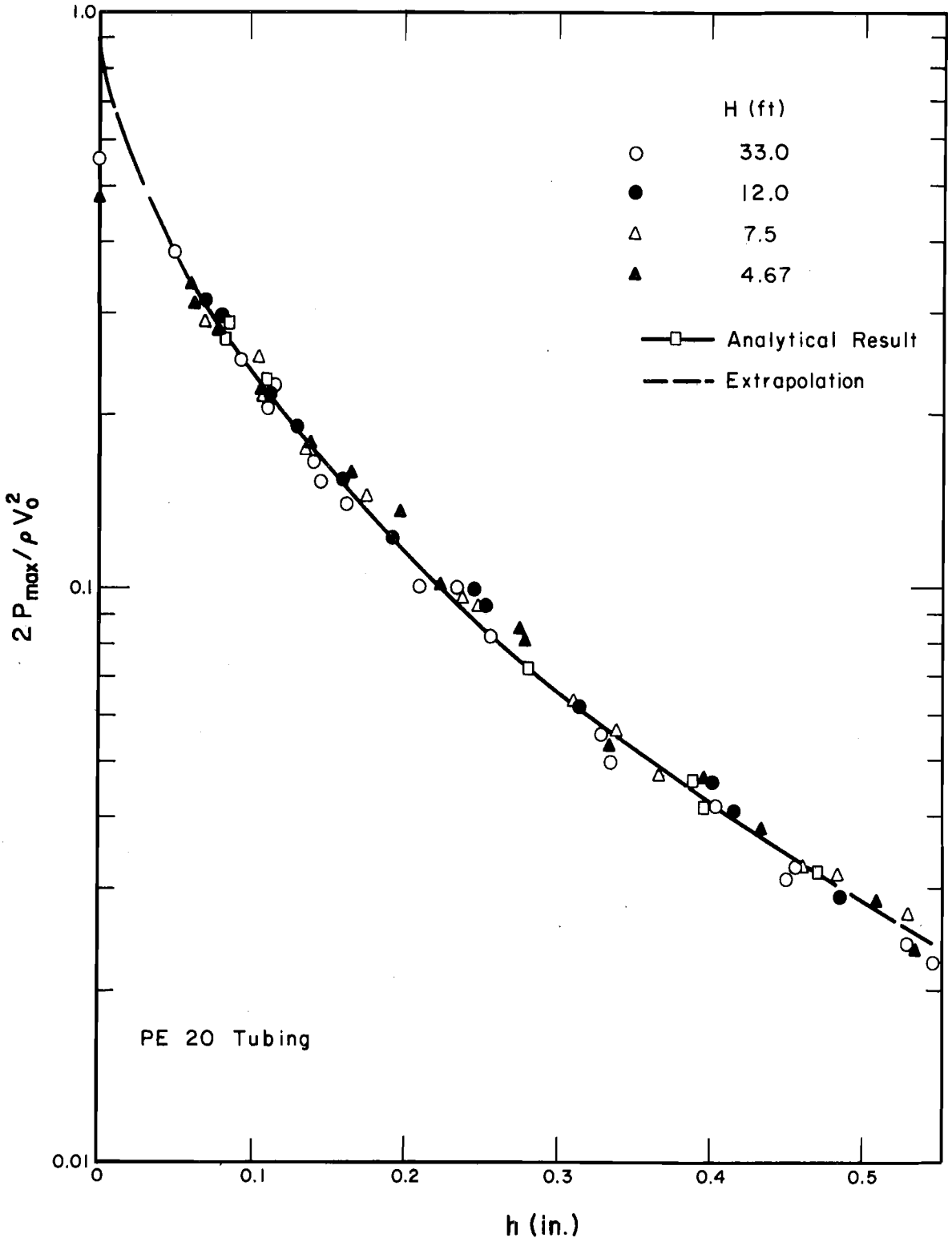

FIGURE 29 DIMENSIONLESS MAXIMUM IMPACT PRESSURE VERSUS WATER DEPTH FOR d = 3.12 mm

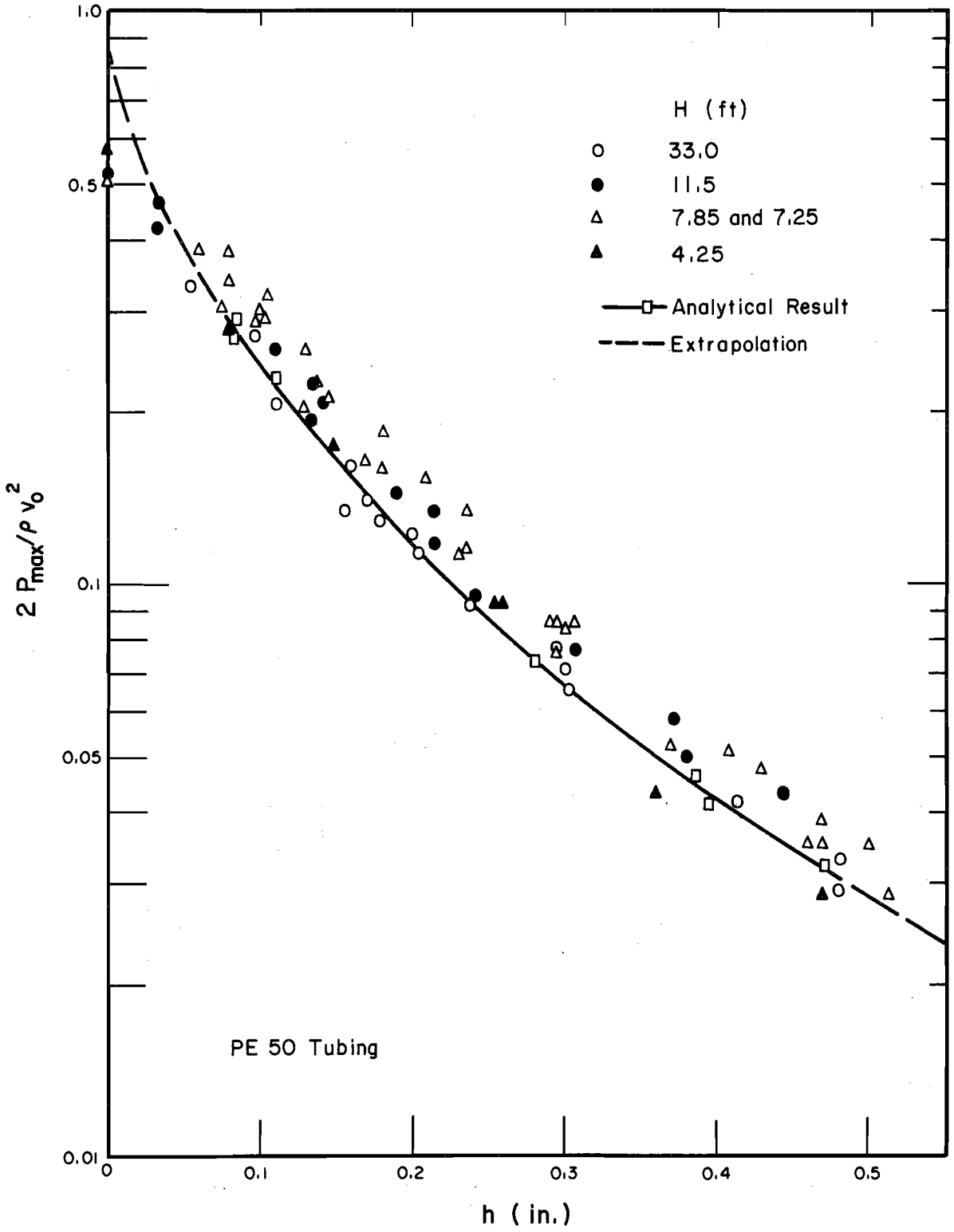

FIGURE 30 DIMENSIONLESS MAXIMUM IMPACT PRESSURE VERSUS WATER DEPTH FOR d = 3.12 mm

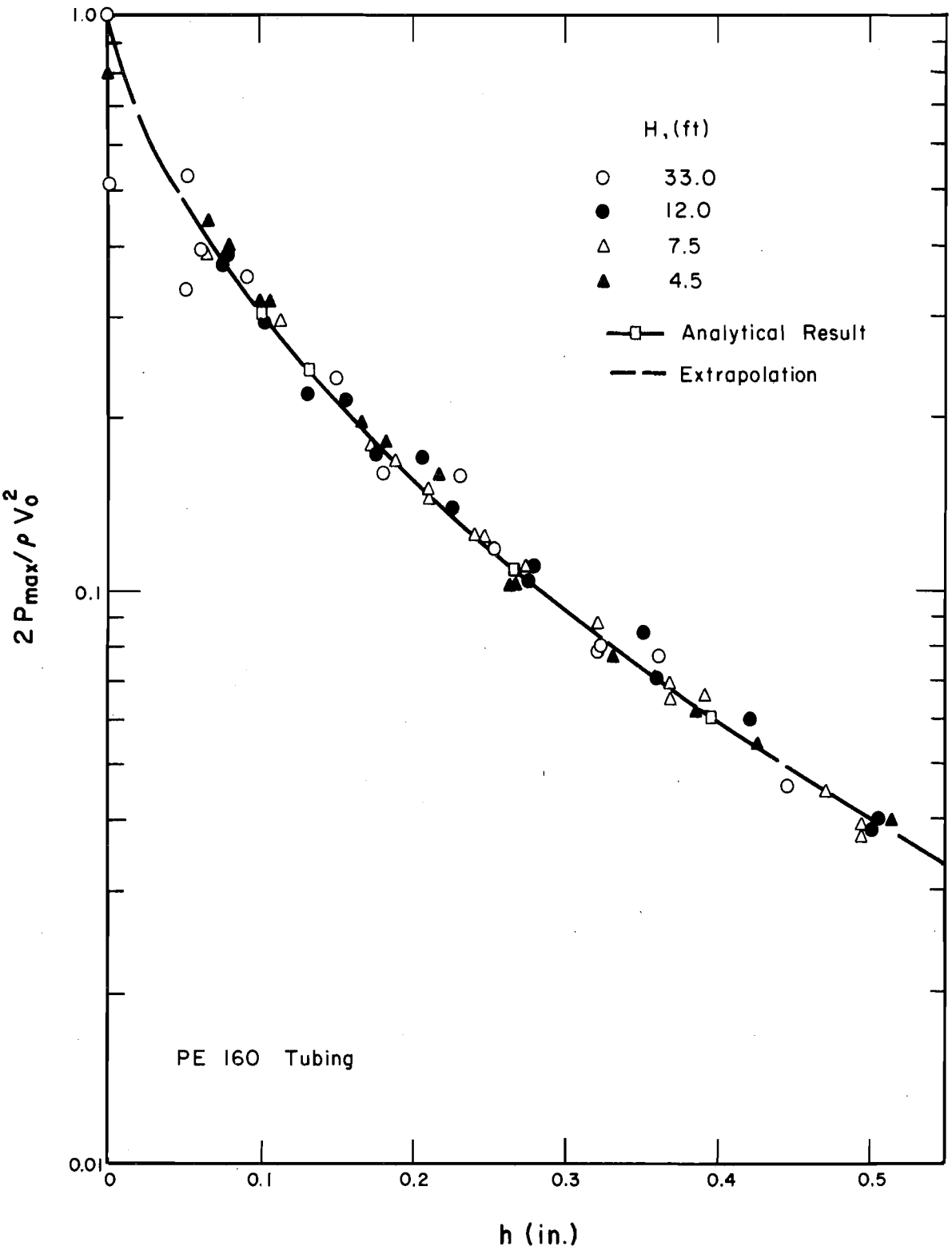

FIGURE 31 DIMENSIONLESS MAXIMUM IMPACT PRESSURE VERSUS WATER DEPTH FOR d = 3.7 mm

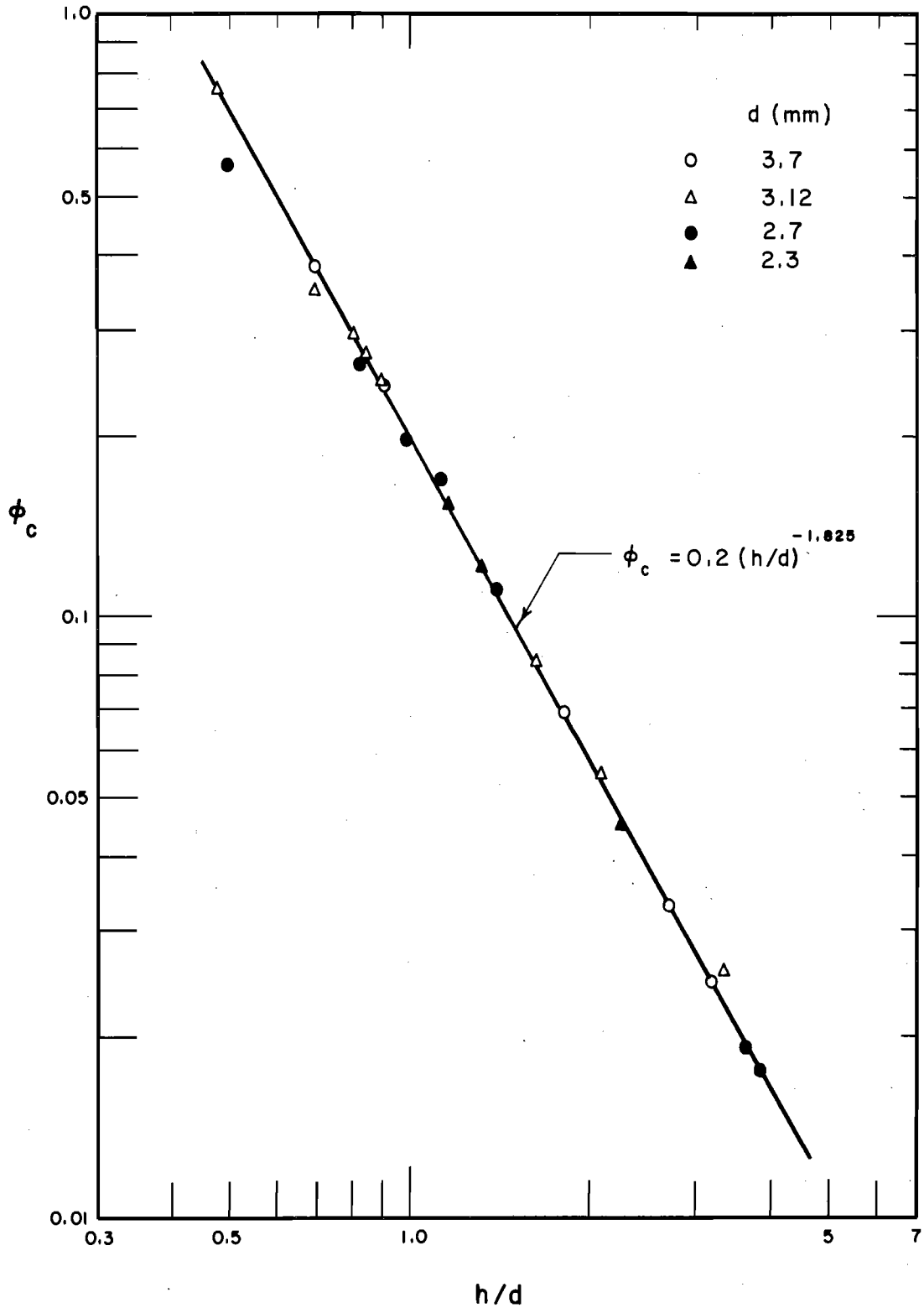

FIGURE 32 ϕ_c VERSUS h/d

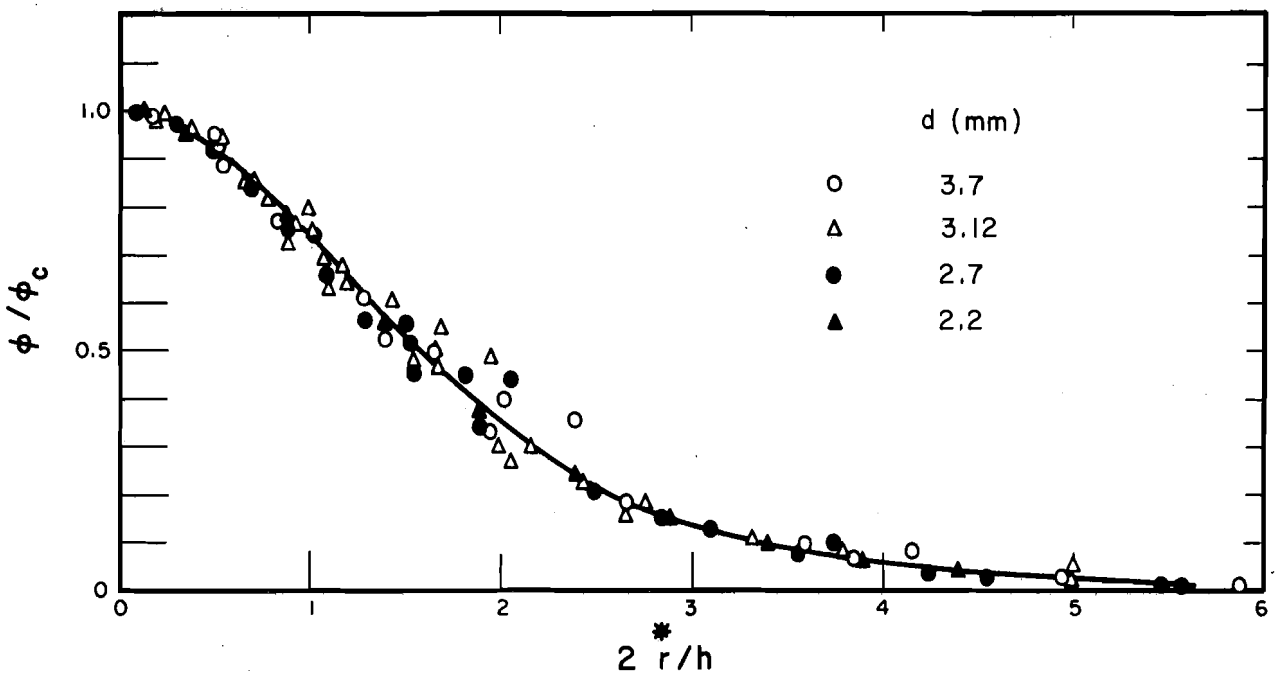

FIGURE 33 ϕ/ϕ_c VERSUS $2\overset{*}{r}/h$

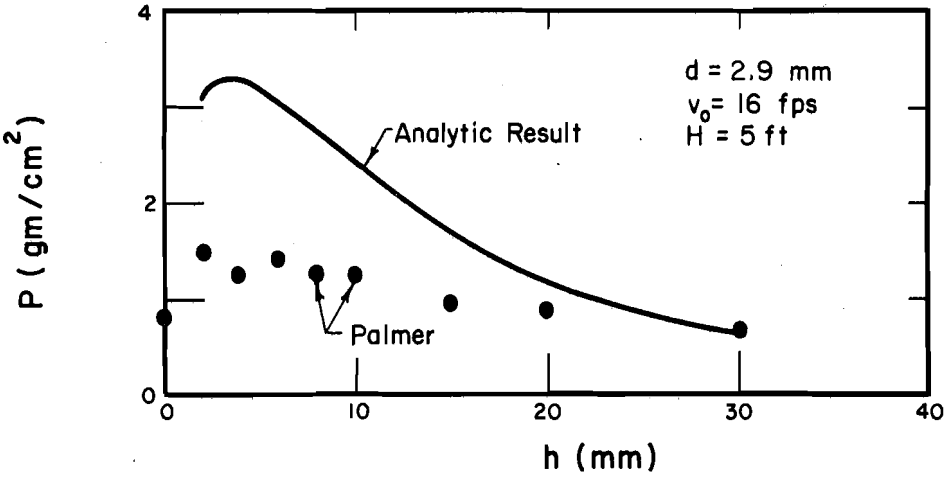

FIGURE 34 PRESSURE VERSUS DEPTH

7.4 Vertical Pressure Distribution

In Figs. 35 and 36, the vertical pressure distributions for two drop sizes at four vertical cross sections, r = 1, 5, 10, and 20, are plotted at three time stages: one before, one near, and one after the time when maximum impact pressure occurs at the bottom of the water layer. The hydrostatic point pressure distributions are also displayed at r = 20 in both figures.

Near the drop impact point, the point pressure increases sharply to its maximum value below the free water surface and then decreases toward the bottom. Due to the direct impact of the impinging drop, the pressure magnitude is substantially higher than that of the corresponding hydrostatic pressure. For example, the peak pressure in Fig. 35 is about 600 times its corresponding hydrostatic pressure. Although this is the case near drop impact point, the pressure distribution has the general shape of the hydrostatic distribution far away from that point. At r = 20, which is approximately one half inch from the drop impact point, the pressure value differs little from its corresponding hydrostatic pressure. It should be pointed out that near the drop impact point the spatial pressure distributions are similar to each other before the maximum impact pressure occurs as shown in Figs. 35 and 36. Their shapes are similar to those reported from breaking water waves (134).

In analyzing shallow overland flow problems, an over-pressure concept which assumes an additional dynamic pressure in analyzing the flow problem was mathematically introduced to account for the drop impact effect by some researchers (23, 53). This study points out that the pressure away from drop impact point remains hydrostatically distributed during the drop

splashing process. Even under the drop impact point, the high dynamic pressure only lasts 1 to 2 msec before it falls to a value of the same order of magnitude as the initial hydrostatic pressure. This time interval is rather short as compared with the time interval between successive drops in natural rainfall. For the drop pattern used in the O.W.R.R. project, the interval between drop impacts is approximately 0.42 sec for a 10 in./hr rainfall. Thus, it suggests that the over-pressure concept does not present a theoretically accurate description under the condition of a series of single drops striking one point.

7.5 Velocity Field And Shearing Stress

In overland flow with rainfall, drops after striking the surface water layer distribute into it and generate a local disturbance which results in high resistance to flow. Thus, the velocity field after drop-liquid impact is one of the important factors in studying the drop-liquid impact process. In Figs. 17 and 18 sequences of velocity vector fields are displayed from initial impact up to the time when the crater approximately reaches its maximum size. Lines radiating from the center of each computational cell indicate both the direction and magnitude of the velocity and constitute the instantaneous velocity vector field. Fluid below the drop impact point tends to flow downward and outward, while fluid around it tends to flow outward and upward. These motions combine to form a crater below and a crown around the drop impact point. Of those drops studied, the fluid field was significantly disturbed by the impinging drop in a diameter approximately 1-inch below the drop impact point. This result is in agreement with the high resistance force reported by Wenzel

et. al. (137) caused by drops spaced 1-inch apart impinging on sheet flow less than one inch deep.

The spatial shear stress distribution along the bottom of the water layer as well as the shear stress time variation at a specific distance from the drop impact point for three different cases is shown in Figs. 19, 20, and 21. These figures show a relatively high shear stress whose magnitude increases as the crater size increases. For example, the permissible unit tractive force for canals in noncohesive material reported by U.S. Bureau of Reclamation (25) is approximately 0.04 lb/ft^2 for particles of average diameter of 1 mm. Whereas the maximum shear stress below a 0.083 in. deep water layer is 0.18 lb/ft^2 as shown in Fig. 21. It should also be pointed out that for a uniform sheet flow of a depth of 0.083 in. on a surface with a 1% slope, the shear stress exerted by the flow is only 0.00432 lb/ft^2 with no rainfall present. Thus, the rainfall in this case increases the boundary shear by a factor of approximately 42.

When the crater reaches its maximum size, the kinetic energy of the fluid reaches a minimum. Thereafter, the fluid around the crater flows radially inward to the crater center to form a Rayleigh jet (67, 68, 146). This back flow phase was not studied because of the large amount of computer time required. This backward fluid motion caused a radially inward shearing force which together with the initial outward shearing force could loosen any soil particles in the impact region, thus initiating the soil erosion process. The maximum shearing force occurs around the edge of the maximum crater directed radially outward suggesting that the soil erosion there is the strongest.

7.6. Drop-Liquid Impact Behavior

After a drop strikes a stagnant water layer, a high pressure is momentarily exerted on the water surface. This high pressure, as well as the drop itself, is then distributed into the water layer. The pressure and velocity fields due to this process generate a local disturbance which is characterized by the crater forming below the water surface and a crown emerging above around the drop impact point. Small droplets are ejected from the crown edge. As the kinetic energy of the system decreases, the crater enlarges until it reaches its maximum size. The newly acquired potential energy as well as the surface energy thereupon cause a water column, which may or may not release small droplets, to rise from the center of the crown. After it subsides small ripples spread outward in an ever-widening circle (68, 146). To simulate this drop-liquid impact process, the mathematical model proposed earlier was solved.

The time history, as determined from the mathematical model, of the behavior of the crater radius, crown tip, and the center position of the crater after a 2.7 mm drop strikes a 0.241 in. deep water layer with an impact speed 15.4 fps is shown in Fig. 24. Some characteristic information are given below:

maximum crater radius = 0.194 in.
maximum crater depth $>$ 0.241 in.
time to reach maximum crater radius $\simeq$ 15 msec

For purposes of comparison experimental data obtained by Engel (42) for a 2.76 mm drop striking a large water pool with an impact speed of 13.1 fps is given below:

maximum crater radius = 0.223 in.
maximum crater depth = 0.286 in.
time to reach maximum crater radius = 13.9 msec

The analytical results show qualitative agreement with Engel's experimental work. The difference between the two crater radii could be due to the finite boundary wall superimposed at a radius 0.506 in. from the drop impact point (102). The bottom of the tray was exposed in the analytical study, therefore the maximum crater depth could be greater than 0.241 in. should the water layer depth be greater than 0.241 in. (98). The crown tip behavior also shows a qualitative agreement with the photographic data obtained by Mutchler* of a 2.9 mm drop striking a 0.114 in. water layer with a speed of 25.6 fps.

While the maximum impact pressure occurred within 0.6 msec after drop impact for the cases studied, subsequent fluid motion lasts much longer. By forming a crater and a crown as well as a possible rebounding water column at a later stage as described above, the impinging drop significantly disturbs the originally stagnant water layer. The crater depth and width are an indication of the region of maximum disturbance, and it has been suspected (42, 43) that these dimensions depend on the kinetic energy of the impinging drop. However, a general relationship describing the crater geometry was not attempted because of the large amount of computer time required. It is believed the mathematical model could be used for this purpose given sufficient computer time.

In Fig. 23, the drop-liquid impact behavior of a 3.7 mm drop striking a 0.132 in. deep water layer with an impact speed 28.41 fps is shown. Approximately 5 msec after drop impact, the crown tip reaches the

*The photographic data were obtained by analyzing a high speed drop-liquid impact film borrowed from Mr. Calvin K. Mutchler, Agricultural Engineer, Soil and Water Conservation Research Division, Morris, Minnesota.

solid boundary wall which is 0.561 in. from the drop impact point. Furthermore, no water is present below the drop impact point at approximately 2 msec. These data indicate that the crater depth and crown tip radius could be greater should there be no physical boundary. The crown tip history also shows qualitative agreement with the experimental data taken by Mutchler besides displaying the relative greater impact effect due to high impact speed.

The surface disturbance can be described by indicating variations in water depth. The depth variation at four points, $\overset{*}{r}$ = 0.016, 0.148, 0.313, and 0.646 in. from the drop impact point respectively, are shown in Fig. 26. The depth varies rapidly near the drop impact point while remaining nearly unchanged at a distance of 0.5 in. The small depth variation at this radius suggests that depth measurements taken away from the drop impact point can serve as an indication of the average water depth in studying overland flow problems. The small pressure variation at 0.495 in. from the drop impact point along the water layer bottom is shown in Fig. 37 to further confirm the relative small pressure disturbance at this point. The first two points are inside the crater where depth decreases rapidly. Toward the end of the sequence shown in Fig. 26, a head between the crater center and the surrounding fluid is built which later forces the fluid to flow back into the crater center.

7.7 Splashing Test

The splashing of a mercury drop of 0.15 in. diameter falling 3 in. in the air against a smooth glass plate is described by the photographs taken in the early 19th century by Worthington (145). Analytical results

by using the following input data

$d = 0.15$ in.-Hg

$\rho = 26.2$ slug/ft^3

$\Gamma = 0.0352$ lb/ft

$\nu = 1.23 \times 10^{-6}$ ft^2/sec

$V_o = 4.0$ fps

show close agreement with Worthington's data as shown in Fig. 38. Analytical results obtained by Harlow and Shannon (67) by using MAC technique are also included for comparison. The deviation of the crown tip behavior is possibly due to the fact that surface tension and viscosity were neglected in their analysis. However, it should be pointed out that the time base for Worthington's data had been reduced by four before they were plotted on Fig. 38. The reason for doing this is because an examination of several drop impact pictures taken by Worthington revealed that a time interval between picture error of a factor of four is not unreasonable since this interval was of the order of milliseconds. Considering the fact that those pictures were taken at a time when photographic techniques were still in the early stages of development, a factor of four was introduced to adjust Worthington's data.

7.8 Energy Transformation

The transformation between potential, kinetic, and surface energies can be described if certain assumptions are made. The temperature is assumed to remain constant and all other energy forms are neglected including sound energy (43, 44). The dimensionless energy equation can be obtained by multiplying the equations of motion, Eqs. 6 and 7, by their

corresponding velocity components

$$V_r \left[\frac{\partial V_r}{\partial t} + \frac{1}{r}\frac{\partial r V_r^2}{\partial r} + \frac{\partial V_r V_z}{\partial z}\right] + V_r \frac{\partial \varphi}{\partial r} - \frac{V_r}{N_R}\frac{\partial \omega}{\partial z} = 0 \tag{66}$$

$$V_z \left[\frac{\partial V_z}{\partial t} + \frac{1}{r}\frac{\partial r V_r V_z}{\partial r} + \frac{\partial V_z^2}{\partial z}\right] + V_z \frac{\partial \varphi}{\partial z} + \frac{V_z}{N_R}\frac{1}{r}\frac{\partial r\omega}{\partial r} + \frac{V_z}{F} = 0 \tag{67}$$

where ω is the vorticity $= \frac{\partial V_r}{\partial z} - \frac{\partial V_z}{\partial r}$.

Upon adding Eqs. 66 and 67 and integrating over the fluid domain, it yields the dimensionless energy equation

$$0.5 \int \left(\frac{\partial V^2}{\partial t} + V_r \frac{\partial V^2}{\partial r} + V_z \frac{\partial V^2}{\partial z} + 2V^2 D\right) d\forall + \int \frac{V_z}{F}\, d\forall$$

$$+ \int \left(V_r \frac{\partial \varphi}{\partial r} + V_z \frac{\partial \varphi}{\partial z}\right) d\forall - \frac{1}{N_R}\int \left(V_r \frac{\partial \omega}{\partial z} - \frac{V_z}{r}\frac{\partial r\omega}{\partial r}\right) d\forall = 0 \tag{68}$$

where $V^2 = V_r^2 + V_z^2$ and $\forall$ is the dimensionless volume.

The first integral in Eq. 68 stands for the rate of change of kinetic energy, E_k, the second integral stands for the rate change of potential energy, E_p, the third integral represents the rate change of energy and the rate at which work is done involving the pressure, herein designated as the rate of change of the pressure energy, and the fourth integral represents the rate of change of energy due to the processes of interal friction and the rate at which the mechanical energy is dissipated. All energy forms are dimensionless.

The free water surface is assumed to be at its local equilibrium stage, the surface energy, E_s, at any particular instant is given by

$$E_s = \int_{\text{surface}} \frac{1}{W}\, dA \tag{69}$$

The total initial energy, E_i, is given by

$$E_i = \int (\frac{V^2}{2} + \varphi + \frac{z}{F})\, d\forall + \int \frac{1}{W}\, dA \tag{70}$$

The contribution to the total energy at subsequent time intervals can be determined by numerical integration of Eqs. 68 and 69. In the numerical integration, the energy components for each cell in r- and z-directions are located at the same node points as their corresponding velocity components. Their magnitudes are given by multiplying Eqs. 66 and 67 by the appropriate fluid volume in the cell. Mathematically the rate of change of mechanical energy components in the r- and z-directions are

$$\frac{dE_{r_{i,j}}}{dt} = V_{r_{i,j}} \cdot FCF_{r_{i,j}} \cdot (\frac{\partial V_r}{\partial t} + \frac{1}{r}\frac{\partial r V_r^2}{\partial r} + \frac{\partial V_r V_z}{\partial z} + \frac{\partial \varphi}{\partial r} - \frac{1}{N_R}\frac{\partial \omega}{\partial r})_{i,j} \tag{71}$$

$$\frac{dE_{z_{i,j}}}{dt} = V_{z_{i,j}} \cdot FCF_{z_{i,j}} \cdot (\frac{\partial V_z}{\partial t} + \frac{1}{r}\frac{\partial r V_r V_z}{\partial r} + \frac{\partial V_z^2}{\partial z} + \frac{\partial \varphi}{\partial z} + \frac{1}{N_R}\frac{\partial r\omega}{\partial r} + \frac{1}{F})_{i,j} \tag{72}$$

where

$$FCF_{r_{i,j}} = \begin{cases} \rho_{s_{i,j}} \cdot (i-0.5) & \text{if } V_{r_{i,j}} \leq 0 \\ \rho_{s_{i-1,j}} \cdot (i-1.5) & \text{if } V_{r_{i,j}} > 0 \end{cases}$$

$$FCF_{z_{i,j}} = \begin{cases} \rho_{s_{i,j}} \cdot (i-0.5) & \text{if } V_{z_{i,j}} \leq 0 \\ \rho_{s_{i-1,j}} \cdot (i-0.5) & \text{if } V_{z_{i,j}} > 0 \end{cases} \tag{73}$$

and they are located at the same node points as $V_{r_{i,j}}$ and $V_{z_{i,j}}$. The rate of change of energy at the center of each cell can thereafter be interpolated as

$$\frac{dE_{i,j}}{dt} = \left[\frac{\frac{dE_{r_{i,j}}}{dt} + \frac{dE_{r_{i+1,j}}}{dt}}{FCF_{r_{i,j}} + FCF_{r_{i+1,j}}} + \frac{\frac{dE_{z_{i,j}}}{dt} + \frac{dE_{z_{i,j+1}}}{dt}}{FCF_{z_{i,j}} + FCF_{z_{i,j+1}}} \right] \rho_{s_{i,j}} (i-0.5) \qquad (74)$$

which upon summation over the entire fluid domain gives the total rate change of mechanical energy.

For example, the time variation of energy forms after a 3.7 mm drop strikes a 0.33 in. deep water layer with a speed of 15.9 fps are presented in Fig. 39. The magnitude of the fourth integral in Eq. 68 is less than 0.1% of that of the third integral and is therefore not plotted. Figure 39 shows that at 15 msec after drop-liquid impact when the crater approaches its maximum size, the kinetic energy and surface energy decreases slowly while the potenetial energy increases slightly. The kinetic energy reaches a local minimum when the crater reaches its relative maximum size, however the kinetic energy at this point does not approach zero as postulated by Engel (42). In other words, the fluid does not cease its motion when the crater reaches its maximum size. Instead it circulates in a vertical plane and flows radially inward to form the Rayleight jet. The total energy is nearly preserved since the only mechanism for mechanical energy dissipation is viscous shear which has little effect in the duration shown in Fig. 39. It should be pointed out that the energy transformation considered in this section is the transformation between mechanical energies. Other energy transformations such as the heat transfer that might occur upon drop-liquid contact and the energy carried by the small droplets sepa-

rated from the fluid field are neglected. Also disregarded by virtue of the large cell size used in the computation is the surface energy introduced by the thin liquid film which might occur around the crown tip (146).

7.9 Surface Tension Effect

Surface tension force plays an important role in the drop impact process. In general, it stabilizes or damps free surface movement and was therefore included in all the analytical work in this study. A test run consisting of a 3.7 mm drop striking a 0.132 in. deep water layer with an impact speed of 28.41 fps was carried out, in which the surface tension force was excluded. The dimensionless impact pressure pulse at the bottom of the water layer under drop impact point is shown in Fig. 40 along with the results of the same test run including surface tension force. Figure 40 shows that when surface tension force is considered, the dimensionless pressure pulse has a high peak which occurs later in time than is the case if surface tension is excluded. Essentially, this is because the surface tension force tends to retard the radially outward fluid motion of the drop after it strikes. The same effect can be verified by examining the fluid movement. At the end of the sequences shown in Fig. 40, the axial velocity components near the surface and the bottom of the water layer under the drop impact point are 21.45 fps and 2.19 fps respectively when surface tension force is included. The corresponding velocities excluding surface tension are 21.65 fps and 2.23 fps. At an even later stage, $\overset{*}{t}$ = 10.6 msec, the radial velocity component at the crown tip is 4.72 fps when surface tension force is considered. Its corresponding velocity without surface tension force is 5.58 fps. Figure 40 also shows that 5.32% error will be

introduced in estimating the dimensionless peak pressure value should the surface tension force be neglected in the analysis in this case. This comparison justifies the inclusion of surface tension in the analysis and no further comparisons were made because limitation on computer time.

7.10 Effect Of Numerical Scheme On Accuracy Of Solution

The accuracy with which the numerical solution approaches the exact solution to the differential equations, Eqs. 5, 6, and 7, is a function of cell size, time increment, and size of computational field. In general, if stability is not a problem, the smaller the cell size and time increment and the larger the computational field the more accurate the solution will be. The question of how accurately the differential equations and boundary conditions describe the physical problem is another question. Because of limited available computer time and storage availability a relatively large cell size and a large computational time increment were used.

A. Computational Cell Size Effect: A smooth numerical result in general is obtained by using a fine cell size instead of a large cell size. For the mercury splashing test, two cell sizes were used to illustrate the effect of cell size. In Fig. 41, pointwise numerical solutions are presented in the form of a set of short straight lines. Numerical results by using L = 0.0149 in. are plotted with short straight lines through which smooth curves are drawn, while results by using L = 0.00747 in. are plotted with dotted lines. The cell size differs by a factor of two but the difference in estimating the drop top and

tip behavior is less than 4%. For the water drop computations a cell size of approximately 0.025 in. was used which required three to ten minutes to run each individual drop-liquid impact test using an IBM 360/50 digital computer. The time increment was chosen to satisfy the criteria given by Eqs. 53, 54, and 55 to assure numerical stability.

B. Computational Field Size Effect: This study was intended to investigate the drop-liquid impact phenomenon in an infinite wide fluid field. A finite amount of computer storage, however, required that a boundary be placed on the field. A circumferential solid wall was therefore installed around the drop impact point, and the computational field size was chosen to minimize this side wall effect. This wall was not present in the experimental studies. In Fig. 42, the impact pressure pulses for three different computational field sizes with radii, R = 0.23, 0.561, and 1.15 in., are presented. The pressure pulses with R = 0.561 and 1.15 in. show no significant difference indicating that the side wall effect beyond R = 0.561 in. is negligible, while the pressure pulse with R = 0.23 in. has a relative larger magnitude displaying a strong side wall effect. Therefore, a computational field with a radius of approximately 0.5 in. is justified for computations concerning the pressure field.

C. Free Slip versus No Slip Condition: Physically the fluid can not slip on a solid wall. However, if the boundary layer thickness is less than the cell size, a free slip boundary condition in the numerical computation may produce a more accurate result. In this study, the fluid velocity near the solid wall generated by the impinging drop is very small, therefore the numerical results using both conditions showed essentially no difference up to the time when maximum impact pressure occurred.

7.11 Error Analysis On Experimental Data

The possible sources of experimental error and an estimate of their magnitude are given below.

A. Surface Tension Variation: For a test period of four months, the room and water temperature varied between 65°F and 74°F. The corresponding variation in surface tension force per unit length with respect to the average temperature of 70°F is about ±0.5%.

B. Drop Size Variation: Between twenty to three-hundred drops produced at various flow rate were collected and weighed to 0.001 gm. This corresponds to an average weighing error of less than 0.1%. The average drop weight was then used to calculate the equivalent drop diameter. The drop size thus obtained varies mainly as a function of tube geometry and tip geometry. Its variation can be regarded as an aggregate error with respect to its average value.

Tube OD (in.)	Tube ID (in.)	d (mm)	Variation (mm)	% Variation (%)
0.024	0.011	2.70	+0.03	+1.11
			-0.08	-2.97
0.038	0.023	3.12	+0.14	+4.48
			-0.20	-6.41
0.038	0.023	3.12	+0.01	+0.32
			-0.03	-0.96
0.062	0.045	3.70	+0.04	+1.08
			-0.10	-2.70

C. Depth Measurement Error: The depth of the water layer was measured to ± 0.001 in. using a micrometer point gage. This results in a ± 0.16% to ± 2.0% error in measuring the water depth which varied from 0.6 to 0.05 in.

D. Surface Sensivity of Pressure Transducer: The surface sensitivity of the pressure transducer used in this study was assumed to have the

response curve described in Fig. 10. Two other reasonable alternatives of the response curve are: first, a one-to-one response from transducer center to a radius of 0.132 in. and then a linear decrease to zero response at a radius of 0.180 in; second, a uniform sensitivity inside a circle of radius 0.132 in. The discrepancy between these two possible pressure response curves and the one used in the present study amounts to +6.7 to -7.7%.

E. Pressure Pulse Error: To trace the impact pressure pulse from the oscilloscope involved a reading error of $\pm$ 0.015 in. which represents a 0.8 to 2.0% error in recording various pressure pulses. The chance of using impact pressure pulse not striking directly upon the center of the transducer was small because of the procedure in recording the impact pressure pulse as described in section 6.1.1, however, quantitative error estimation is unavailable. The data scatter about the curves in Figs. 28-31 could be viewed qualitatively as a rough total error estimation. Such a typical error amounts to $\pm$ 3.6%.

The rise time of the transducer was about 3 microseconds which was sufficient for measuring the pressure rise accurately, yet the recorded time to reach the maximum impact pressure, t_p, was rather random as shown in Fig. 27 and varied more than 100%. Figure 27 also shows that the results scatter more widely for drops falling a short distance. This suggests that the randomness of the results could be due to the difference in drop geometry upon drop impact, since the drop oscillates and changes its shape while falling in the air and reaches a stable drop shape only after falling a sufficient distance. Magnatic tape was considered as a recording aid at one time and was not used due to the fact that the time span between each

7.11 Error Analysis On Experimental Data

The possible sources of experimental error and an estimate of their magnitude are given below.

A. Surface Tension Variation: For a test period of four months, the room and water temperature varied between $65^{o}F$ and $74^{o}F$. The corresponding variation in surface tension force per unit length with respect to the average temperature of $70^{o}F$ is about $\pm 0.5\%$.

B. Drop Size Variation: Between twenty to three-hundred drops produced at various flow rate were collected and weighed to 0.001 gm. This corresponds to an average weighing error of less than 0.1%. The average drop weight was then used to calculate the equivalent drop diameter. The drop size thus obtained varies mainly as a function of tube geometry and tip geometry. Its variation can be regarded as an aggregate error with respect to its average value.

Tube OD (in.)	Tube ID (in.)	d (mm)	Variation (mm)	% Variation (%)
0.024	0.011	2.70	+0.03	+1.11
			-0.08	-2.97
0.038	0.023	3.12	+0.14	+4.48
			-0.20	-6.41
0.038	0.023	3.12	+0.01	+0.32
			-0.03	-0.96
0.062	0.045	3.70	+0.04	+1.08
			-0.10	-2.70

C. Depth Measurement Error: The depth of the water layer was measured to $\pm$ 0.001 in. using a micrometer point gage. This results in a $\pm$ 0.16% to $\pm$ 2.0% error in measuring the water depth which varied from 0.6 to 0.05 in.

D. Surface Sensivity of Pressure Transducer: The surface sensitivity of the pressure transducer used in this study was assumed to have the

response curve described in Fig. 10. Two other reasonable alternatives of the response curve are: first, a one-to-one response from transducer center to a radius of 0.132 in. and then a linear decrease to zero response at a radius of 0.180 in; second, a uniform sensitivity inside a circle of radius 0.132 in. The discrepancy between these two possible pressure response curves and the one used in the present study amounts to +6.7 to -7.7%.

E. Pressure Pulse Error: To trace the impact pressure pulse from the oscilloscope involved a reading error of $\pm$ 0.015 in. which represents a 0.8 to 2.0% error in recording various pressure pulses. The chance of using impact pressure pulse not striking directly upon the center of the transducer was small because of the procedure in recording the impact pressure pulse as described in section 6.1.1, however, quantitative error estimation is unavailable. The data scatter about the curves in Figs. 28-31 could be viewed qualitatively as a rough total error estimation. Such a typical error amounts to $\pm$ 3.6%.

The rise time of the transducer was about 3 microseconds which was sufficient for measuring the pressure rise accurately, yet the recorded time to reach the maximum impact pressure, t_p, was rather random as shown in Fig. 27 and varied more than 100%. Figure 27 also shows that the results scatter more widely for drops falling a short distance. This suggests that the randomness of the results could be due to the difference in drop geometry upon drop impact, since the drop oscillates and changes its shape while falling in the air and reaches a stable drop shape only after falling a sufficient distance. Magnatic tape was considered as a recording aid at one time and was not used due to the fact that the time span between each

individual pressure pulse was much longer than that of the pressure pulse itself. In addition, only a small percentage of the total drop impact measurements were used because only those tests in which the drop struck the center of the transducer were used.

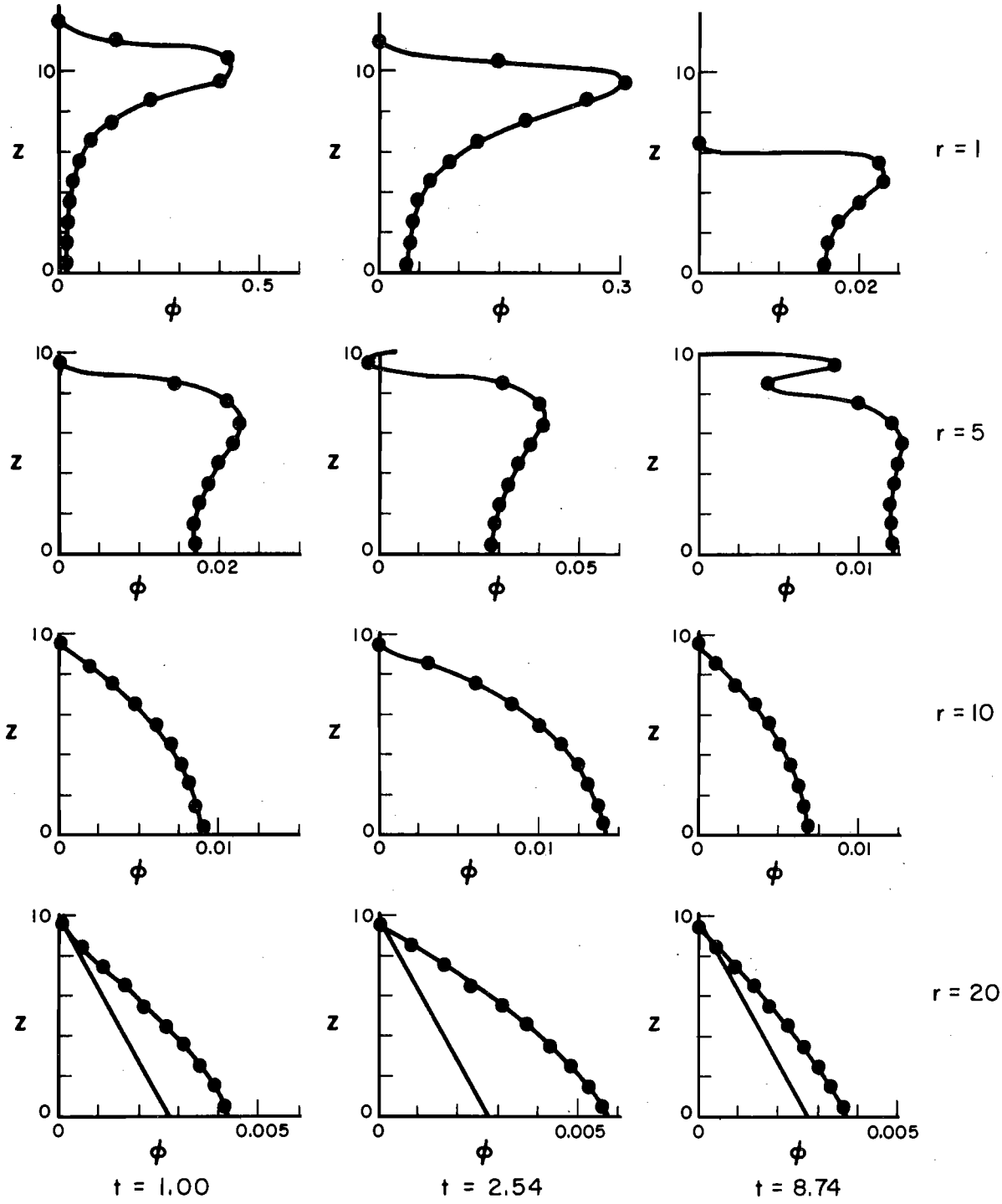

FIGURE 35 VERTICAL PRESSURE DISTRIBUTION

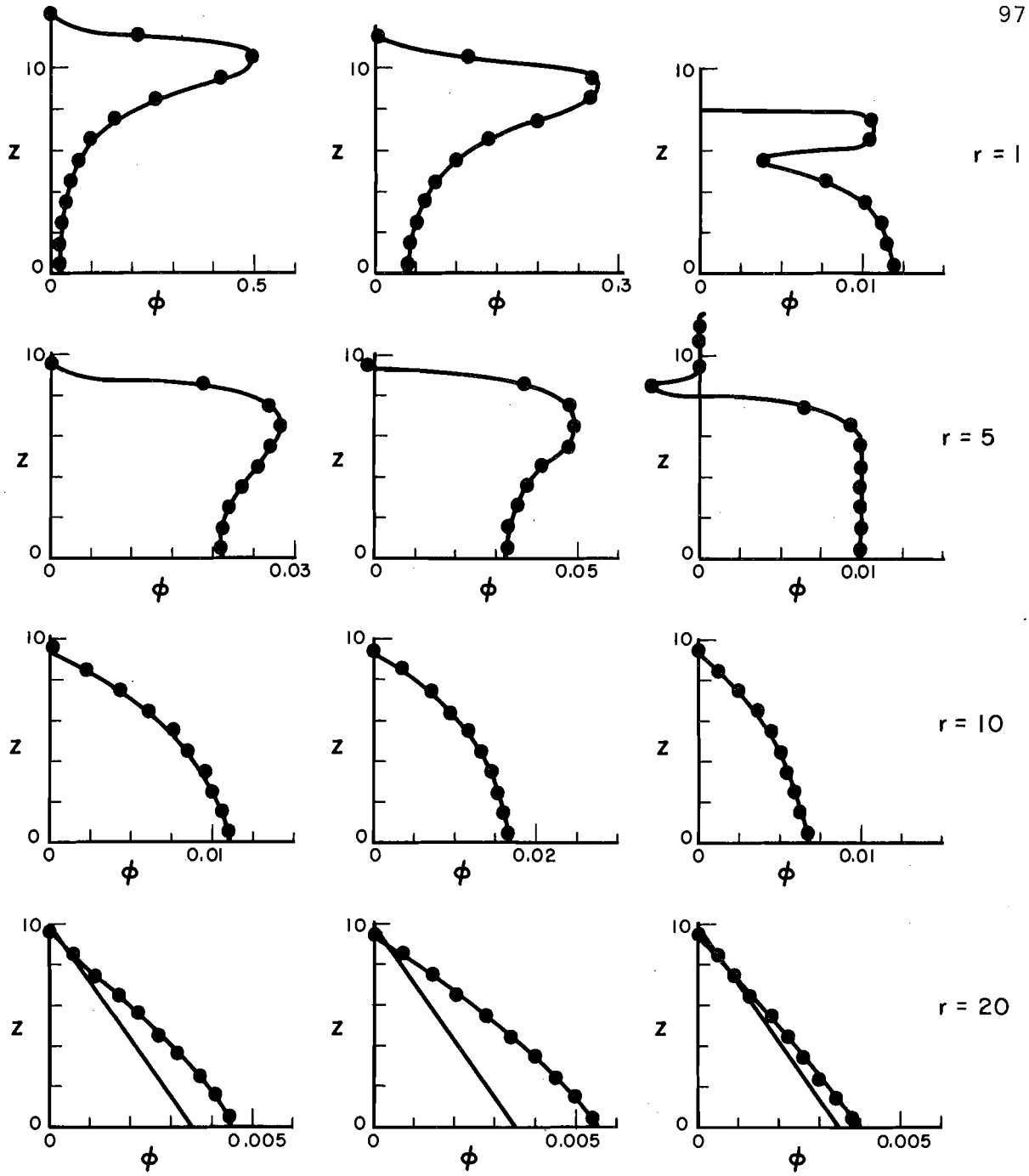

FIGURE 36 VERTICAL PRESSURE DISTRIBUTION

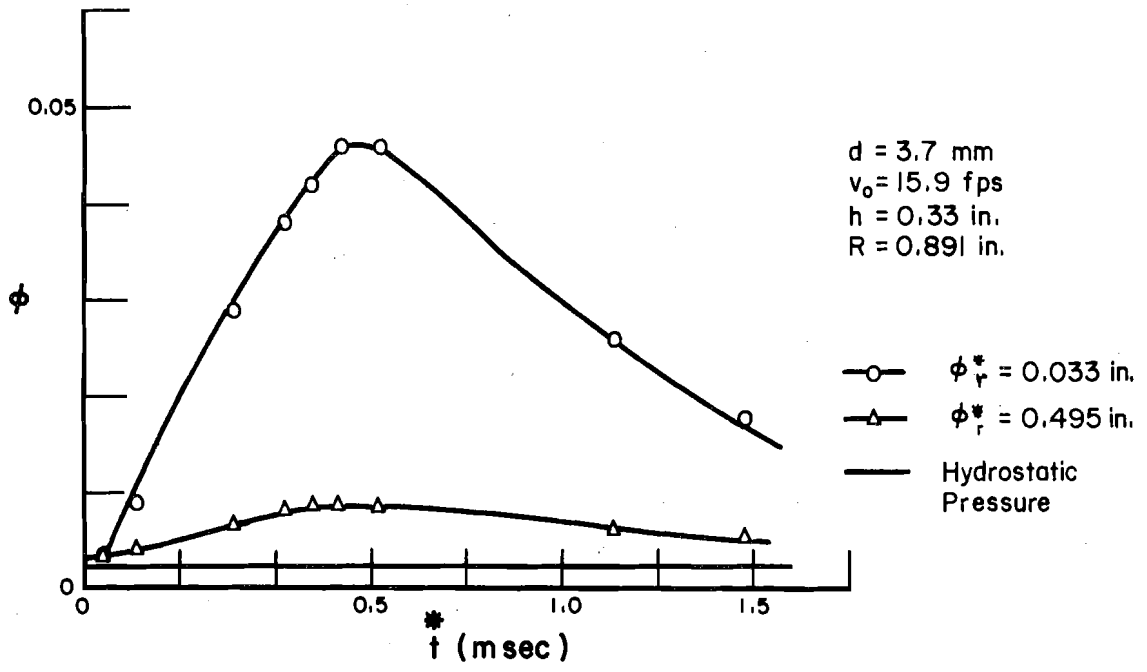

FIGURE 37 PRESSURE VARIATION

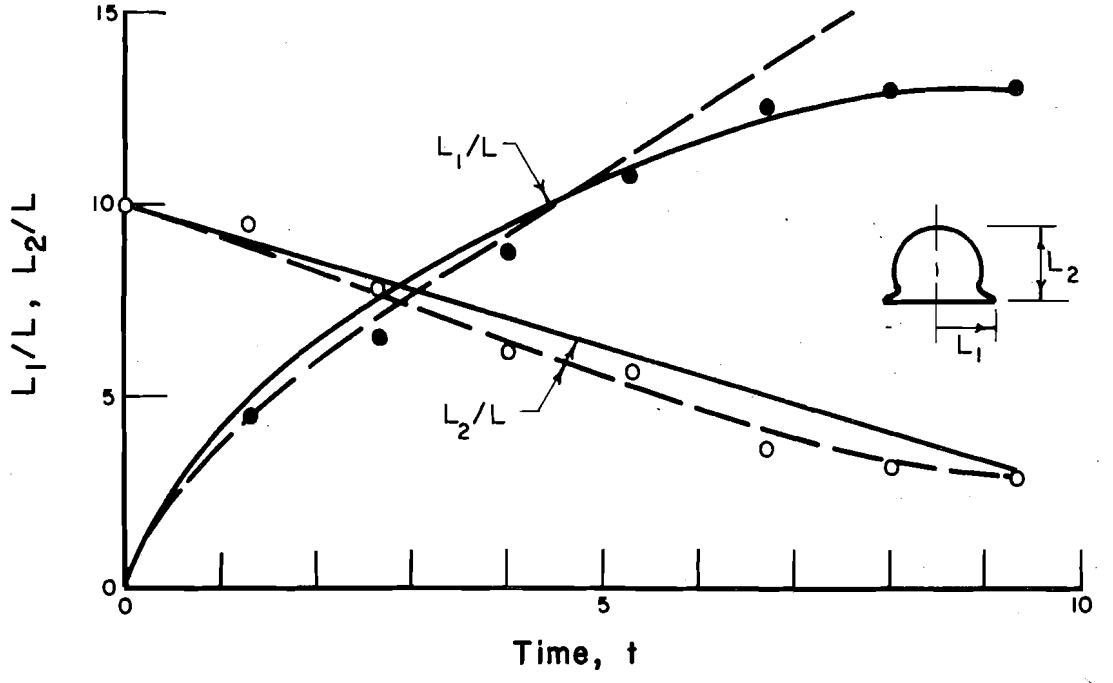

FIGURE 38 MERCURY DROP SPLASHING TEST

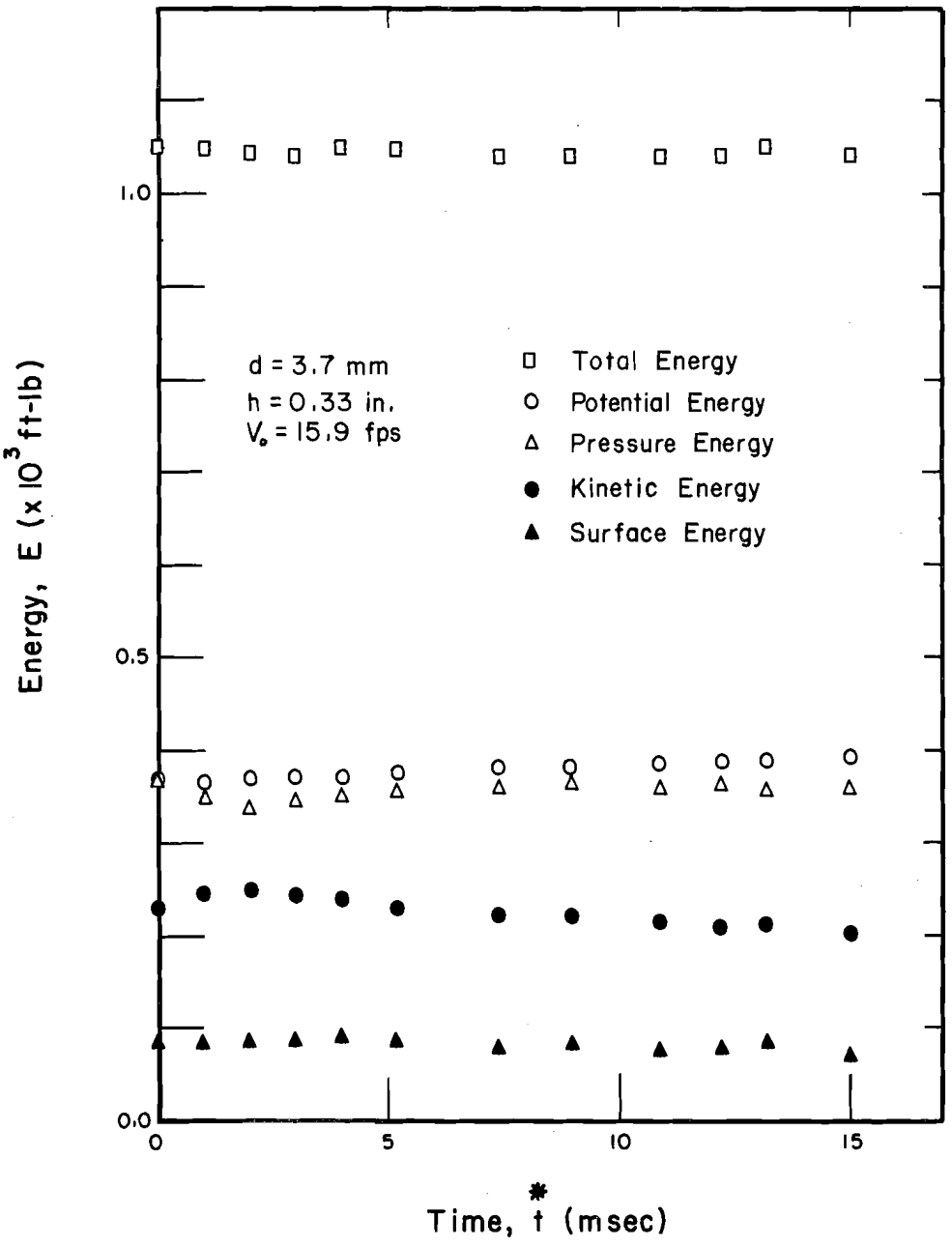

FIGURE 39 ENERGY TRANSFORMATION

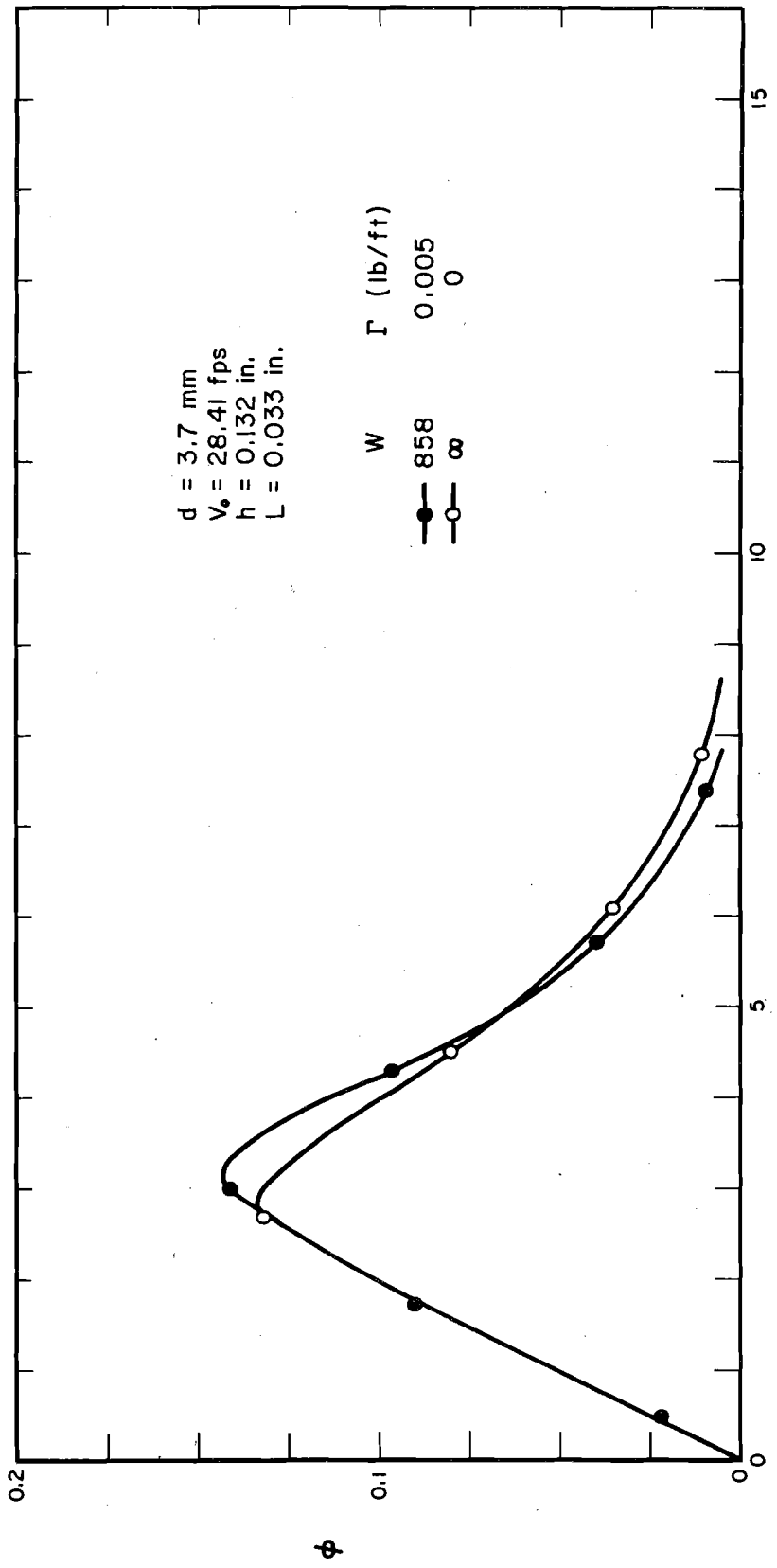

FIGURE 40 SURFACE TENSION EFFECT

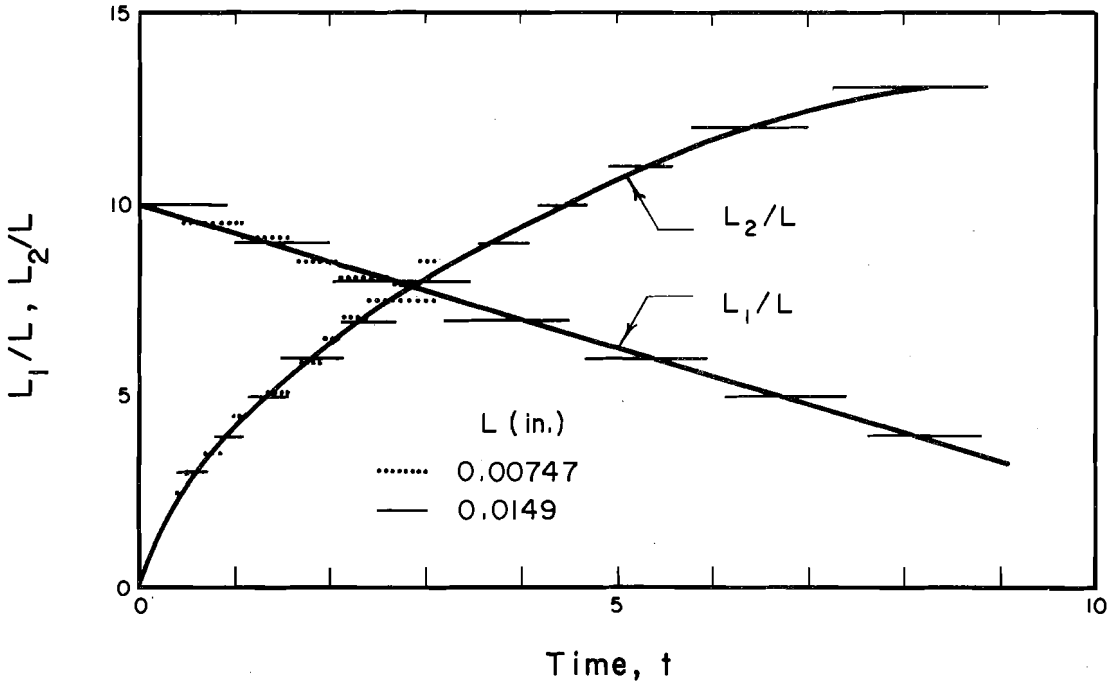

FIGURE 41 COMPUTATIONAL CELL SIZE EFFECT

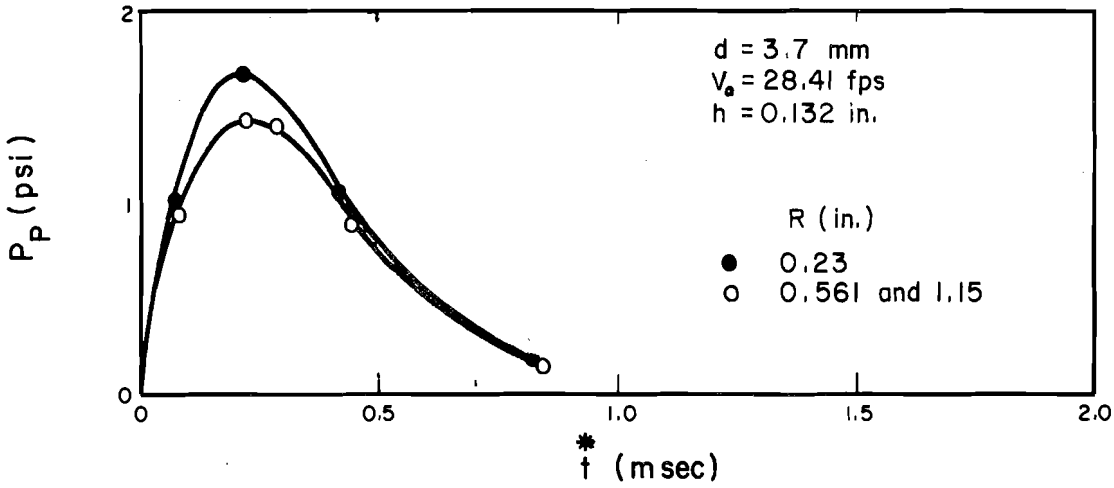

FIGURE 42 COMPUTATIONAL FIELD SIZE EFFECT

LIST OF REFERENCES

1. Abbas, M. A., and J. Latham, The Instability of Evaporating Charged Drops, J. Fluid Mech., 30, 663, 1967.

2. Adam, N. K., The Physics and Chemistry of Surfaces, Oxford Press, London, 1949.

3. Alder, B., S. Fernbach, and M. Rotenberg, Methods in Computational Physics — Volume 3: Fundamental Methods in Hydrodynamics, Academic Press, N. Y., N. Y., 1964.

4. Amsden, A. A., The Particle-In-Cell Method for the Calculation of the Dynamics of Compressible Fluids, Los Alamos Sci. Lab., Los Alamos, New Mexico, LA-3466, 1966.

5. Amsden, A. A., and F. H. Harlow, Transport of Turbulence in Numerical Fluid Dynamics, J. Computational Physics, 3, 94, 1968.

6. Bashforth, F., An Attempt to Test the Theories of Capillary Action by Comparing the Theoretical and Measured Forms of Drops of Fluid, Cambridge Univ. Press, 1883.

7. Baumeister, K. J., and T. D. Hamill, Liquid Drops: Numerical and Asymptotic Solutions of Their Shapes, NASA TN D-4779, Lewis Res. Center, Cleveland, Ohio, 1968.

8. Best, A. C., Emperical Formula for the Terminal Velocity of Waterdrops Falling Through the Atmosphere, Quarterly J. Royal Math. Soc., 76, 302, 1950b.

9. Birkhoff, C., D. P. MacDougall, E. M. Pugh, and G. Taylor, Explosives With Lined Cavities, J. Appl. Physics, 19, 563, 1948.

10. Blauchard, D. C., Behavior of Water Drops at Terminal Velocity, Trans. Am. Geophy. Uni., 31, 836, 1950.

11. Bom, N., Effect of Rain on Underwater Noise Level, J. Accoust. Soc. Am., 45, 150, 1969.

12. Bond, W. N., Bubbles and Drops and Stokes Law, Phil. Mag., Ser. 7, 4, 889, 1927.

13. Boussinesq, J., Vitesse de la chute lente, devenue uniform, d'une goutte liquid sphérique, dans un fluide visqueux de poids specifique moindre, Ann. Chim. Phys., 29, 364, 1913.

14. Bowden, F. P., and J. H. Brunton, The Deformation of Solids by Liquid Impact at Supersonic Speeds, Proc. Roy. Soc. A-263, 433, 1961.

15. Bowden, F. P., and J. E. Field, The Brittle Fracture of Solids by Liquid Impact, by Solid Impact and by Shock, Proc. Roy. Soc. A-282, 331, 1964.

16. Bowden, F. P., A Discussion on Deformation of Solids by the Impact of Liquids and Its Relation to Rain Damage in Aircraft and Missiles, to Blade Erosion in Steam Turbines, and to Cavitation Erosion, Phil. Trans. Roy. Soc. of London, A-260, 73, 1966.

17. Brazee, R. D., Theoretical Aspects of Droplet Impact Measurements, ARS42-77, U.S. Dept. Agr., 1963.

18. Brodkey, R. S., The Phenomena of Fluid Motions, Addison-Wesley Publishing Company, Reading, Mass., 1967.

19. Centry, R. A., R. E. Martin, and B. J. Daly, An Eulerian Differencing Method for Unsteady Compressible Flow Problems, J. Compu. Physics, 1, 87, 1966.

20. Chapman, D. S., and P. R. Critchlow, Formation of Vortex Rings from Falling Drops, J. Fluid Mech., 29, 177, 1967.

21. Chapman, G., Size of Raindrops and Their Striking Force at the Soil Surface in a Red Pine Plantation, Trans. AGU, 29, 664, 1948.

22. Charters, A. C., High Speed Impact, Sci. Am., 128, Oct., 1960.

23. Chen, C. L., An Analysis of Overland Flow, Ph.D. thesis, Dept. of Agr. Eng., Michigan State Uni., 1962.

24. Chen, C. L., and V. T. Chow, Hydrodynamics of Mathematically Simulated Surface Runoff, Dept. of Civil Eng., Uni. of Illinois, 1968.

25. Chow, V. T., Open-Channel Hydraulics, McGraw-Hill Book Company, Inc., N. Y. 1959.

26. Chow, V. T., and T. E. Harbaugh, Raindrop Production for Laboratory Watershed Experimentation, J. Geoph. Res., 70, 6111, 1965.

27. Cook, M. A., R. T. Keyes, and W. O. Ursenbach, Measurement of Detonation Pressure, J. Appl. Phys., 33, 3413, 1962.

28. Cook, M. A., and K. S. Mortensen, Impact Cratering in Granular Materials, J. Appl. Phys., 38, 5125, 1967.

29. Courant, R., and K. D. Friedrichs, Supersonic Flow and Shook Waves, Interscience Publishing Company, N. Y., 1948.

30. Daly, B. J., Numerical Study of Two Fluid Rayleigh-Taylor Instability, Phys. Fluids, 10, 297, 1967.

31. Daly, B. J., and W. E. Pracht, Numerical Study of Density-Current Surges, Phys. Fluids, 11, 15, 1968.

32. Daly, B. J., A Technique for Including Surface Tension Effects in Hydrodynamic Calculations, J. Compu. Phys., 4, 97, 1969.

33. Daly, B. J., Numerical Study of the Effect of Surface Tension on Interface Instability, Phys. Fluids, 12, 1340, 1969.

34. Edgerton, H. E., E. A. Hauser, and W. B. Tucker, Studies in Drop Formation as revealed by the High-Speed Motion Camera, J. Phys. Chem., 41, 1017, 1937.

35. Edgerton, H. E., and J. R. Killian, Flash! Seeing the Unseen by Ultra High-Speed Photograph, Hale, Cushman and Flint, Boston, 1939, Charles, T. Branford Company, Boston, 1954.

36. Ekeru, P. C., Raindrop Impact as the Force Initiating Soil Erosion, Soil Sci. Soc. Am., Proc. 15, 7, 1950.

37. Ellison, W. D., Splash Erosion in Pictures, J. Soil and Water Cons., 5, 71, 1950.

38. Emery, A. F., An Evaluation of Several Differencing Methods for Inviscid Fluid Flow Problems, J. Compu. Phys., 2, 306, 1968.

39. Engel, O. G., Waterdrop Collisions with Solid Surfaces, J. Res., National Bur. Stand., 54, 281, 1955.

40. Engel, O. G., Collision of Liquid Drops with Liquids, National Bur. Stand., TN 89, 1961.

41. Engel, O. G., Collisions of Liquid Drops with Liquids, Part II, Crater Depth in Fluid Impacts, Tech. Rep. WADD-TR-60-475, Aeronaut. System Div., Wright-Patterson AFB, Ohio, 1962.

42. Engel, O. G., Crater Depth in Fluid Impacts, J. Appl. Phys., 37, 1798, 1966.

43. Engel, O. G., Initial Pressure, Initial Flow Velocity, and the Time Dependence of Crater Depth in Fluid Impacts, J. Appl. Phys., 38, 3935, 1967.

44. Franz, G. J., Splashes as Sources of Sound in Liquids, J. Accoust. Soc. Am., 31, 1080, 1959.

45. Fromm, J. E., A Method of Computing Nonsteady, Incompressible, Viscous Fluid Flows, Los Alamos Sci. Lab., Los Alamos, New Mexico, LA-2910, 1963.

46. Fromm, J. E. and F. H. Harlow, Numerical Solution of the Problem of Vortex Street Development, Phys. Fluids, 6, 975, 1963.

47. Garabedian, P. R., Free Boundary Flows of A Viscous Liquid, Comm. on Pure and Appl. Mathe., 14, 421, 1966.

48. Gerlach, C. R., Investigation of Water Impact of Blunt Rigid Bodies-Real Fluid Effects, Tech. Rept. No. 1, Southwest Res. Inst., San Antonio, Houston, 1967.

49. Gilchrist, R. B., and W. A. Strawderman, Experimental Hydrophone-Size Correction Factor for Boundary-Layer Pressure Fluctuations, J. Accoust. Soc. Am., 38, 298, 1965.

50. Glass, L. J., and E. T. Smerdon, Effect of Rainfall on the Velocity Profile in Shallow-Channel Flow, ASAE, 10, 330, 1967.

51. Goad, W. B., WAT: A Numerical Method for Two-dimensional Unsteady Fluid Flow, Los Alamos Sci. Lab., Los Alamos, New Mexico, LAMS-2365, 1960.

52. Grace, R. A., and P. S. Eagleson, Similarity Criteria in the Surface Runoff Process, Dept. of Civil Eng., MIT, Hydrodynamic Lab. Rept. No. 77, 1965.

53. Grace, R. A., and P. S. Eagleson, The Modeling of Overland Flow, Water Resources Res., 2, 393, 1966.

54. Gunn, R., and G. D. Kinzer, The Terminal Velocity of Fall for Water Droplets in Stagnant Air, J. Meteor., 6, 243, 1949.

55. Guthrie, F., On Drops, Proc. Roy. Soc. (London), 13, 444, 1864.

56. Haberman, W. L., and R. K. Morton, An Experimental Investigation of the Drag and Shape of Air Bubbles Rising in Various Liquids, Navy Dept. Rept. 802, David Taylor Model Basin, Washington, D.C., 1953.

57. Halperson, S. M., Comparisons Between Hydrodynamic Theory and Impact Experiments, Proc. 7th Hypervelocity Impact Symposium at Tampa, Florida, Nov., 1964.

58. Handbook of Chemistry and Physics, Chemical Rubber Publishing Co., 48th ed., 1967-1968.

59. Harkins, W. D., and F. E. Brown, The Determination of Surface Tension, and the Weight of Falling Drops: The Surface Tension of Water and Benzene by the Capillary Height Methods, J. Am. Chem. Soc., 41, 499, 1919.

60. Harlow, F. H., The Particle-In-Cell Method for Hydrodynamic Calculations, Los Alamos Scie. Lab., Los Alamos, New Mexico, LA-2139, 1957.

61. Harlow, F. H., Stability of Difference Equations, Selected Topics, Los Alamos Sci. Lab., Los Alamos, New Mexico, LAMS-2452, 1960.

62. Harlow, F. H., and B. D. Meixner, The Particle-And-Force Computing Method for Fluid Dynamics, Los Alamos Sci. Lab., Los Alamos, New Mexico, LAMS-2567, 1961.

63. Harlow, F. H., The Particle-In-Cell Method for Numerical Solution of Problems in Fluid Dynamics, Proc. of Symposia in Appl. Math., 15, 269, 1965.

64. Harlow, F. H., J. P. Shannon, and J. E. Welch, Liquid Wave of Computer, Science, 149, 1092, 1965.

65. Harlow, F. H., and J. E. Welch, Numerical Calculation of Time-Dependent Viscous, Incompressible Flow of Fluid with Free Surface, Phys. Fluids, 8, 2182, 1965.

66. Harlow, F. H., and J. E. Welch, Numerical Study of Large Amplitude Free Surface Motions, Phys. Fluids, 9, 842, 1966.

67. Harlow, F. H., and J. P. Shannon, Distortion of a Splashing Liquid Drop, Science, 157, 547, 1967.

68. Harlow, F. H., and J. P. Shannon, The Splash of a Liquid Drop, J. Appl. Phys., 38, 3855, 1967.

69. Harlow, F. H., and A. A. Amsden, Numerical Calculation of Almost Incompressible Flow, J. Compu. Phys., 3, 80, 1968.

70. Harpor, J. F., D. W. Moore, and J. R. A. Pearson, The Effect of the Variation of Surface Tension with Temperature on the Motion of Bubbles and Drops, J. Fluid Mech., 27, 361, 1967.

71. Hauser, E. A., H. E. Edgerton, B. M. Holt, and J. J. Cox, Jr., The Application of the High-Speed Motion Picture Camera to Research on the Surface Tension of Liquids, J. Phys. Chem., 40, 973, 1936.

72. Hill, T. L., Concerning the Dependence of the Surface Energy and Surface Tension of Spherical Drops and Bubbles on Radius, J. Am. Chem. Soc., 72, 3923, 1950.

73. Hirt, C. W., and F. H. Harlow, A General Corrective Procedure for the Numerical Solution of Initial-Value Problems, J. Compu. Phys., 2, 114, 1967.

74. Hirt, C. W., Heuristic Stability Theory for Finite Difference Equations, J. Compu. Phys., 2, 339, 1968.

75. Hirt, C. W., and J. P. Shannon, Free-Surface Stress Conditions for Incompressible-Flow Calculations, J. Compu. Phys., 2, 403, 1968.

76. Hobbs, P. V., and A. J. Kezweeny, Splashing of a Water Drop, Science, 155, 1112, 1967.

77. Hobbs, P. V., and T. Osheroff, Splashing of Drops on Shallow Liquids, Science, 158, 1184, 1967.

78. Hoerner, S. F., Fluid-Dynamic Drag, Dr.-Ing. S. F. Hoerner, 148 Busteed Drive, Midland Park, N. J.

79. Hughes, R. R., The Mechanics of Drops, Chemical Engr. Progress, 48, 497, 1952.

80. Izzard, C. F., and M. T. Agustine, Preliminary Report on Analysis of Runoff, From Simulated Rainfall on a Paved Plot, Trans. AGU, 24, 500, 1943.

81. Izzard, C. F., The Surface Profile of Overland Flow, Trans. AGU, 25, 959, 1944.

82. Izzard, C. F., Hydraulics of Runoff From Developed Surfaces, Hwy. Res. Bd., Proc., 26, 129, 1947.

83. Jenkins, D. C., J. D. Booker, and J. W. Sweed, An Experimental Method for the Study of the Impact Between a Liquid Drop and a Surface Moving at High Speed, R & M No. 3203, 1961.

84. Jenkins, D. C., An Experimental Method for Studying the High Speed Impact of a Liquid Drop on a Liquid Surface, Roy. Aircraft Establishment TR 66135, 1966.

85. Johnson, R. S., The Effect of Air Compressibility in the Impact of a Flat Body Upon a Free Surface, Uni. of Calif. (Berkeley), College of Engr., Report No. NA-66-8, 1966.

86. Johnstone, H. F., and G. C. Williams, Absorption of Gases by Liquid Drops, Indus. Engr. Chem., 31, 993, 1939.

87. Kelkar, W. N., Size Distribution of Raindrops, Part IV, Dept. of Phys., Nowrosjee Wadia College, Ponna, 1962.

88. Kennard, E. H., Irrotational Flow of Frictionless Fluids, Mostly of Invariable Density, Rept. 2299, David Taylor Model Basin, Washington D.C., 1967.

89. Keulegan, G. K., Spatially Variable Discharge Over A Sloping Plane, Trans. AGU, 25, 956, 1944.

90. Lambs, H., Hydrodynamics, 6th ed., Dover Publications, N. Y., 1932.

91. Landau, L. D., and E. M. Lifshitz, Fluid Mechanics, Pergamon Press, London, 1959.

92. Laws, J. O., Recent Studies in Raindrops and Erosion, Agr. Eng., 21, 431, 1940.

93. Laws, J. O., Measurements of the Fall Velocity of Water-Drops and Raindrops, Trans. AGU, 22, 709, 1941.

94. Laws, J. O., and D. A. Parsons, The Relation of Raindrop-Size to Intensity, Trans. AGU, 24, 452, 1943.

95. Levich, V. G., Physicochemical Hydrodynamics, Prentice Hall, Englewood Cliffs, N. J., 1962.

96. Lighthill, M. J., Waves in Fluids, Comm. on Pure and Appl. Math., 20, 267, 1967.

97. Los Angeles District Corps of Engineer, Data Report, Airfield Drainage Investigation, Oct. 1955.

98. Macklin, W. C., and P. V. Hobbs, Subsurface Phenomena and the Splashing of Drops on Shallow Liquids, Science, 166, 107, 1969.

99. Manfré, G., Rheological Aspects of Drop Formation, J. Appl. Phys., 37, 1955, 1966.

100. Manfré, G., and R. W. Whorlow, The Rapid Formation of Drops of Viscous Liquids, Brit. J. Appl. Phys., 18, 839, 1967.

101. May, A., Drag Coefficients of Steel Spheres Entering Water Vertically, J. Appl. Phys., 19, 1109, 1948.

102. May, A., The Influence of the Proximity of Tank Walls on the Water-Entry Behavior of Models, NAVORD Rept. 2240, Naval Ordnance Lab., White Oak, Maryland, 1951.

103. McDonald, J. E., The Shape and Aerodynamics of Large Raindrops, J. Meteo., 11, 478, 1954.

104. McDonald, J. E., The Shape of Raindrops, Sci. Am., 190, 64, 1954.

105. Meyer, L. D., Simulation of Rainfall for Soil Erosion Research, Trans. ASAE, 8, 63, 1965.

106. Miller, C. A., and L. E. Scriven, The Oscillations of a Fluid Droplet Immersed in Another Fluid, J. Fluid Mech., 32, 417, 1968.

107. Mutchler, C. K., and L. F. Hermsmeier, A Review of Rainfall Simulators, Paper No. 63-726, Winter Meeting of ASAE at Chicago, Illinois, 1963.

108. Mutchler, C. K., Waterdrop Formation from Capillary Tubes, ARS41-107, U.S. Dept. Agr., Washington, D.C., 1965.

109. Mutchler, C. K., Using the Drift of Waterdrops During Fall for Rainfall Simulator Design, J. Geophys. Res., 70, 3899, 1965.

110. Mutchler, C. K., and W. C. Moldenhauer, Applicator for Laboratory Rainfall Simulator, Trans. ASAE, 6, 220, 1963.

111. Mutchler, C. K., Parameters for Describing Raindrop Splash, J. Soil and Water Conservation, 22, 91, 1967.

112. Noh, W. F., A General Theory for the Numerical Solution of the Equations of Hydrodynamics — Numerical Solutions of Nonlinear Differential Equation, ed. by D. Greenspan,John Wiley & Sons, Inc., N. Y., 1966.

113. Palmer, R. S., An Apparatus for Forming Waterdrop, U.S. Dept. Agr., ARS Production Res. Rept. 63, 1962.

114. Palmer, R. S., Waterdrop Impact Forces, Paper No. 63-727, presented at the Winter Meeting of ASAE, Chicago, Illinois, 1963.

115. Payne, L. E., On the Stability of Solutions of the Navier-Stokes Equation and Convergence to Steady State, SIAM J. Appl. Math., 15, 392, 1967.

116. Pearson, J. E., and G. E. Martin, An Evaluation of Raindrop Sizing and Counting Techniques, Sci. Rept. No.1, Ill. State Water Survey, 1957.

117. Pfeifer, R. J., and C. D. Hendricks, Charge-to-Mass Relationships for Electrohydrodynamical Sprayed Liquid Droplets, Phys. Fluids, 10, 2149, 1967.

118. Reinsch, C. H., Smoothing by Spline Functions, Numerische Matehmatik, 10, 177, 1967.

119. Reynolds, O., On the Action of Rain to Calm the Sea, Proc. Lit. and Phil. Soc. Manchester, 14, 1874-1875.

120. Rich, M., and S. M. Blackman, A Method for Eulerian Fluid Dynamics, Los Alamos Sci. Lab., Los Alamos, New Mexico, LAMS-2826, 1963.

121. Richardson, E. G., The Impact of a Solid on a Liquid Surface, Proc., Phys. Soc. (London), 61, 352, 1948.

122. Richtmyer, R. D., A Survey of Difference Methods for Nonsteady Fluid Dynamics, NCAR TN 63-2, Boulder, Colo., 1962.

123. Richtmyer, R. D., and K. W. Morton, Difference Methods for Initial-Value Problems, Interscience Publishers, N. Y., 1967.

124. Schlichting, H., Boundary Layer Theory, 4th ed., McGraw-Hill Book Company, N. Y., 1960.

125. Schultz, M. H., and R. S. Varga, L-Splines, Numerische Mathematik, 10, 345, 1967.

126. Smerdon, E. T., Effect of Rainfall on Critical Tractive Forces in Channels with Shallow Flow, Trans. ASAE, 7, 287, 1964.

127. Spilhaus, A. F., Raindrop Size, Shape, and Falling Speed, J. Meteo., 5, 108, 1948.

128. Stoker, J. J., Water Waves, Interscience Publishers, Inc., N. Y., 1957.

129. Streeter, V. L., and E. B. Wylie, Hydraulic Transients, McGraw-Hill Book Company, N. Y., 1967.

130. Taylor, T. D., and A. Acrivos, On the Deformation and Drag of a Falling Viscous Drop at Low Reynolds Number, J. Fluid Mech., 18, 466, 1964.

131. Thelen, J., W. Trommsdorff, and H. Wiegand, Experiments about the Generation of Uniform Sized Liquid Droplets, Deutsche Versuchsanstalt fur Luft-und Raumfahrt, Porz (W. Germany), 1967.

132. Thom, A., and C. J. Apelt, Field Computations in Engineering and Physics, D. Van Nostrand Company, Ltd., London, 1961.

133. Walsh, J. L., J. H. Ahlberg, and E. N. Nilson, Best Approximation Properties of the Spline Fit, J. Math. Mech., 11, 225, 1962.

134. Weggel, J. R., The Impact Pressures of Breaking Water Waves, Ph.D. thesis, Dept. of Civil Engr., Uni. of Illinois, 1968.

135. Welch, J. E. et. al., The MAC Method — A Computing Technique for Solving Viscous, Incompressible, Transient Fluid — Flow Problems Involving Free Surfaces, Los Alamos Sci. Lab., Los Alamos, New Mexico, LA-3425, 1965.

136. Welch, J. E., Computer Simulation of Water Waves, Datamation 12, No. 11, 41, 1966.

137. Wenzel, H. G., Jr., Y. N. Yoon, and R. C. T. Wang , The Effect of Rainfall on Sheet Flow, presented at the 50th Annual Meeting of AGU, April 21-25, 1969.

138. White, P. H., Effect of Transducer Size, Shape, and Surface Sensitivity on the Measurement of Boundary-Layer Pressures, J. Accoust. Soc. Am., 41, 1358, 1967.

139. Wischmeier, W. H., and D. D. Smith, Rainfall Energy and Its Relationship to Soil Loss, Trans. AGU, 39, 285, 1958.

140. Woo, D. C., and E. F. Brater, Spatially Varied Flow From Controlled Rainfall, Proc. ASCE, 88, HY6, 31, 1962.

141. Worthington, A. M., On Pendent Drops, Proc. Roy. Soc. (London), 32, 362, 1881.

142. Worthington, A. M., On Impact With a Liquid Surface, Proc. Roy. Soc., 34, 217, 1882.

143. Worthington, A. M., The Splash of a Drop and Allied Phenomena, Smithsonian Inst. Rept., 49, 197, 1894.

144. Worthington, A. M., and R. S. Cole, Impact With a Liquid Surface, Studied by the Aid of Instantaneous Photograph, Phil. Trans. Roy. Soc. 189A, 137, 1897.

145. Worthington, A. M., A Study of Splashes, Longmans, Green & Co., 1908.

146. Worthington, A. M., A Study of Splashes, MacMillan Co., N. Y., 1963.

147. Yu, Y. S., and J. S. McNown, Runoff From Impervious Surfaces, J. IAHR, 2, No. 1, 1964.

APPENDIX A THE COMPRESSIBILITY EFFECT

After a drop strikes a water layer, a portion of the fluid around the drop impact point is compressed. The effective compression area, A_c, for a drop with a spherical or elliptical shape is approximated by (15)

$$A_c \cong \pi \left(\frac{V_o}{c} \frac{d}{2}\right)^2 \tag{I-1}$$

For a 3 mm drop striking a water layer at 20 fps, it requires only approximately 2.5 microseconds for the compression wave to travel across the drop at a speed of 2000 fps, which corresponds to the wave speed of water with 0.1% air content (48, 129). During this short period of time an area, A_c, with a radius 0.015 mm is compressed, and a pressure P_c, generated by the compression wave, is approximately given by (40)

$$P_c \cong \rho c V_o A_c / A \tag{1-2}$$

where A is the average drop cross sectional area. For the drop impact case mentioned, this yields a pressure of approximately 2 lb/ft^2, which upon averaging over the sensing element of the transducer used in this study results in a pressure signal of a negligible magnitude of 2.5×10^{-7} psi. Therefore, for drops studied the compressible effect generated upon drop-liquid contact can be neglected and the fluid density is taken as constant.

APPENDIX B DROP FORMATION DATA

Tube Name	d_i^+ (in.)	d_o^+ (in.)	Δt_d (sec)	$L_h^{\neq}$ (in.)	$L^{\neq}$ (in.)	Sample Size	Drop Weight (gm)	d (mm)
PE10	.011	.024	1.845	7.0	0.875	100	.01	2.67
PE10	.011	.024	1.87	7.0	0.875	100	.01	2.67
PE10	.011	.024	-	7.0	0.875	100	.0099	2.66
PE10	.011	.024	-	-	-	90	.0103	2.70
PE10	.011	.024	-	-	-	50	.01071	2.73
PE10	.011	.024	-	-	-	20	.01	2.67
PE10	.011	.024	-	-	-	100	.0093	2.61
PE20	.023	.038	0.324	2.5	0.875	300	.016	3.13
PE20	.023	.038	0.433	2.5	0.875	301	.01585	3.12
PE20	.023	.038	-	2.5	0.875	300	.01545	3.09
PE20	.023	.038	-	-	-	100	.01575	3.11
PE20	.023	.038	—	—	—	300	.0161	3.14
PE20	.023	.038	0.377	—	—	100	.0157	3.11
PE20	.023	.038	—	—	—	200	.0153	3.08
PE20	.023	.038	—	—	—	200	.01545	3.09
PE20	.023	.038	—	—	—	200	.01635	3.15
PE20	.023	.038	—	—	—	200	.0160	3.13
PE50	.023	.038	0.963	1.5	0.5	300	.01512	3.07
PE50	.023	.038	—	2.0	0.5	100	.0154	3.08
PE50	.023	.038	0.46	2.0	1.0	300	.01495	3.06
PE50	.023	.038	—	2.0	1.0	100	.0149	3.06
PE50	.023	.038	—	—	—	100	.0168	3.18
PE50	.023	.038	—	—	—	100	.0130	2.92
PE50	.023	.038	—	—	—	100	.0152	3.08
PE50	.023	.038	—	—	—	200	.01445	3.02
PE50	.023	.038	0.48	—	—	100	.01813	3.26
PE50	.023	.038	—	—	—	200	.01492	3.06
PE160	.045	.062	1.24	2.0	0.625	100	.0245	3.60
PE160	.045	.062	0.558	2.0	0.625	101	.0264	3.70
PE160	.045	.062	—	2.0	0.625	201	.0273	3.74
PE160	.045	.062	—	—	—	101	.0268	3.72
PE160	.045	.062	—	—	—	301	.0273	3.74
PE160	.045	.062	—	—	—	101	.0280	3.77
PE160	.045	.062	—	—	—	150	.0282	3.78
PE160	.045	.062	—	—	—	100	.0265	3.70
—	—	.042	—	—	—	400	.01874	3.30
—	.023	.050	—	—	—	200	.0225	3.50
—	.023	.050	—	—	—	200	.0224	3.50
—	.023	.050	—	—	—	200	.02285	3.52
PE320	.106	.138	—	—	—	100	.0536	4.68
PE320	.106	.138	—	—	—	80	.05075	4.60

[+] The inside and outside diameter of the tube (d_i and d_o) are those specified by the manufacturer.

[≠] L_h is the static water head, and L is the length of the capillary tube.

APPENDIX C EXPERIMENTAL PRESSURE DATA

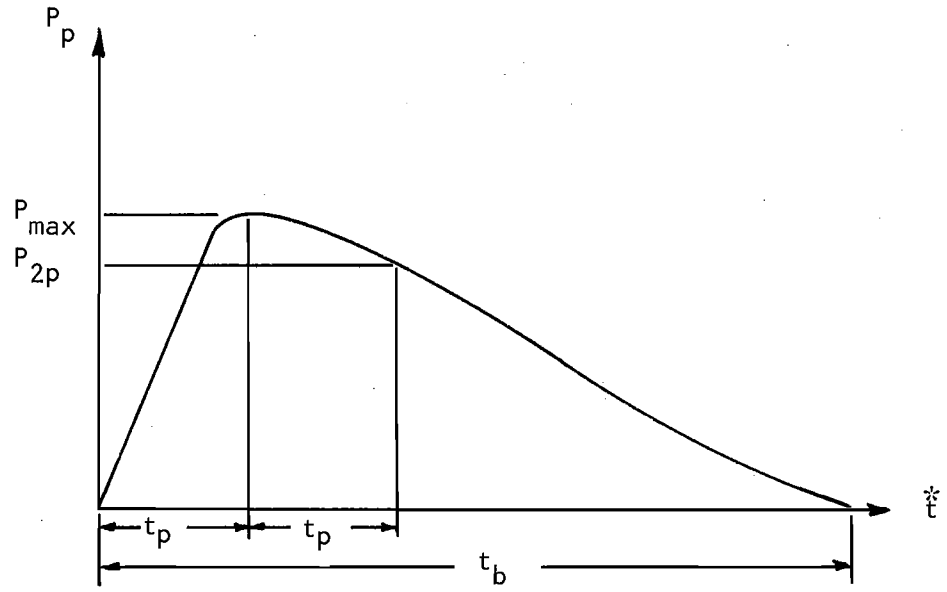

In this appendix, the maximum impact pressure, P_{max}, is presented as a function of the water layer depth, h. Also tabulated are the time to reach the maximum impact pressure, t_p, the approximate time base of a single pressure pulse, t_b, and the impact pressure value, P_{2p}, at $\overset{*}{t} = 2\ t_p$.

Tube Name	d (mm)	H (ft)	h (in.)	P_{max} (psi)	t_p (msec)	P_{2p} (psi)	t_b (msec)
PE10	2.7	33	0.123	0.660	0.16	-	1.2
PE10	2.7	33	0.233	0.326	0.2	0.28	-
PE10	2.7	33	0.393	0.132	0.2	0.11	-
PE10	2.7	33	0.184	0.453	0.22	-	-
PE10	2.7	33	0.306	0.212	0.14	0.2	-
PE10	2.7	33	0.576	0.0755	0.20	-	3.0
PE10	2.7	33	0.172	0.44	0.16	0.40	1.3
PE10	2.7	33	0.285	0.23	0.16	0.21	2.2
PE10	2.7	33	0.451	0.114	0.18	0.10	1.6
PE10	2.7	33	0.633	0.062	0.20	0.052	1.8
PE10	2.7	33	0.817	0.035	-	-	-
PE10	2.7	33	0.0	1.5	-	-	-
PE10	2.7	33	0.113	0.750	0.15	0.66	1.0
PE10	2.7	33	0.230	0.310	-	-	-
PE10	2.7	12	0.278	0.175	0.16	0.155	-
PE10	2.7	12	0.337	0.135	0.20	0.115	-
PE10	2.7	12	0.413	0.088	0.18	0.08	-
PE10	2.7	12	0.531	0.06	0.20	0.054	-
PE10	2.7	12	0.092	0.625	0.14	0.560	1.2
PE10	2.7	12	0.132	0.470	0.18	0.38	1.6
PE10	2.7	12	0.198	0.300	0.20	0.27	-
PE10	2.7	12	0.227	0.245	0.20	0.225	1.8
PE10	2.7	12	0.302	0.1555	0.22	0.13	1.8
PE10	2.7	12	0.135	0.477	0.19	0.39	1.4
PE10	2.7	12	0.138	0.408	0.20	-	-
PE10	2.7	12	0.449	0.080	0.26	-	-
PE10	2.7	12	0.540	0.056	0.26	-	-
PE10	2.7	12	0.194	0.311	0.22	-	-
PE10	2.7	12	0.102	0.583	0.20	-	-
PE10	2.7	12	0.0	1.261	-	-	-
PE10	2.7	7.5	0.227	0.18	0.28	0.15	1.8
PE10	2.7	7.5	0.288	0.125	0.28	0.10	-
PE10	2.7	7.5	0.374	0.088	0.36	0.064	-
PE10	2.7	7.5	0.477	0.056	-	-	-
PE10	2.7	7.5	0.052	0.6	0.2	0.43	0.9
PE10	2.7	7.5	0.096	0.4	0.2	0.34	-
PE10	2.7	7.5	0.165	0.285	0.28	0.22	2.0
PE10	2.7	7.5	0.270	0.150	-	-	-
PE10	2.7	7.5	0.365	0.092	-	-	-
PE10	2.7	7.5	0.280	0.136	0.22	0.126	-

Tube Name	d (mm)	H (ft)	h (in.)	P_{max} (psi)	t_p (msec)	P_{2p} (psi)	t_b (msec)
PE10	2.7	7.5	0.469	0.056	0.20	0.052	-
PE10	2.7	7.5	0.056	0.583	0.16	0.47	1.0
PE10	2.7	7.5	0.548	0.043	0.32	-	-
PE10	2.7	7.5	0.105	0.447	0.20	0.39	1.6
PE10	2.7	7.5	0.215	0.199	0.28	0.175	2.0
PE10	2.7	7.5	0.295	0.126	0.26	0.11	-
PE10	2.7	7.5	0.477	0.060	-	-	-
PE10	2.7	4.75	0.0	0.66	0.03	-	-
PE10	2.7	4.75	0.176	0.20	0.3	0.17	2.2
PE10	2.7	4.75	0.248	0.11	0.32	-	-
PE10	2.7	4.75	0.315	0.08	0.25	0.074	3.0
PE10	2.7	4.75	0.398	0.056	0.25	-	-
PE10	2.7	4.75	0.474	0.04	0.25	-	-
PE10	2.7	4.75	0.062	0.42	0.22	0.34	1.2
PE10	2.7	4.75	0.159	0.20	0.30	0.18	-
PE10	2.7	4.75	0.134	0.243	0.30	0.21	1.6
PE10	2.7	4.75	0.201	0.1554	0.32	0.126	-
PE10	2.7	4.75	0.402	0.0544	0.40	-	-
PE10	2.7	4.75	0.530	0.0311	0.40	-	-
PE20	3.12	33	0.093	1.204	0.08	1.1	0.8
PE20	3.12	33	0.145	0.741	0.14	-	1.4
PE20	3.12	33	0.255	0.398	0.16	0.37	-
PE20	3.12	33	0.455	0.157	0.10	-	-
PE20	3.12	33	0.547	0.107	-	-	-
PE20	3.12	33	0.111	0.98	0.14	0.81	1.0
PE20	3.12	33	0.209	0.49	0.16	0.44	1.8
PE20	3.12	33	0.328	0.27	0.14	-	-
PE20	3.12	33	0.048	1.85	0.09	1.60	-
PE20	3.12	33	0.113	1.08	-	-	-
PE20	3.12	33	0.210	0.48	-	-	-
PE20	3.12	33	0.140	0.80	0.15	-	-
PE20	3.12	33	0.403	0.20	0.20	0.175	-
PE20	3.12	33	0.0	2.7	-	-	-
PE20	3.12	33	0.110	1.0	0.17	-	1.2
PE20	3.12	33	0.162	0.67	0.20	0.54	1.6
PE20	3.12	33	0.233	0.48	0.18	0.40	-
PE20	3.12	33	0.335	0.24	0.20	0.22	-
PE20	3.12	33	0.449	0.15	0.20	-	-
PE20	3.12	33	0.528	0.106	0.20	0.104	-
PE20	3.12	33	0.613	0.096	-	-	-
PE20	3.12	12	0.135	0.56	0.1	0.52	1.4
PE20	3.12	12	0.237	0.31	0.2	0.29	1.8

Tube Name	d (mm)	H (ft)	h (in.)	P_{max} (psi)	t_p (msec)	P_{2p} (psi)	t_b (msec)
PE20	3.12	12	0.338	0.18	0.2	0.17	-
PE20	3.12	12	0.481	0.102	0.2	0.096	-
PE20	3.12	12	0.581	0.072	0.2	0.068	-
PE20	3.12	12	0.110	0.7	0.14	0.64	1.2
PE20	3.12	12	0.069	0.92	-	-	-
PE20	3.12	12	0.248	0.294	0.22	0.27	-
PE20	3.12	12	0.310	0.206	0.20	0.20	-
PE20	3.12	12	0.103	0.794	0.18	0.63	1.0
PE20	3.12	12	0.365	0.152	0.24	-	-
PE20	3.12	12	0.460	0.103	0.28	-	-
PE20	3.12	12	0.528	0.0862	0.24	-	-
PE20	3.12	12	0.173	0.47	0.24	-	-
PE20	3.12	7.5	0.112	0.52	0.2	-	1.4
PE20	3.12	7.5	0.192	0.29	0.3	0.26	-
PE20	3.12	7.5	0.252	0.22	0.3	0.19	-
PE20	3.12	7.5	0.314	0.15	0.26	0.13	2.0
PE20	3.12	7.5	0.415	0.097	0.25	0.088	-
PE20	3.12	7.5	0.576	0.056	0.30	0.048	3.0
PE20	3.12	7.5	0.08	0.72	0.20	0.58	1.0
PE20	3.12	7.5	0.158	0.365	0.28	0.29	1.8
PE20	3.12	7.5	0.40	0.108	0.32	-	-
PE20	3.12	7.5	0.484	0.069	0.40	-	-
PE20	3.12	7.5	0.128	0.451	0.28	0.36	1.4
PE20	3.12	7.5	0.246	0.235	0.24	-	-
PE20	3.12	7.5	0.071	0.745	0.20	0.63	1.0
PE20	3.12	4.7	0.078	0.48	0.24	0.40	1.4
PE20	3.12	4.7	0.106	0.37	0.28	0.31	1.7
PE20	3.12	4.7	0.164	0.265	0.35	0.22	2.3
PE20	3.12	4.7	0.278	0.135	0.30	0.115	2.7
PE20	3.12	4.7	0.432	0.064	0.45	0.05	-
PE20	3.12	4.7	0.509	0.048	0.40	-	-
PE20	3.12	4.7	0.0	0.80	0.10	-	-
PE20	3.12	4.7	0.063	0.53	0.20	-	-
PE20	3.12	4.7	0.137	0.30	0.30	-	-
PE20	3.12	4.7	0.233	0.17	0.4	-	-
PE20	3.12	4.7	0.333	0.09	0.4	-	-
PE20	3.12	4.7	0.534	0.039	0.4	-	-
PE20	3.12	4.7	0.061	0.569	0.20	0.43	1.2
PE20	3.12	4.7	0.197	0.225	0.31	0.20	-
PE20	3.12	4.7	0.274	0.142	0.30	-	-
PE20	3.12	4.7	0.395	0.078	0.34	-	-

Tube Name	d (mm)	H (ft)	h (in.)	P_{max} (psi)	t_p (msec)	P_{2p} (psi)	t_b (msec)
PE50	3.12	33	0.17	0.672	0.20	0.575	-
PE50	3.12	33	0.095	1.334	0.14	1.28	1.0
PE50	3.12	33	0.303	0.315	0.15	0.28	2.5
PE50	3.12	33	0.178	0.62	0.12	0.10	-
PE50	3.12	33	0.30	0.34	0.19	0.30	-
PE50	3.12	33	0.16	0.78	0.13	0.65	1.2
PE50	3.12	33	0.238	0.45	0.13	0.41	1.8
PE50	3.12	33	0.48	0.14	-	-	-
PE50	3.12	33	0.097	1.3	-	-	-
PE50	3.12	33	0.055	1.6	0.15	-	-
PE50	3.12	33	0.11	1.0	-	-	-
PE50	3.12	33	0.156	0.646	0.2	0.52	1.5
PE50	3.12	33	0.203	0.552	0.2	0.47	1.8
PE50	3.12	33	0.296	0.374	0.2	0.32	2.0
PE50	3.12	33	0.414	0.201	0.2	0.18	2.0
PE50	3.12	33	0.482	0.159	0.2	0.14	-
PE50	3.12	11.5	0.144	0.66 0.72	-	-	1.5
PE50	3.12	11.5	0.230	0.35	-	-	-
PE50	3.12	11.5	0.302	0.26	-	-	-
PE50	3.12	11.5	0.470	0.11 0.12	0.2	-	4.0
PE50	3.12	11.5	0.602	0.072 0.076	0.25	-	4.0
PE50	3.12	11.5	0.706	0.046 0.052	0.30	-	4.0
PE50	3.12	11.5	0.08	1.06 1.20	0.16	0.90	1.20
PE50	3.12	11.5	0.137	0.7	0.26	0.52	1.40
PE50	3.12	11.5	0.371	0.165	0.34	0.13	-
PE50	3.12	11.5	0.514	0.09	0.24	0.08	2.0
PE50	3.12	11.5	0.100	0.96	0.20	0.78	1.40
PE50	3.12	11.5	0.0	1.60	0.06	1.44	0.80
PE50	3.12	11.5	0.105	0.92	0.15	0.86	1.10
PE50	3.12	11.5	0.130	0.64 0.80	0.16	0.60	1.4
PE50	3.12	11.5	0.170	0.50 0.58	0.18	0.46	1.5
PE50	3.12	11.5	0.237	0.35 0.42	0.30	0.24	2.2
PE50	3.12	11.5	0.296	0.24 0.27	0.20	-	-

Tube Name	d (mm)	H (ft)	h (in.)	P_{max} (psi)	t_p (msec)	P_{2p} (psi)	t_b (msec)
PE50	3.12	11.5	0.432	0.15	-	-	-
PE50	3.12	11.5	0.0	1.80	-	-	-
PE50	3.12	11.5	0.060	1.20	0.14	1.1	1.0
PE50	3.12	11.5	0.105	1.00	0.16	-	1.32
PE50	3.12	11.5	0.208	0.48	0.30	-	2.0
PE50	3.12	11.5	0.307	0.265	0.25	-	2.5
PE50	3.12	11.5	0.408	0.160	0.20	-	3.2
PE50	3.12	11.5	0.500	0.110	0.40	-	3.0
PE50	3.12	11.5	0.0	4.4	0.025	4.0	-
PE50	3.12	11.5	0.169	0.52	0.26	0.4	1.72
PE50	3.12	11.5	0.29	0.27	0.20	-	2.50
PE50	3.12	11.5	0.46	0.11	0.30	0.09	3.0
PE50	3.12	11.5	0.62	0.064	0.35	0.054	-
PE50	3.12	11.5	0.072	0.96	0.16	-	-
PE50	3.12	11.5	0.099	0.91	-	-	-
PE50	3.12	7.8	0.111	0.60	0.2	0.56	1.5
PE50	3.12	7.8	0.191	0.34	0.4	0.26	-
PE50	3.12	7.8	0.308	0.18	0.35	-	2.8
PE50	3.12	7.8	0.373	0.135	0.30	0.11	-
PE50	3.12	7.8	0.445	0.10	-	-	-
PE50	3.12	7.8	0.033	1.0	0.18	0.83	0.9
PE50	3.12	7.25	0.0	1.2	0.04	-	0.7
PE50	3.12	7.25	0.135	0.45 0.52	0.3	0.3 0.4	1.6
PE50	3.12	7.25	0.215	0.27 0.31	0.26	0.27	-
PE50	3.12	7.25	0.380	0.115	0.35	0.105	3.5
PE50	3.12	7.25	0.141	0.47 0.49	0.28	0.37	1.8
PE50	3.12	7.25	0.240	0.22	0.30	0.18	2.5
PE50	3.12	4.3	0.0	0.88	0.10	0.72	0.8
PE50	3.12	4.3	0.148	0.27	0.50	0.22	2.15
PE50	3.12	4.3	0.255	0.143	-	-	-
PE50	3.12	4.3	0.26	0.143	0.35	0.126	3.0
PE50	3.12	4.3	0.36	0.066	0.8	0.044	-
PE50	3.12	4.3	0.08	0.43	0.4	0.286	1.6
PE50	3.12	4.3	0.47	0.044	0.5	0.04	4.0
PE160	3.7	33	0.180	0.815	0.20	0.66	-
PE160	3.7	33	0.322	0.408	0.20	-	-
PE160	3.7	33	0.445	0.232	0.20	-	-

Tube Name	d (mm)	H (ft)	h (in.)	P_{max} (psi)	t_p (msec)	P_{2p} (psi)	t_b (msec)
PE160	3.7	33	0.587	0.139	0.20	-	-
PE160	3.7	33	0.0	2.600	-	-	-
PE160	3.7	33	0.080	2.000	0.09	1.9	0.68
PE160	3.7	33	0.231	0.800	-	-	-
PE160	3.7	33	0.361	0.390	0.20	0.35	-
PE160	3.7	33	0.498	0.195	-	-	-
PE160	3.7	33	0.050	1.700	-	-	-
PE160	3.7	33	0.0	5.200	-	-	-
PE160	3.7	33	0.060	2.000	-	-	-
PE160	3.7	33	0.052	2.700	-	-	-
PE160	3.7	33	0.089	1.8	0.14	-	0.85
PE160	3.7	33	0.148	1.2	0.20	0.85	1.6
PE160	3.7	33	0.253	0.6	0.20	-	-
PE160	3.7	33	0.320	0.4	0.20	0.35	1.8
PE160	3.7	33	0.418	0.29	0.20	-	-
PE160	3.7	33	0.557	0.175	-	-	-
PE160	3.7	12	0.21	0.50	0.18	0.45	-
PE160	3.7	12	0.319	0.30	0.22	0.28	-
PE160	3.7	12	0.471	0.155	0.20	0.15	2.3
PE160	3.7	12	0.389	0.225	0.30	0.20	-
PE160	3.7	12	0.581	0.1	-	-	-
PE160	3.7	12	0.078	1.38	0.10	1.28	1.0
PE160	3.7	12	0.111	1.02	0.20	0.86	1.2
PE160	3.7	12	0.163	0.68	0.20	0.62	1.4
PE160	3.7	12	0.274	0.375	0.20	0.35	-
PE160	3.7	12	0.107	1.03	0.14	0.97	1.2
PE160	3.7	12	0.187	0.582	0.20	0.50	1.6
PE160	3.7	12	0.209	0.514	0.20	0.50	1.9
PE160	3.7	12	0.367	0.223	0.36	-	-
PE160	3.7	12	0.367	0.238	0.36	-	-
PE160	3.7	12	0.247	0.427	0.20	0.40	1.8
PE160	3.7	12	0.495	0.136	0.32	-	-
PE160	3.7	12	0.240	0.433	0.20	-	-
PE160	3.7	12	0.064	1.347	0.11	1.30	0.8
PE160	3.7	12	0.174	0.615	0.20	-	-
PE160	3.7	7.5	0.078	0.96	0.16	0.88	1.2
PE160	3.7	7.5	0.130	0.55	0.24	0.47	1.6
PE160	3.7	7.5	0.225	0.35	0.30	0.27	-
PE160	3.7	7.5	0.280	0.275	0.25	0.25	3.0
PE160	3.7	7.5	0.350	0.215	0.30	-	3.0

Tube Name	d (mm)	H (ft)	h (in.)	P_{max} (psi)	t_p (msec)	P_{2p} (psi)	t_b (msec)
PE160	3.7	7.5	0.419	0.15	0.40	0.12	-
PE160	3.7	7.5	0.503	0.10	0.25	0.094	-
PE160	3.7	7.5	0.073	0.92	-	-	-
PE160	3.7	7.5	0.101	0.74	0.20	0.68	1.4
PE160	3.7	7.5	0.155	0.54	0.20	0.50	1.6
PE160	3.7	7.5	0.205	0.43	-	-	-
PE160	3.7	7.5	0.075	0.962	0.20	0.86	1.2
PE160	3.7	7.5	0.174	0.433	0.34	0.36	2.0
PE160	3.7	7.5	0.275	0.26	0.40	0.23	-
PE160	3.7	7.5	0.360	0.178	0.34	-	-
PE160	3.7	7.5	0.503	0.0962	0.40	-	-
PE160	3.7	4.67	0.164	0.34	0.3	0.3	2.0
PE160	3.7	4.67	0.512	0.068	0.35	0.062	3.5
PE160	3.7	4.67	0.264	0.175	0.5	0.13	3.0
PE160	3.7	4.67	0.383	0.105	0.4	0.075	-
PE160	3.7	4.67	0.105	0.54	0.22	0.49	1.8
PE160	3.7	4.67	0.215	0.27	0.25	0.25	2.5
PE160	3.7	4.67	0.0	1.35	0.055	-	-
PE160	3.7	4.67	0.064	0.76	0.17	-	-
PE160	3.7	4.67	0.098	0.538	0.28	0.44	-
PE160	3.7	4.67	0.180	0.308	0.46	0.25	2.2
PE160	3.7	4.67	0.328	0.13	0.50	0.096	-
PE160	3.7	4.67	0.425	0.0924	0.5	-	-

APPENDIX D ANALYTICAL PRESSURE DATA

After Eq. 8 was solved for the pressure field at a specific time, the dynamic pressure in the bottom cells, that is cells along the bottom of the water layer, is calculated as

$$\varphi_i = \varphi_{i,1} - h/LF \tag{IV-1}$$

For i = 1, 3, 5, 7, 9, and 15, where i is the cell number, these dynamic point pressure values are tabulated at several time stages, along with the necessary information to convert them back into dimensional form by the following equations.

$$F = V_o^2/gL \tag{IV-2}$$

$$P_{i,1} = \rho V_o^2 \, (\varphi_i + h/LF) \tag{IV-3}$$

$$\overset{*}{t} = tL/V_o \tag{IV-4}$$

where $g = 32.2$ ft/sec^2 and $\rho = 1.935$ slug/ft^3.

d = 3.7 mm V_o = 15.9 fps h = 0.33 in. R = 0.89 in. L = 0.033 in.

t	φ_1	φ_3	φ_5	φ_7	φ_9	φ_{11}	φ_{13}	φ_{15}
0.	0.	0.	0.	0.	0.	0.	0.	0.
1.17	.0258	.0234	.0189	.0164	.0119	.0084	.0058	.0040
2.51	.0430	.0391	.0318	.0239	.0171	.0119	.0082	.0057
5.75	.0226	.0206	.0169	.0128	.0093	.0065	.0045	.0031
20.35	.0026	.0022	.0020	.0019	.0017	.0013	.0010	.0008

d = 2.7 mm V_o = 15.4 fps h = 0.241 in. R = 0.506 in. L = 0.0241 in.

t	φ_1	φ_3	φ_5	φ_7	φ_9	φ_{11}	φ_{13}	φ_{15}
0.	0.	0.	0.	0.	0.	0.	0.	0.
1.08	.0274	.0247	.0200	.0150	.0107	.0076	.0054	.0039
2.38	.0445	.0404	.0329	.0248	.0179	.0127	.0090	.0066
6.39	.0236	.0215	.0177	.0135	.0098	.0070	.0051	.0037
8.74	.0169	.0155	.0129	.0100	.0074	.0054	.0039	.0029

d = 2.7 mm V_o = 25.1 fps h = 0.405 in. R = 0.50 in. L = 0.0238 in.

t	φ_1	φ_3	φ_5	φ_7	φ_9	φ_{11}	φ_{13}	φ_{15}
0.	0.	0.	0.	0.	0.	0.	0.	0.
1.37	.0116	.0113	.0106	.0097	.0087	.0077	.0069	.0063
2.38	.0176	.0171	.0161	.0147	.0132	.0118	.0106	.0096
4.25	.0143	.0139	.0131	.0120	.0108	.0096	.0086	.0078
8.46	.0086	.0084	.0079	.0072	.0065	.0058	.0052	.0047

d = 2.7 mm V_o = 18.3 fps h = 0.241 in. R = 0.506 in. L = 0.0241 in.

t	φ_1	φ_3	φ_5	φ_7	φ_9	φ_{11}	φ_{13}	φ_{15}
0.	0.	0.	0.	0.	0.	0.	0.	0.
1.37	.0299	.0270	.0219	.0164	.0117	.0083	.0059	.0043
2.38	.0444	.0404	.0329	.0248	.0179	.0127	.0090	.0066
4.05	.0321	.0293	.0241	.0183	.0133	.0095	.0068	.0050
8.71	.0201	.0183	.0151	.0116	.0086	.0062	.0044	.0033

d = 2.7 mm V_o = 15.4 fps h = 0.12 in. R = 0.506 in. L = 0.0241 in.

t	φ_1	φ_3	φ_5	φ_7	φ_9	φ_{11}	φ_{13}	φ_{15}
0.	0.	0.	0.	0.	0.	0.	0.	0.
1.08	.107	.0765	.0394	.0182	.0083	.0038	.0018	.0008
2.38	.164	.121	.0659	.0313	.0144	.0066	.0031	.0014
4.30	.107	.082	.0477	.0239	.0113	.0053	.0025	.0012
8.86	.0296	.0216	.0172	.0111	.0059	.0029	.0014	.0006

d = 2.7 mm V_o = 15.4 fps h = 0.245 in. R = 0.368 in. L = 0.0175 in.

t	φ_1	φ_3	φ_5	φ_7	φ_9	φ_{11}	φ_{13}	φ_{15}
0.	0.	0.	0.	0.	0.	0.	0.	0.
0.52	.0174	.0166	.0149	.0128	.0108	.0089	.0074	.0063
1.47	.0411	.0393	.0356	.0309	.0260	.0217	.0181	.0154
3.02	.0368	.0353	.0323	.0282	.0240	.0201	.0169	.0145
7.56	.0178	.0170	.0155	.0136	.0116	.0097	.0082	.0070

d = 2.67 mm V_o = 25.1 fps h = 0.147 in. R = 0.342 in. L = 0.0122 in.

t	φ_1	φ_3	φ_5	φ_7	φ_9	φ_{11}	φ_{13}	φ_{15}
0.	0.	0.	0.	0.	0.	0.	0.	0.
0.49	.0739	.0692	.0599	.0486	.0377	.0285	.0213	.0158
1.47	.111	.105	.0924	.0767	.0607	.0466	.0351	.0262
11.85	.0421	.0393	.0348	.0302	.0261	.0222	.0054	.0051

d = 3.12 mm V_o = 26.8 fps h = 0.278 in. R = 0.584 in. L = 0.0278 in.

t	φ_1	φ_3	φ_5	φ_7	φ_9	φ_{11}	φ_{13}	φ_{15}
0.	0.	0.	0.	0.	0.	0.	0.	0.
1.10	.0287	.0260	.0210	.0157	.0113	.0080	.0057	.0042
2.26	.0447	.0406	.0331	.0249	.0180	.0128	.0091	.0067
2.88	.0440	.0400	.0327	.0247	.0178	.0127	.0090	.0066
7.73	.0196	.0178	.0147	.0114	.0084	.0061	.0044	.0032

d = 3.12 mm V_o = 26.8 fps h = 0.111 in. R = 0.584 in. L = 0.0278 in.

t	φ_1	φ_3	φ_5	φ_7	φ_9	φ_{11}	φ_{13}	φ_{15}
0.	0.	0.	0.	0.	0.	0.	0.	0.
1.08	.161	.102	.0414	.0153	.0057	.0021	.0008	.0003
2.37	.236	.160	.0710	.0272	.0102	.0038	.0015	.0006
4.56	.137	.0931	.0478	.0206	.0081	.0031	.0012	.0005
7.59	.0586	.0286	.0191	.0113	.0051	.0021	.0008	.0003

d = 3.12 mm V_o = 21.8 fps h = 0.473 in. R = 0.584 in. L = 0.0278 in.

t	φ_1	φ_3	φ_5	φ_7	φ_9	φ_{11}	φ_{13}	φ_{15}
0.	0.	0.	0.	0.	0.	0.	0.	0.
1.22	.0111	.0108	.0102	.0093	.0083	.0074	.0066	.0060
2.38	.0176	.0171	.0161	.0147	.0132	.0118	.0106	.0096
4.49	.0146	.0142	.0133	.0122	.0110	.0098	.0088	.0080
8.45	.0085	.0083	.0078	.0072	.0065	.0058	.0052	.0047

d = 3.12 mm V_o = 21.8 fps h = 0.278 in. R = 0.584 in. L = 0.0278 in.

t	φ_1	φ_3	φ_5	φ_7	φ_9	φ_{11}	φ_{13}	φ_{15}
0.	0.	0.	0.	0.	0.	0.	0.	0.
1.08	.0275	.0249	.0201	.0150	.0108	.0076	.0054	.0040
2.38	.0447	.0406	.0331	.0249	.0180	.0128	.0091	.0067
4.24	.0353	.0327	.0264	.0201	.0146	.0104	.0074	.0055
8.50	.0209	.0190	.0158	.0122	.0090	.0065	.0047	.0035

d = 3.12 mm V_o = 21.8 fps h = 0.111 in. R = 0.584 in. L = 0.0278 in.

t	φ_1	φ_3	φ_5	φ_7	φ_9	φ_{11}	φ_{13}	φ_{15}
0.	0.	0.	0.	0.	0.	0.	0.	0.
1.22	.167	.106	.0433	.0160	.0059	.0022	.0009	.0003
2.37	.236	.160	.0710	.0270	.0101	.0038	.0015	.0006
4.56	.137	.0928	.0477	.0205	.0080	.0031	.0012	.0005
8.16	.0337	.0163	.0172	.0110	.0051	.0021	.0008	.0003

d = 3.12 mm V_o = 18.8 fps h = 0.390 in. R = 0.50 in. L = 0.0278 in.

t	φ_1	φ_3	φ_5	φ_7	φ_9	φ_{11}	φ_{13}	φ_{15}
0.	0.	0.	0.	0.	0.	0.	0.	0.
1.27	.0161	.0154	.0140	.0123	.0106	.0091	.0080	.0072
2.38	.0253	.0242	.0221	.0194	.0168	.0145	.0127	.0115
4.59	.0208	.0199	.0182	.0160	.0139	.0120	.0106	.0096
7.45	.0143	.0137	.0125	.0110	.0096	.0083	.0073	.0067

d = 3.12 mm V_o = 18.8 fps h = 0.278 in. R = 0.584 in. L = 0.0278 in.

t	φ_1	φ_3	φ_5	φ_7	φ_9	φ_{11}	φ_{13}	φ_{15}
0.	0.	0.	0.	0.	0.	0.	0.	0.
1.22	.0286	.0259	.0210	.0157	.0113	.0080	.0057	.0041
2.38	.0444	.0404	.0329	.0248	.0179	.0127	.0090	.0066
4.33	.0333	.0304	.0249	.0189	.0137	.0098	.0070	.0051
8.67	.0202	.0184	.0152	.0117	.0086	.0062	.0045	.0033

d = 3.12 mm V_o = 15.8 fps h = 0.390 in. R = 0.50 in. L = 0.0278 in.

t	φ_1	φ_3	φ_5	φ_7	φ_9	φ_{11}	φ_{13}	φ_{15}
0.	0.	0.	0.	0.	0.	0.	0.	0.
1.15	.0161	.0154	.0140	.0123	.0106	.0091	.0080	.0072
2.31	.0253	.0243	.0221	.0194	.0168	.0145	.0127	.0115
4.29	.0194	.0186	.0170	.0150	.0130	.0112	.0099	.0090
7.66	.0130	.0125	.0114	.0101	.0087	.0076	.0067	.0061

d = 3.12 mm V_o = 18.8 fps h = 0.111 in. R = 0.50 in. L = 0.0278 in.

t	φ_1	φ_3	φ_5	φ_7	φ_9	φ_{11}	φ_{13}	φ_{15}
0.	0.	0.	0.	0.	0.	0.	0.	0.
1.20	.172	.110	.0452	.0168	.0062	.0023	.0009	.0004
2.41	.245	.166	.0738	.0283	.0106	.0040	.0015	.0006
4.29	.150	.111	.0555	.0236	.0092	.0035	.0014	.0006
6.74	.0549	.0322	.0203	.0117	.0051	.0021	.0008	.0003

d = 3.12 mm V_o = 15.8 fps h = 0.111 in. R = 0.473 in. L = 0.0278 in.

t	φ_1	φ_3	φ_5	φ_7	φ_9	φ_{11}	φ_{13}	φ_{15}
0.	0.	0.	0.	0.	0.	0.	0.	0.
1.06	.194	.123	.0501	.0185	.0069	.0026	.0010	.0004
2.08	.270	.181	.0802	.0306	.0114	.0043	.0017	.0007
4.30	.166	.107	.0546	.0234	.0091	.0035	.0014	.0006
9.06	.000	.0185	.0195	.0136	.0064	.0026	.0010	.0004

d = 3.7 mm V_o = 28.41 fps h = 0.395 in. R = 0.561 in. L = 0.033 in.

t	φ_1	φ_3	φ_5	φ_7	φ_9	φ_{11}	φ_{13}	φ_{15}
0.	0.	0.	0.	0.	0.	0.	0.	0.
0.93	.0198	.0186	.0162	.0135	.0110	.0090	.0076	.0068
2.37	.0331	.0311	.0273	.0228	.0186	.0153	.0130	.0116
4.30	.0251	.0237	.0208	.0175	.0144	.0118	.0101	.0090
8.19	.0148	.0140	.0124	.0105	.0087	.0073	.0062	.0056

d = 3.7 mm V_o = 22.6 fps h = 0.395 in. R = 0.506 in. L = 0.033 in.

t	φ_1	φ_3	φ_5	φ_7	φ_9	φ_{11}	φ_{13}	φ_{15}
0.	0.	0.	0.	0.	0.	0.	0.	0.
1.22	.0211	.0198	.0173	.0144	.0117	.0096	.0081	.0072
2.37	.0331	.0311	.0273	.0288	.0186	.0153	.0130	.0116
4.33	.0252	.0237	.0209	.0175	.0144	.0119	.0101	.0090
8.47	.0136	.0128	.0113	.0096	.0080	.0066	.0057	.0051

d = 3.68 mm V_o = 28.2 fps h = 0.151 in. R = 0.468 in. L = 0.0167 in.

t	φ_1	φ_3	φ_5	φ_7	φ_9	φ_{11}	φ_{13}	φ_{15}
0.	0.	0.	0.	0.	0.	0.	0.	0.
0.77	.123	.111	.0875	.0631	.0430	.0286	.0188	.0124
3.85	.166	.154	.128	.0976	.0695	.0476	.0319	.0212
7.67	.0887	.0827	.0706	.0560	.0426	.0313	.0222	.0153
14.25	.0712	.0530	.0286	.0173	.0131	.0118	.0118	.0125

d = 3.7 mm V_o = 28.41 fps h = 0.132 in. R = 0.561 in. L = 0.033 in.

t	φ_1	φ_3	φ_5	φ_7	φ_9	φ_{11}	φ_{13}	φ_{15}
0.	0.	0.	0.	0.	0.	0.	0.	0.
1.25	.163	.103	.0422	.0157	.0058	.0022	.0009	.0004
2.54	.235	.157	.0698	.0267	.0100	.0038	.0015	.0006
4.70	.148	.0959	.0491	.0213	.0084	.0032	.0013	.0005
9.16	.0386	.0131	.0162	.0112	.0054	.0022	.0009	.0004

d = 3.7 mm V_o = 28.41 fps h = 0.264 in. R = 0.561 in. L = 0.033 in.

t	φ_1	φ_3	φ_5	φ_7	φ_9	φ_{11}	φ_{13}	φ_{15}
0.	0.	0.	0.	0.	0.	0.	0.	0.
1.10	.0449	.0385	.0282	.0188	.0121	.0079	.0054	.0041
2.25	.0690	.0598	.0443	.0299	.0194	.0127	.0087	.0066
4.17	.0504	.0439	.0330	.0226	.0148	.0098	.0067	.0051
8.72	.0277	.0242	.0187	.0134	.0092	.0062	.0044	.0033

d = 3.7 mm V_o = 19.3 fps h = 0.395 in. R = 0561 in. L = 0.033 in.

t	φ_1	φ_3	φ_5	φ_7	φ_9	φ_{11}	φ_{13}	φ_{15}
0.	0.	0.	0.	0.	0.	0.	0.	0.
1.10	.0210	.0198	.0173	.0144	.0117	.0096	.0081	.0072
2.25	.0331	.0311	.0273	.0228	.0186	.0153	.0130	.0116
4.21	.0251	.0237	.0208	.0175	.0143	.0118	.0101	.0090
7.64	.0130	.0122	.0109	.0092	.0077	.0064	.0055	.0049

d = 3.7 mm V_o = 15.9 fps h = 0.395 in. R = 0.561 in. L = 0.033 in.

t	φ_1	φ_3	φ_5	φ_7	φ_9	φ_{11}	φ_{13}	φ_{15}
0.	0.	0.	0.	0.	0.	0.	0.	0.
1.10	.0210	.0197	.0172	.0143	.0117	.0096	.0081	.0072
2.25	.0330	.0311	.0272	.0227	.0186	.0153	.0129	.0115
4.21	.0249	.0235	.0207	.0173	.0142	.0117	.0100	.0089
7.60	.0166	.0155	.0136	.0114	.0094	.0078	.0066	.0060